The Dissertation Committee for Simon Kheifets
certifies that this is the approved version of the following dissertation:

High-sensitivity tracking of optically trapped particles in gases and liquids: observation of Brownian motion in velocity space

Committee:

Mark G. Raizen, Supervisor

Alejandro De Lozanne

Harry L. Swinney

Carlos Torres Verdín

Philip J. Morrison

High-sensitivity tracking of optically trapped particles in gases and liquids: observation of Brownian motion in velocity space

by

Simon Kheifets, A.B.

DISSERTATION

Presented to the Faculty of the Graduate School of

The University of Texas at Austin

in Partial Fulfillment

of the Requirements

for the Degree of

DOCTOR OF PHILOSOPHY

THE UNIVERSITY OF TEXAS AT AUSTIN

August 2014

For mum, dad, Olya and Pauly.

Acknowledgments

Working under the supervision of Professor Mark Raizen has been an honor and a privilege. For the past five years I have been continuously inspired by his creativity, perseverance and vision. I am thankful for the supportive environment which he has fostered in the Raizen group.

I began working in the Raizen group at the start of 2010, when I joined Tongcang Li, who had just finished developing the launching system for microspheres in air, and was in the process of optimizing the split-beam detection system. My first few years in the lab were spent working closely with Tongcang, first on measurements of Brownian motion in air, followed by work on active feedback cooling of a trapped particle in vacuum. I could not ask for a better mentor than Tongcang. His enthusiasm for experimental physics is contagious, and he has an incredibly intuitive way of understanding physics which makes him very good at explaining complicated concepts in very simple terms, something he is always eager to do.

For the majority of the water experiment I worked alongside Akarsh Simha, whose help was essential in bringing the experiment to fruition. Akarsh's background in theory helped us navigate the maze of hydrodynamic Brownian motion, his programming prowess proved invaluable for writing the control software, and he is an expert at the arduous task of constructing flow

cells. In the final stages of the experiment, we were joined by Kevin Mellin, a valuable addition during that critical stage. I would also like to thank Isaac Chavez and Giannis Keramidas for their preliminary work on the experiment, and Camilo Perez for his investigations of modified detection schemes. The next generation of the Brownian motion experiment is now in the hands of Jianyong Mo, with the help of Jimmy Kennington and Willium Plusnick and consultancy of Akarsh. Jianyong has been a great friend during my time in the group and my many discussions with him about the experiment have proven very useful for writing this dissertation. I wish Jianyong the best of luck.

In the last year I've been fortunate to have had the opportunity to work with Tom Mazur. I am constantly impressed by Tom's leadership, organization and work ethic.

As a new student in the Raizen group I was very glad for the help and company of the senior students who were always willing to drop what they were doing whenever I asked for assistance. David Medellin has always been the go-to guy for all math, electronics and computer related questions. Kirsten Viering always knew where everything was, and if she didn't she would always help to look. Adam Libson was a vault of information about absolutely everything. I also appreciate the help and company of the other group members who I've worked with during my time in the lab: Gabriel Price, Travis Bannerman, Melissa Jerkins, Charlotte Sanders, Jamie Gardner, Erik Anciaux, Alina Blinova, Georgios Stratis, Karl Burkhardt, Igal Bucay, Rob Clark, Rodrigo Castillo-Garza, Bruce Klappauf, Francisco Camargo, Daniel Ellsworth, Daniel

High-sensitivity tracking of optically trapped particles in gases and liquids: observation of Brownian motion in velocity space

Publication No. _____

Simon Kheifets, Ph.D.
The University of Texas at Austin, 2014

Supervisor: Mark G. Raizen

The thermal velocity fluctuations of microscopic particles mediate the transition from microscopic statistical mechanics to macroscopic long-time diffusion. Prior to this work, detection methods lacked the sensitivity necessary to resolve motion at the length and time scales at which thermal velocity fluctuations occur. This dissertation details two experiments which resulted in velocity measurement of the thermal motion of dielectric microspheres suspended by an optical trap in gases and liquids.

First, optical tweezers were used to trap glass microspheres in air over a wide range of pressures and a detection system was developed to track the trapped microspheres' trajectories with MHz bandwidth and <100 fm/$\sqrt{\text{Hz}}$ position sensitivity. Low-noise trajectory measurements allowed for observation of fluctuations in the instantaneous velocity of a trapped particle with a

signal to noise ratio (SNR) of 26 dB, and provided direct verification of the equipartition theorem and of the Maxwell-Boltzmann velocity distribution for a single Brownian particle.

Next, the detection technology was further optimized and used to track optically trapped silica and barium titanate glass microspheres in water and acetone with >50 MHz bandwidth and <3 fm/$\sqrt{\text{Hz}}$ sensitivity. Brownian motion in a liquid is influenced by hydrodynamic, time-retarded coupling between the particle and the fluid flow its motion generates. Our measurements allowed for instantaneous velocity measurement with an SNR of up to 16 dB and confirmed the Maxwell Boltzmann distribution for Brownian motion in a liquid. The measurements also revealed several unusual features predicted for Brownian motion in the regime of hydrodynamic coupling, including faster-than-exponential decay of the velocity autocorrelation function, correlation of the thermal force and non-zero cross-correlation between the particle's velocity and the thermal force preceding it.

Table of Contents

List of Figures

xv

Chapter 1

Introduction

In 1827, Robert Brown reported his observation[1] of what is now known to be the thermal motion of microscopic particles which now bears his name [2]. The nineteenth century saw several attempts to explain the phenomenon: Brownian motion seemed to be a macroscopic embodiment of the otherwise invisible erratic motion of molecules posited by kinetic theory. However, experimental measurements of the velocity, and thus kinetic energy, of the thermal motion of microscopic particles fell orders of magnitude short of the theory's prediction. [2, 3].

In 1905, Albert Einstein published paper in which he used statistical mechanics to predict the statistics of a particle's displacement rather than of its velocity [4]. In contemporary terms, Einstein's description was that of a Wiener process: for any time interval, no matter how short, consecutive displacements are statistically independent [5]. However, one of the properties of a Wiener process is that it has no well-defined derivative: Einstein's prediction gives no account of the statistics of the particle's velocity.

---

[1] Brown studied the motion systematically and concluded it was not caused by a living thing, but he was not the first to report on thermal motion, which was observed as early as 1785 by Jan Ingenhauz in 1785 [1]

In 1907, Einstein published a note in which he addressed the lack of an account of the particle's velocity in his description of Brownian motion. He noted that the time scales at which thermal energy is exchanged between the particle and the fluid, which are determined by fluid mechanics, were experimentally out of reach. Moreover, the displacements made by the particle during that time scale were many orders of magnitude smaller than even the particle size. He concluded that measurement of the velocity would be 'impossible' [6].

In 1908, Paul Langevin published a paper in which he tackled Brownian motion with a different approach: that of a stochastic differential equation [7]. In Langevin's description, the Brownian particle's velocity is an Ornstein-Uhlenbeck process, and its position is the time integral of its velocity, reducing to Einstein's prediction in the long time limit [5].

By 1909, Einstein's prediction was verified in experiments by Jean Perrin using the newly invented ultramicroscope; a significant result in that it removed final doubt in the scientific community of the molecular nature of matter [8,9]. However, experimental confirmation of Langevin's prediction of Brownian motion in velocity space would require a measurement deemed impossible by Einstein and even after a century's worth of technological advances Einstein's claim still held true. This dissertation details the results of two experiments involving successful measurement of Brownian motion in velocity space: the first using glass microspheres in gas [10], the second in liquid [11].

Both experiments relied on the use of tightly focused laser beams to

both contain and probe the microspheres' thermal motion. A dielectric sphere near the focus of a laser beam scatters some of the incident photons in a direction which depends on the bead's position. Changes in the bead's position are encoded in the spatial distribution of the scattered beam, which can be measured with high sensitivity. For sufficiently low measurement noise and bandwidth, the position signal can be differentiated to determine the particle's velocity. Also, the recoil force imparted on the sphere by the scattered photons happens to always point towards the center of the laser focus. This restoring force is negligible at the time scales of thermal velocity fluctuations, but at long times it prevents diffusion of the sphere out of the detection region, enabling continuous measurement over long time intervals. The principles of optical trapping and detection are discussed in Chapter 2.

1.1 Effect of fluid on Brownian dynamics

The dynamics of thermal velocity fluctuations of a glass microsphere strongly depend on the fluid's density and viscosity, and thus there are several distinct differences between the dynamics of glass microspheres in gases and in liquids. The viscosity of gases is typically much smaller than that of liquids, and the density of gasses is much smaller than that of dielectric solids, whereas liquids have densities comparable to those of dielectrics. In a gas with viscosity η, a dense sphere released with initial velocity v_0 experiences viscous damping, and its velocity decays exponentially with time constant $\tau_p \propto 1/\eta$, known as the momentum relaxation time. The dynamics of thermal velocity fluctuations

3

of a glass microsphere strongly depend on the fluid's density and viscosity, and thus there are several distinct differences between the dynamics of glass microspheres in gases and in liquids. The viscosity of gases is typically much smaller than that of liquids, and the density of gasses is much smaller than that of dielectric solids, whereas liquids have densities comparable to those of dielectrics. In a gas with viscosity η, a dense sphere released with initial velocity v_0 experiences viscous damping, and its velocity decays exponentially with time constant $\tau_p \propto 1/\eta$, known as the momentum relaxation time.

The same particle in a liquid will have much shorter τ_p, however, when released, the sphere's velocity does not decay as a simple exponential. In fact, the damping force exerted on the sphere by the fluid depends on the history of the sphere's motion before its release. This is because a fluctuation in the sphere's velocity at one instant results in a perturbation of the fluid flow around the sphere which gradually weakens as it decays outward to infinity. As long as the perturbation is near the sphere, it affects the force exerted on the sphere by the fluid; the fluid has 'memory' of the sphere's prior motion. The characteristic decay time of such interactions is $\tau_f = \tau_p \rho_f / \rho_p$, where ρ_f and ρ_p are the densities of the fluid and sphere, respectively. In gases, $\tau_f \ll \tau_p$; the velocity change during the exponential decay is too slow to result in significant perturbations to the flow, and the effect can be ignored. In liquids, the two time scales can be comparable. The decay can be faster or slower than an exponential, depending on the history of the sphere's velocity prior to being released.

An initially stationary sphere when released in a fluid at finite temperature does not remain stationary as a consequence of the force on the sphere from collisions with the thermal molecules of the fluid. Although the long-time average of the force from the collisions is zero, at short times the net force fluctuates resulting in Brownian motion. The steady state behavior represents a balance between acceleration due to thermal forces and deceleration from viscous forces. The distribution of the particle's velocity over time is predicted by the Maxwell-Boltzmann velocity distribution. The rate at which it explores this distribution is closely related to the damping dynamics described in the previous paragraphs (the relationship is precisely described by the fluctuation dissipation theorem [12]). Thus in air, velocity fluctuations occur over the time scale τ_p, while in water, the fluctuations have more variability, sometimes shorter, sometimes longer than τ_p.

Measurement of velocity by differentiation of consecutive position measurements is very demanding on the noise and bandwidth requirements for position detection. The time interval between successive position measurements must be small enough that the velocity remains relatively constant over its duration, while the uncertainty in each position measurement must be much smaller than the displacement over the interval. For a 3 μm diameter glass bead in water, it takes, on average, 10 ns for the velocity to change by 10 %. The root mean square velocity is about 0.3 mm per second. To measure the velocity with 10 % uncertainty, the position resolution must be at least 0.2 pm in 10 ns, corresponding to 6×10^{-17} m/$\sqrt{\text{Hz}}$ position sensitivity. The mea-

surement requirements in air are less demanding due to the weaker coupling between fluctuations in the bead and fluctuations in the gas. For the same 3 μm bead in air, the average time for the velocity to fluctuate by 10 % is ~ 50 μs. Velocity measurement with 10 % uncertainty requires 15 nm resolution in 50 μs, requiring a more reasonable position sensitivity of 10^{-10} m/$\sqrt{\text{Hz}}$. This was one of the main motivations for first attempting a measurement of the velocity of the Brownian motion of a trapped particle in air, described in the first part of this dissertation. The second part of this dissertation describes measurement in liquid, made possible by a detailed understanding of the complex dynamics in liquid and optimization of all aspects of the measurement process first developed for the air experiment.

1.2   Measurement in air

The theory of Brownian motion in air (in which hydrodynamic effects are neglected), is often referred to as Einstein-Ornstein-Uhlenbeck theory (EOU theory), though it is based more on Langevin's initial work than that of Einstein. By the 1930s, Ornstein and Uhlenbeck formalized Langevin's approach and extended the results to Brownian motion in a harmonic potential [13]. An overview of their results is given in Chapter 3.

The two greatest experimental challenges in measurement in air were that of launching the beads into and sensitive detection. Loading the trap in air is much more difficult than in water because van der Waals forces make microspheres stick to all surfaces and each other. An ultrasonic, inertial launching

6

method was developed to separate the microspheres and load them into an optical trap located within a vacuum chamber. A split-beam detection technique was developed, and gave improved performance over existing particle tracking methods. The description of the trapping and detection apparatus is given in Chapter 4.

The analysis of recorded trajectories is presented in Chapter 3. This includes comparison to the predictions of Einstein and EOU theory, followed by the results of instantaneous velocity measurement, including the confirmation of the Maxwell-Boltzmann velocity distribution for a single Brownian particle.

1.3 Measurement in liquid

Although the effect of hydrodynamic interaction on the force on a moving sphere was already known by Stokes in the nineteenth century, its influence on Brownian motion in liquids was not considered until much later. In the mid 1960s, developments in computers allowed, for the first time, to simulate statistical mechanics on the single-particle level. An anomaly was observed in the results of such hard-sphere molecular simulations, in the long-time behavior of the autocorrelation of individual molecules' velocity. The velocity autocorrelation at long times was much significantly larger than the prediction of EOU theory. The tails of the autocorrelation fit to a power law, and not the EOU prediction of an exponential [14–16]. These observations sparked interest in Brownian motion in the regime of hydrodynamic coupling that persists to this day [17, 18].

The earliest theoretical description of hydrodynamic Brownian motion was given in a Soviet journal in 1945, but was not known to western scientists until much later [17, 19]. Most of the theoretical progress in the field was made in the 1970s [20–24]. Though the expressions for the dynamics are much more complicated than those of EOU theory, the system can be solved analytically. A summary of those results, and comparison to EOU theory is given in Chapter 6. The most relevant difference, in the context of velocity measurement, is that velocity fluctuations occur at much shorter times than τ_p, which is already much shorter in liquid than in air.

Initial estimates (using EOU theory), suggested that with the detection method used in the air experiment could be easily improved to a level that would facilitate the measurement of instantaneous velocity in water. Not long after initial attempts, however, it was realized that hydrodynamic coupling leads to a much more gradual transition between the ballistic (constant-velocity) and diffusive regimes. At times shorter than τ_f, hydrodynamic theory of Brownian motion predicts that velocity autocorrelation function decays much *faster* than than the exponential prediction of EOU theory, meaning measurement in water was further out of reach than initial estimates suggested.

In order to resolve the velocity above the detection noise, it was necessary to optimize every parameter available. Silica microspheres were replaced by barium titanate glass microspheres, whose high refractive index increases the scattering of the detection beam, and whose high density slowed the Brow-

nian dynamics, allowing for longer averaging times. Water was replaced with acetone. Its low density and low viscosity further slows the rate of velocity fluctuation. To reduce the quantum-limited noise floor, a custom, high power, high bandwidth detector was developed. The experimental apparatus is described in Chapter 7.

The results are presented in Chapter 8. The instantaneous velocity was measured with an SNR of 14 dB and was observed to be in agreement with the Maxwell-Boltzmann distribution. Other results include the observation of faster-than-exponential decay in the velocity autocorrelation function, color in the thermal force and nonzero force-velocity cross correlation for positive and negative time.

Chapter 2

Position and velocity measurement of optically trapped particles

The existence of radiation pressure was first deduced from electromagnetic theory by James Clerk Maxwell in 1873 [25, 26]. It was first measured experimentally at the turn of the 20th century [27, 28]. Radiation pressure is very weak; 1 W of light reflecting from a mirror exerts about 7 nN of force. The advent of lasers introduced the possibility of focusing high power radiation to μm length scales; a 1W laser interacting with a microscopic particle can apply a force 10^5 times that of the gravitational force on the particle.

In 1970, Arthur Ashkin published a seminal paper reporting the use of focused laser beams to accelerate and trap μm size transparent particles [29]. Several years later he demonstrated optical levitation of oil droplets and glass microspheres in air [30], shortly followed by a demonstration of trapping in vacuum [31]. This powerful new tool was not limited to microparticles; it revolutionized the field of atomic physics by creating the ability to cool and trap atoms [32–35], paving the way towards atomic clocks and quantum degeneracy in the lab. In 1986, Ashkin et al. [36] observed stable trapping of dielectric particles using the gradient force from a single strongly focused laser

beam, an improvement over the prior work which required a restoring force to counteract the radiation pressure. This technique was then developed to trap and manipulate viruses and bacteria [37, 38] becoming a standard tool of biophysicists now known as optical tweezers [39]. The first section of this chapter gives an overview of the principles of optical trapping and calculations for some limiting cases which shed some light on the behavior of traps as a function of properties of the trapping laser, trapped particle and trapping medium.

The second section of this chapter discusses techniques to track the position of the particle within the trap. The most powerful of these is that of split beam detection, in which a focused laser (often the same beam used for trapping) is used to measure the position of the particle. The same mechanism that transfers momentum from the trapping beam to the particle also results in a change in the beam profile of the beam downstream of the particle. Measurement of changes in the beam profile can give a very sensitive readout of the particle's position.

In this work, position measurements are used to determine the velocity of the particle. The third section of this chapter gives an overview of sources of limitation to velocity measurements.

2.1 Optical trapping

The position-dependence of the force that a tightly-focused laser beam exerts on a microsphere located near the beam's focus results from momentum

transfer from photons scattering off the particle. An exact solution requires solving for the scattered light field and calculating the associated momentum transfer. In most real-world cases, the bead diameter d is comparable to trapping field wavelength λ and an analytical solution is impossible due to the combined effects of internal reflection and interference. However, many of the essential principles of optical trapping are revealed by considering the limiting cases: $d \gg \lambda$, in which beam propagation can be approximated using ray optics [40], and $d \ll \lambda$, in which the trapped particle is approximated as a Rayleigh scatterer [41].

2.1.1 Rayleigh approximation

When the trapped particle diameter is much smaller than the wavelength of the trapping beam, at any instant in time, the electric field is uniform over the entire particle. In this case, it is possible to treat the particle as a point-dipole (a Rayleigh scatterer) when calculating the interaction between the particle and the trapping field [36]. This section will summarize the results which are derived in Ref. [41]. As a rule of thumb, the Rayleigh approximation is valid for $d < \lambda/5$.

The radiation pressure exerted by the laser on the particle can be split into two parts: the scattering force and the gradient force. As the electric field oscillates in time, it induces a dipole moment, whose oscillations follow that of the electric field. The oscillating dipole radiates a secondary, or scattered field, in all directions. The momentum flux of the resulting field is nonzero;

some of it is transferred to the dipole in the form of the scattering force. The second component of radiation pressure is due to the Lorenz force exerted by the optical field on the induced dipole, which is proportional to the gradient of the laser field.

In the Rayleigh approximation, for a scatterer in a fluid with permittivity ϵ_m, the dipole moment $\mathbf{p}$ induced by an electric field $\mathbf{E}$ is given by $\mathbf{p} = 4\pi\epsilon_f\alpha\mathbf{E}$, where α is the particle's polarizability. For a sphere in a uniform electric field $\mathbf{E}$, the polarizability is given by:

$$\alpha = a^3\frac{m^2 - 1}{m^2 + 2}, \tag{2.1}$$

where a is the radius of the particle, $m = n_p/n_f$ is the ratio of the particle's refractive index (n_p) and that of the fluid (n_f). For a particle at the focus of a Gaussian laser beam, the scattering force points in the direction of laser propagation and its magnitude is:

$$F_{scat} = \frac{8\pi}{3}\frac{n_f}{c}k^4\alpha^2 I(\mathbf{r}) \tag{2.2}$$

where $I(\mathbf{r})$ is the intensity of the laser beam at the position $\mathbf{r}$ of the particle, $k = 2\pi/\lambda$, and λ is the wavelength of the trapping field in the fluid.

The gradient force is given by

$$F_{grad} = 2\pi\frac{n_f}{c}\alpha\boldsymbol{\nabla}I(\mathbf{r}). \tag{2.3}$$

For Gaussian beam with total power P, $1/e^2$ diameter of w_0 at its focus, the intensity profile is:

$$\frac{2P}{\pi w_0^2}\frac{1}{1 + (2\tilde{z})^2}\exp\left[-\frac{2(\tilde{x}^2 + \tilde{y}^2)}{1 + (2\tilde{z})^2}\right], \tag{2.4}$$

where $\tilde{x}, \tilde{y}$ and $\tilde{z}$ are the normalized spatial coordinates: $(\tilde{x}, \tilde{y}, \tilde{z})$ $= (x/w_0, y/w_0, z/kw_0^2)$.

On its own, the gradient force produces a stable trapping potential. For displacements much smaller than w_0, the potential is, to first order, harmonic. The transverse force constant is

$$K_x = \frac{8\pi n_f \alpha I(0)}{cw_0^2}, \tag{2.5}$$

where $I(0) = P/\pi w_0^2$ is the laser intensity at the focus. The axial force constant is

$$K_z = \frac{16\pi n_f \alpha I(0)}{k^2 cw_0^4}. \tag{2.6}$$

The scattering force causes in a shift of the minimum of the trapping potential in the direction of laser propagation. If the scattering force is too strong, there is no trap minimum and the particle cannot be trapped by the laser. The scattering force goes as α^2 and thus d^6, while the gradient force is linear in α and thus proportional to d^3, thus it is easier to form a stable minimum for a smaller particle than a larger one. However, the depth of the trap decreases as the size of the particle decreases, while the average thermal energy is independent of particle size, thus if the particle is too small, the trap lifetime will be very short. Also, α increases with increasing m, thus for large refractive index mismatch, the scattering force dominates the gradient force and trapping becomes more difficult.

The strength of the gradient force can be increased relative to the scattering force by decreasing the waist of the focus, w_0. Minimizing w_0 requires

14

focusing of the laser at a very steep angle, which can be quantified by a parameter known as the numerical aperture, $NA \equiv n_m \sin \theta$, where θ is the $1/e^2$ half-angle of convergence of the trapping beam. In terms of the NA, the beam waist is $w_0 = \lambda/\pi NA$. The upper limit for NA is n_f, and experimental realization of high-NA focusing requires a lens system corrected for spherical aberration. State-of-the-art optical tweezer experiments can operate close to this limit, achieving NA of around 1.2 in water [36, 42] and 0.95 in air [43].

2.1.2 Ray Optics Approximation

Perhaps a more intuitive understanding of the principle of optical trapping can be gained in the opposite limit. In the ray optics regime, the scattering force corresponds to back-reflections of the laser from the surfaces of the sphere. The gradient force corresponds to the recoil force from photons refracted by the sphere.

When a 'ray' of photons is bent by refraction through a glass sphere, momentum is transferred from the photons to the sphere. The average force on the sphere is $F = (Pn_f/c)\sin\theta$, where P is the power of the ray, c is the speed of light in vacuum, and θ is the angle of deflection. The force from a converging laser beam can be calculated by splitting the beam as a collection of rays and summing the force from each one.

Figure 2.1 illustrates the counter-intuitive mechanism of optical trapping: that a displacement of the sphere in any direction from the focus of the laser results in a restoring force. The figure shows the refraction of two

rays within the laser beam, which represent the $1/e^2$ contours of the Gaussian trapping beam. Ignoring surface reflections, when the bead is the center of the focus, all incoming and outgoing rays are perpendicular to the bead surface and no force is exerted on the bead. When the bead is displaced in a direction perpendicular to the optical axis, the outgoing rays are refracted in the same direction as the bead's displacement. The recoil force points towards the center of the trap. When the bead is displaced axially, upstream (opposite to the direction of laser propagation), it causes the outgoing rays to fan out into a wider cone than in the equilibrium position, the net forward momentum of the outgoing beam is reduced; some of the momentum is transferred into a force on the bead in the direction of beam propagation. When the bead is displaced downstream of the focus, the rays converge, the outgoing beam's forward momentum is increased, and the recoil forces the bead backwards.

The strength of the restoring force depends on the laser power, P, as well as the relative index of refraction between the bead and the medium m. For fixed laser power, the magnitude of the axial force (illustrated in the right two panels of figure 2.1) increases with large NA. The transverse force, however, is maximized when $NA \to 0$.

Not shown in Fig. 2.1 are rays reflected from the external and internal surfaces of the bead. These reflected rays also exert a recoil force on the bead. The net effect of reflected rays is to push the bead in the laser propagation direction, which is the ray-tracing analog of the scattering force. If the scattering force is stronger than the peak axial force, the potential of the optical
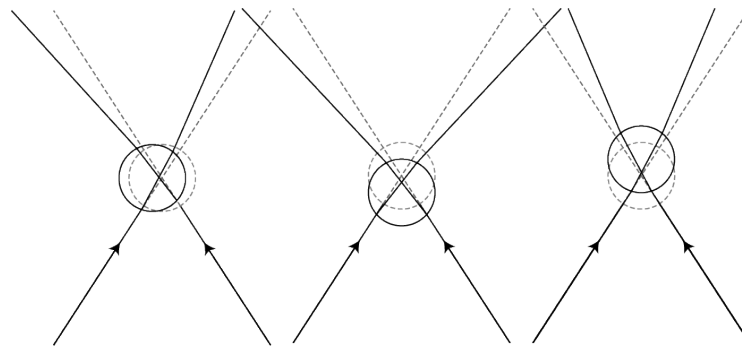
Figure 2.1: Illustration of optical trapping using ray tracing. The trapping laser is represented by two rays converging on the center of the trap. If scattering is ignored, the equilibrium position of the bead is at the laser focus. Each panel shows the effect of displacement of the microsphere on the direction and divergence angle of the outgoing laser (solid rays) compared to the outgoing beam when the microsphere is in the equilibrium position (dotted rays). Left: lateral displacement of the particle refracts the beam towards the same direction as displacement. Center: displacement upstream causes the outgoing beam to diverge faster, forward momentum is exchanged from the beam to the bead. Right: displacement downstream causes tighter focusing of the laser, recoil pushes the bead back upstream.

trap has no minimum. Stable trapping requires a potential well that is deep compared to the thermal energy. The axial force must be strong enough to counteract the radiation pressure from the reflected rays. For normal incidence, the reflectance is proportional to $(m^2 - 1)/(m^2 + 2)$, while the axial force has a linear dependence on m, thus particles with too large an index mismatch are more difficult to trap [42].

2.2   Position detection of trapped particles

Early optical trapping experiments relied on 2-D imaging to track particle position. In most cases, the same lens used to create a tight laser focus can be used to create a diffraction-limited image of the trapping plane, which can be recorded with a CCD camera. Circle-fitting algorithms can be used to measure the center of the imaged particle with much higher precision than the resolution of the microscope. The bandwidth of detection using this method is limited by the frame-rate of the camera used to record the image.

One early example of fast single-particle tracking is given in Ref. [44], in which an image of the particle's trajectory is recorded onto the film of a rotating drum camera with a time resolution of 0.1 μs. A later version of a similar experiment projected the image of a particle onto a neutral density wedge filter and the position was mapped to a voltage on a photodiode that collected the transmitted light [45].

In the 1990s, several techniques were developed in which a probe laser beam, or the trapping beam itself, was used in conjunction with fast photodi-
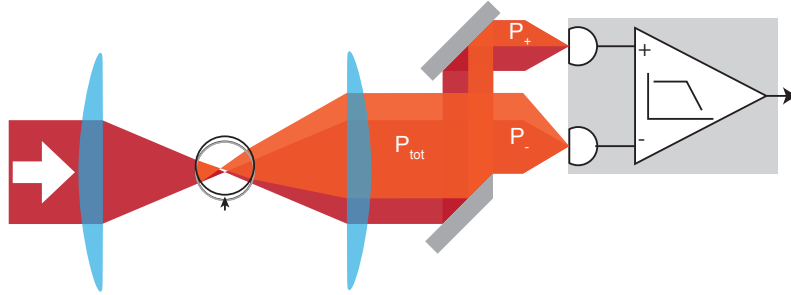
Figure 2.2: Illustration of split-beam detection. The trapping beam is re-collimated by a detection lens, and a cut mirror is used to split the beam onto two photodiodes. The output of the detector is proportional to the difference in the photocurrents of the two photodiodes. When the microsphere is displaced from the center of the trap, the beam is deflected, changing the powers of the two split beams. For small displacements, the detector output is proportional to the displacement of the microsphere

odes to track motion of microscopic particles with high bandwidth. A variety of techniques were used to produce a position-dependent intensity variation, including Wollaston interferometry [46,47], clipping of the scattered beam [48], and the use of a position-sensitive detector to detect deflection of the transmitted beam [49]. The technique that became the standard tool for position detection was the use of a quadrant photodiode to detect the deflection of the trapping beam [50–53]; a technique known as split beam detection (sometimes also referred to as back-focal plane detection).

2.2.1 Split beam detection

When the particle is displaced relative to the trapped beam, the same mechanism that results in a transverse force on the particle also changes the

19

angular intensity distribution of the outgoing, scattered (or refracted, in the ray optics picture) trapping beam. If a second lens is positioned with is focal point at the trap focus, it will re-collimate the outgoing beam (now referred to as the detection beam), and the angular intensity distribution is mapped the transverse intensity distribution of the laser.

In a quadrant photodiode, the photosensitive area of the semiconductor is split into four quadrants, each of which is an individual photodiode and photocurrent of each diode can be amplified separately. Changes in position of an incident laser beam can be measured by looking at linear combinations of the four signals. Horizontal deflection is proportional as the difference in signal between the left and right halves, while the vertical is proportional to the difference in photocurrent between top and bottom halves. When the two halves are perfectly aligned, laser intensity fluctuations are heavily suppressed because they contribute equally to both halves. The effect of laser intensity fluctuations can be minimized by normalizing each signal by the sum of all four quadrants.

In biophysics experiments the trapping beam is often used to manipulate the trapped sample; an appropriately placed mirror can be used to adjust the transverse location of the trapping beam without affecting its direction. When the quadrant detector is placed in a plane conjugate to the back focal plane of the detection lens, beam displacement at the detector is sensitive only to changes in the angular distribution of light exiting the trap and is (to first order) independent of the position of the trap in the trapping plane.

The bandwidth of quadrant photo-detection is less than that which can be achieved for single photodiodes. The bandwidth of an amplified photodiode is limited, among other things, by the photodiode capacitance. The large area and close spacing of the four photodiodes within a quadrant detector creates a relatively large capacitance that limits their bandwidth to ∼10-100 KHz.

A faster detection method developed by the Raizen group separates the spatial splitting and detection of the light. consists of a fiber-optic bundle that spatially splits the incident beam. Light exiting each half of the bundle was then focused onto two inputs of a fast, balanced photodetector [54]. The photodiodes in the balanced photodetector can be physically separated, and have much smaller area than those used in a quadrant detector because the beams can be focused without having to maintain the beam profile. Also, in a quadrant detector, the photocurrent from each diode is amplified individually before subtraction. In a balanced detector, it is possible to wire the photo-diodes in a kind of push-pull configuration and amplify only the difference current. This allows for much higher gain, higher bandwidth and lower noise. This method only measures deflection in one dimension but can be extended to two dimensions by splitting the beam into two with a beam-splitter and using two orthogonally aligned fiber bundle detectors.

The detection configuration used in this work is an improved version of the fiber bundle method, and is illustrated in Fig. 2.2. The spatial splitting of the laser is performed using a mirror with a sharp edge. Half of the beam is reflected by the mirror while the other half is not. Each half is then focused

21

onto an input of a fast balanced detector. This method has been extended for three-dimensional imaging [55], however when studying Brownian motion in fluids, one-dimensional detection is sufficient because the equation of motion has no coupling terms and can be separated into three independent equations of motion, one for each Cartesian coordinate.

In split beam detection, for bead displacements much smaller than the wavelength, the voltage signal V from the balanced photodiode is proportional to the displacement δ of the microsphere. The relationship can be written as:

$$V(d) = \Gamma P \eta Z \delta, \tag{2.7}$$

where P is the laser power, Z is the detector transimpedance gain (volts/amp), η is the sensitivity of the photodiode (amps/Watt), and Γ is the optical gain, which has dimensions of inverse length. At low frequencies, the sensitivity of split beam is typically limited by mechanical motion of detection optics. At high frequencies, it is limited by noise from the detection system, and ultimately by shot noise of the arrival rate of electrons in the photocurrent. Velocity measurement (when determined from position measurements) is most sensitive to high frequency noise. Sensitivity at high frequency can be improved by reducing noise from the detection system or by increasing optical gain. However, increasing the optical gain does not reduce the low frequency noise from mechanical vibrations.

2.2.2 Maximizing optical gain

The optical gain can be defined in terms of the dimensionless quantity $f(\delta)$:

$$f(x) \equiv \frac{\int_{-\infty}^{\infty} \int_{-\infty}^{\infty} sgn(x) I_\delta(x,y) dx dy}{\int_{-\infty}^{\infty} \int_{-\infty}^{\infty} I_\delta(x,y) dx dy}, \qquad (2.8)$$

where $I_\delta(x,y)$ is the intensity profile at the plane of the cut mirror resulting from a displacement d of the microsphere from the optical axis in the x-direction, and where $sgn(x)$ is the sign function, equal to -1 for $x < 0$, 0 for $x = 0$ and 1 for $x > 0$. $f(d)$ corresponds to the difference of the power of the two split beams normalized by their sum. For $\delta \ll \lambda$, $f(\delta) = \Gamma\delta$.

The magnitude of Γ is closely related to transverse force constant of the optical trap: The detection lens maps momentum space at the trapping plane to position space at the detection plane. Thus the momentum distribution of scattered photons, directly responsible for the trapping force, determines the intensity distribution at the detector. However, not all the photons that exert a transverse force on the trapped particle contribute to the detection signal, only those forward scattered within the finite aperture of the detection lens. An analytic calculation of Γ requires Mie scattering calculations, as is necessary for the calculation of the trapping force, but again, the limiting cases of Rayleigh scattering and ray optics provide useful quantitative and qualitative information.

In the Rayleigh scattering regime, the gain can be calculated from the intensity distribution that results from the sum of the unscattered, trapping

field and the (typically much weaker) scattered field radiated by the induced dipole. When the bead is displaced from the center of the trap, the relative phase between the scattered and unscattered fields is increased for one half of the beam and deceased on the other half. Crucial to the process is the Guoy phase shift that occurs when a Gaussian beam is focused. Thus in the far field, the scattered light is out of phase with the unscattered light and the amplitude of their sum is sensitive to small phase changes in the scattered light. The resulting (first order) optical gain is [51]:

$$\Gamma = \frac{4\sqrt{\pi}n_f d^3}{\lambda w_0^3} \frac{m^2 - 1}{m^2 + 2} \tag{2.9}$$

Where n_f is the refractive index of the fluid, d is the bead diameter, λ is the wavelength in vacuum, w_0 is the $1/e^2$ beam waist, and $m = n_b/n_f$, is the ratio of the refractive indices of the bead and fluid, where n_b is the refractive index of the bead.

The most striking feature of Eq. 2.9 is the $(d/w_0)^3$ dependence. To maximize Γ, the beam waist should be focused as tightly as possible, maximizing the overlap between the trapping field and the particle. For the same reason, the particle should be as large as possible, though Eq. 2.9 is only accurate if $d \ll \lambda$.

The ray optics approximation can be used to get a sense for the behavior of Γ for large particles. Although a sphere is far from a perfect lens, for small angles, it can be approximated as a thin lens [56] whose effective focal length (EFL), back focal length (BFL), and NA (as illustrated in Fig 2.3) are given

24
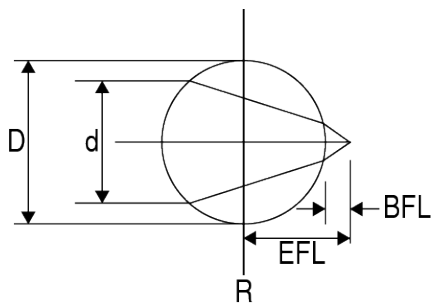
Figure 2.3: Ball lens

by:

$$EFL = \frac{md}{4(m-1)} \tag{2.10}$$

$$BFL = EFL - \frac{d}{2} \tag{2.11}$$

$$NA = \frac{2w(m-1)}{md}, \tag{2.12}$$

where m is the relative index of the sphere to the surrounding fluid, d is its diameter, and w is the diameter of the incident beam. For rays with a large angle of convergence, the approximation breaks down and spherical aberration is introduced: rays are focused at different locations depending on their distance from the optical axis.

Ray optics can be used to illustrate the dependence of Γ on the axial location of the sphere relative to the laser focus. If the sphere is aligned with the laser focus, the cone of light emerging from the sphere has the same divergence angle as the incoming light. A small transverse displacement δ of the sphere results in a tilt of the refracted cone by an angle $\phi = \delta/EFL$. This corresponds to a shift in the intensity distribution at a distance D from

the sphere by a distance $\Delta = D\delta/EFL$. Assuming, for simplicity, a uniform intensity distribution with angular width θ, the change in the normalized signal caused by a bead displacement δ is

$$f(\delta) - f(0) = \frac{2\phi\theta}{\pi\theta^2} = \frac{8\delta(m-1)}{\pi\theta md}, \tag{2.13}$$

and the corresponding optical gain is

$$\Gamma = \frac{8(m-1)}{\pi m} \frac{1}{\theta d} \tag{2.14}$$

The gain improves with smaller bead size and smaller width of the incident beam. It is advantageous to use as shallow of a detection focus as possible. However, if the focus is too shallow, the waist of the detection beam may be larger than the sphere, and the sphere will not interact with the entire trapping field. The minimum angle of convergence such that the beam waist is the size of the bead is $\theta_0 = \lambda/\pi d$. The resulting optical gain is independent of d:

$$\Gamma = \frac{8(m-1)}{m\lambda} \tag{2.15}$$

Another possible detection configuration is shown in Fig. 2.4, with the bead displaced axially from the detection beam focus.

The lensing effect of the sphere can be taken advantage of by shifting it forward such that its focal point overlaps the focus of the detection beam. An incoming beam with angle of divergence θ will be collimated by the sphere, the outgoing collimated beam having waist $w_0' = \theta_0 EFL$. In a ray optics picture, the collimated beam will have the same waist w_0' at any distance D from the

26
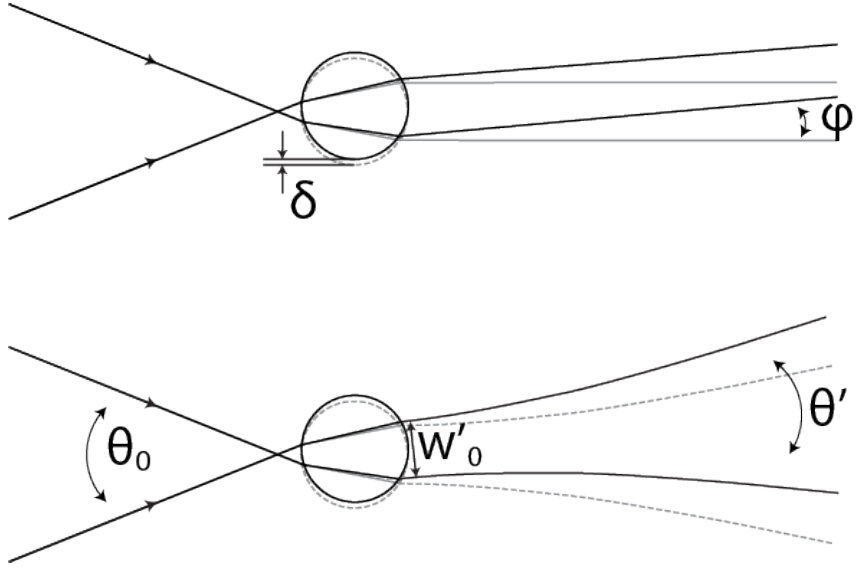
Figure 2.4: Beam deflection by a sphere in front of the focus.

bead, but its displacement from the optical will increase indefinitely: $\Delta = \phi D$ with $\phi = \delta/EFL$. In this limit, Γ is proportional to D, which can be made arbitrarily large.

Physically, this is impossible, because a laser beam cannot be perfectly collimated. A Gaussian beam with waist w_0 begins to diverge when $D > z_R$, where $z_R = \pi w_0^2/\lambda$ is the Rayleigh range. The $1/e^2$ half-angle of divergence is $\theta = \lambda/\pi w_0$. Thus the refracted beam has an angle of divergence $\theta' = \lambda/(\pi\theta_0 EFL)$. The resulting change in f is

$$f(\delta) - f(0) = \frac{2\phi\theta'}{\pi\theta'^2} = \frac{2\pi\delta\theta_0 EFL}{\pi\lambda EFL} = \frac{2\delta\theta_0}{\lambda}, \tag{2.16}$$

and resulting optical gain, $\Gamma = 2\theta_0/\lambda$, also independent of particle size, but is limited by the NA of the sphere, whose maximum is $2(m+1)/m$.

27

The above estimates must be understood as an upper limit. However it is interesting that both configurations predict almost the same value for maximal Γ, in both cases independent of particle size. For any size bead it is advantageous to use short wavelength light and microspheres with high refractive index.

2.2.3 Sources of noise

Noise in the output of the balanced detector can come from a variety of sources. These include laser intensity noise, laser pointing noise, mechanical vibration of the trapping and detection optics, quantum fluctuations of laser intensity at the detector inputs and electronic noise from the balanced photodetector circuit.

The power of the detection laser typically has small fluctuations about its mean value: $P(t) = P_0 + P_n(t)$, with $\langle P_n \rangle = 0$. The output of the detector in the presence of such noise will be $V(t) = P(t)\Gamma\eta Z\delta(t)$. The measured position of the particle, δ_m is inferred by dividing $V(t)$ by the average total gain $P_0\Gamma\eta Z$, and power fluctuations will result in the addition of a noise term: $\delta_m(t) = \delta(t) + \delta_{PF}(t)$, where $\delta_{PF}(t)$ is the effective position noise due to power fluctuations, given by:

$$\delta_{PF}(t) = \frac{P_n(t)\delta(t)}{P_0}, \tag{2.17}$$

The amount of cancellation of intensity fluctuations depends on the alignment of the cut mirror. Misalignment of the cut mirror effectively adds a constant displacement to the otherwise zero-mean fluctuations: $\delta'(t) = \bar{\delta} + \delta(t)$ if $\bar{\delta} \gg$

28

δ_{rms}, then most of the contribution from position noise will come from the term $P_n(t)\bar{\delta}/P_0$. The power spectral density (PSD) of δ_{PF} will be:

$$S_{\delta_{PF}} = \frac{S_{P_n}\bar{\delta}^2}{P_0^2} \tag{2.18}$$

where S_{P_n} is the PSD of the laser intensity noise. Perfect alignment of the cut mirror, however, will not completely eliminate the effect of intensity noise. If $\bar{\delta} = 0$, there remains the term $P_n(t)\delta(t)/P_0$. This can be thought of as the intensity noise modulated by the envelope of $\delta(t)$. The effect of laser intensity noise will then be

$$S_{\delta_{PF}} = \frac{S_{P_n}\bar{\delta^2}}{P_0^2} \tag{2.19}$$

where $\bar{\delta^2}$ is the variance of $\delta(t)$.

Laser pointing noise, and mechanical vibration of the trapping and detection optics result in motion of the laser relative to the cut mirror that is not caused by motion of the trapped particle. Laser pointing noise can be eliminated by fiber coupling the laser into a single mode fiber, but vibration of the optics is difficult to minimize. Vibration can be transferred through the ground via the optical table or acoustically through sound waves in the air. There is no easy way to eliminate this noise. The spectrum of mechanical vibrations typically falls off as $1/f$, and thus dominates at low frequency. However mechanical vibration also contributes to the $\bar{\delta^2}$ coefficient which determines the leakage of laser intensity noise.

Electronic noise from the detector consists of $1/f$ drift-type noise as well as white-spectrum thermal noise from resistors and op-amps within the

circuit. Velocity measurement is more sensitive to high frequency noise, so $1/f$ noise is not as much of a concern as the high frequency white noise, though with careful detector design this can be reduced below the level of white noise contributed from photon shot noise, which imposes the fundamental limit to noise at high frequencies.

For photons in a laser beam, arrival times obey the statistics of a Poisson process. The 'power' of a single photon is a delta function with the area of the photon's energy, $P_0(t) = h\nu\delta(t)$. A beam with constant power $\bar{P}$ has a photon rate of $\bar{r} = \bar{P}/h\nu$, thus the statistical fluctuations of the power in the laser have a spectrum of:

$$S_P = \frac{\bar{P}}{h\nu}(h\nu)^2 = \bar{P}h\nu \tag{2.20}$$

If the photodiodes have quantum efficiency q (photoelectrons per photon), The effective position noise as a result of this shot noise is

$$S_{\delta_{SN}} = \frac{S_P}{(qP\Gamma)^2} = \frac{h\nu}{qP\Gamma^2} \tag{2.21}$$

The absolute photon shot noise scales with $\sqrt{P}$, but the signal scales linearly, thus the noise floor in the position signal decreases as $1/\sqrt{P}$. If all technical noise sources are driven below the shot noise level, the shot noise can be reduced by increasing the power. The maximum power can be limited by technical constraints of generating and detecting a high power laser beam, but will ultimately be limited by absorption and heating of the trapped particle or fluid.

2.3 Effects of noise and bandwidth on position and velocity measurement

The practical process of determining velocity from position measurements is far from trivial, especially in the presence of noise and limited bandwidth. There are different methods by which velocity can be estimated and noise filtered out. This section gives a discussion of ways in which measured velocity can deviate from the 'real' velocity, and strategies to quantify and minimize this deviation.

2.3.1 Effects of noise

Velocity measurement is particularly sensitive to the high frequency components of the position measurement noise. As discussed above, the dominant source of noise at high frequencies is photon shot noise, which has a flat spectrum. Figures 2.5, 2.6 and 2.7 illustrate effect of adding white noise to a simulated trajectory of a Brownian particle. The top graph of Fig. 2.6 shows a sample of the simulated position with and without noise. While the noise appears small relative to the position signal, when the the velocity is calculated by differentiating the position (bottom of Fig. 2.6), the velocity of the noise completely dominates that of signal.

The reason for this can be understood by looking at the power spectral densities (PSD) of the position (S_x and velocity (S_v signals. The PSD of a fluctuating signal represents the relative contribution of the various Fourier components of the signal to the signal's total variance. The area of a PSD
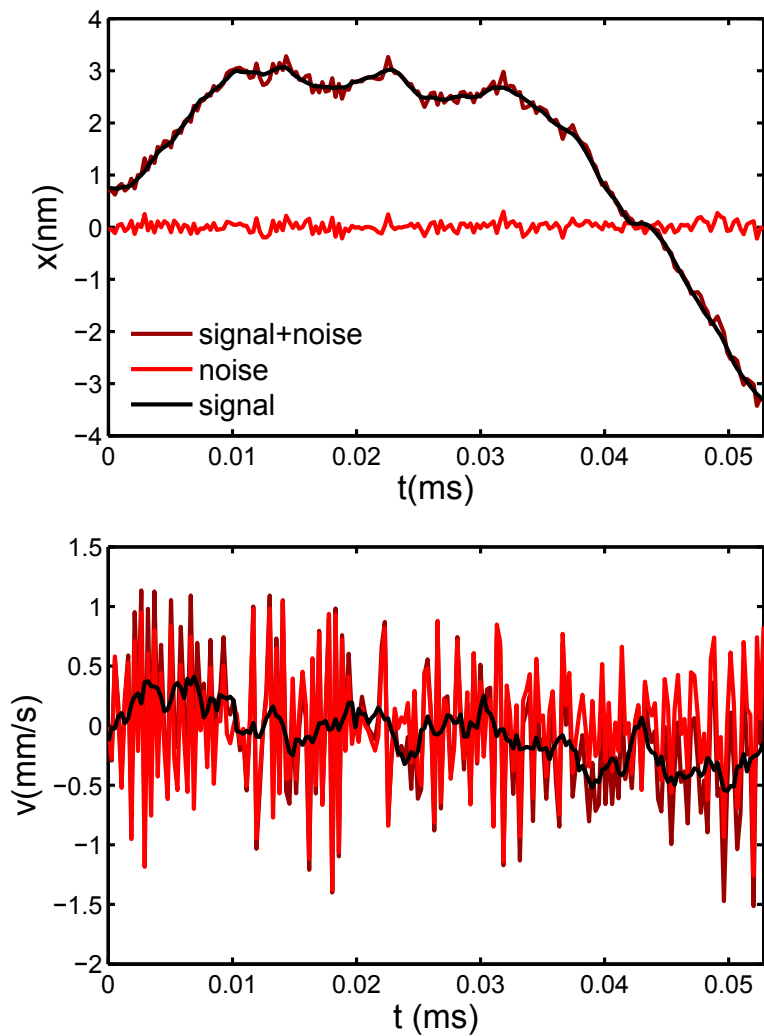
Figure 2.5: Sample of the position and velocity of a simulated Brownian trajectory, with and without noise. Position (top) and corresponding velocity (bottom) of a simulated Brownian trajectory (black curve), as well as simulated white noise (red curve) and the resulting noisy trajectory (brown curve). While the noise is small relative to the position signal, it dominates the velocity signal.
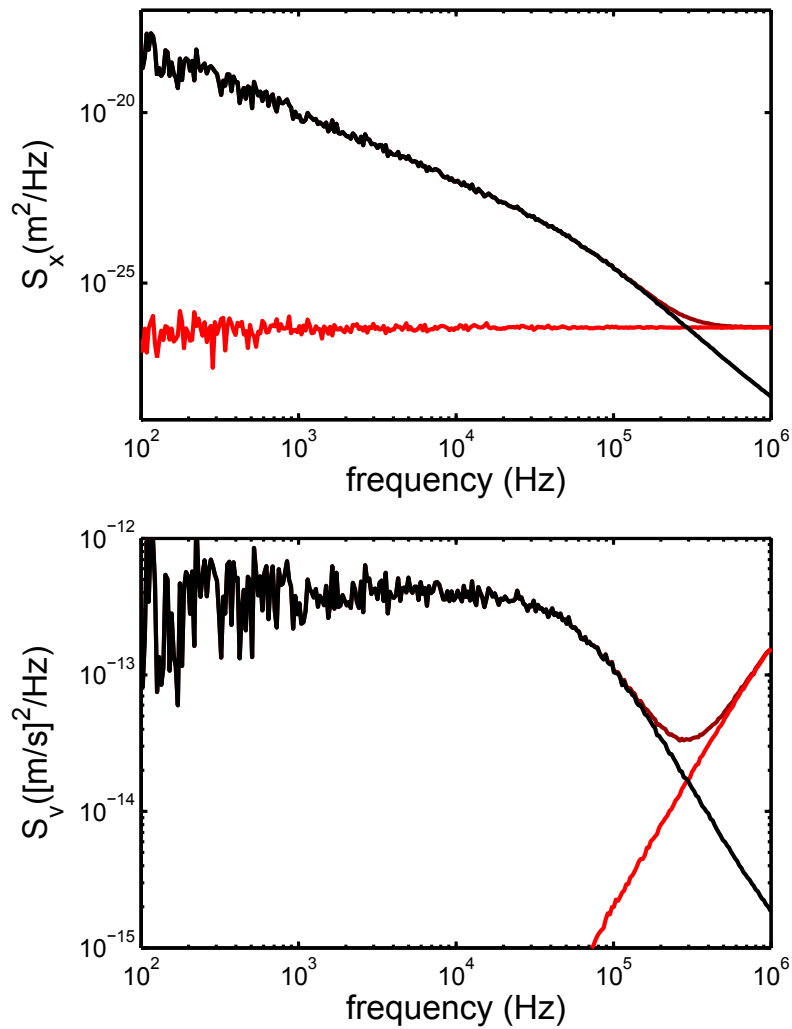
Figure 2.6: The position (top) and velocity (bottom) PSDs corresponding to a simulated Brownian trajectory, a sample of which is shown in Fig. 2.5. When differentiated, the white noise in position measurement becomes noise with slope 2 in the velocity.

gives the variance of the signal. For this discussion, the details the particular form of the PSDs for a Brownian trajectory are not important (the theory is discussed in detail in Chapters 3 and 6). The upper graph in Fig 2.6 shows the PSDs of the position signal and noise. The spectrum of the white noise is flat, while that of the position decreases with increasing frequency. For most frequencies, the signal dominates the noise, and the area of the signal spectrum is larger than that of the noise.

The lower graph of Fig. 2.6 shows the PSD of the velocity. The position and velocity PSD are closely related: $S_v = \omega^2 S_x$. Thus white noise in position, when differentiated, results in a noise with PSD of slope 2 on a log-log plot. The result of differentiation is that the high frequency components of both the signal and noise contribute more to the velocity variance than to that of the position. For velocity, the frequency range over which noise dominates the signal is the same, but its relative contribution to the final signal-to-noise ratio (SNR) is much more significant than it was for position. The logarithmic scale can be misleading when visually estimating the area.

The lower graph of Fig. 2.7 shows the cumulative distribution of the velocity PSD (CS_v), calculated by integrating S_v from zero to f. The vertical axis is on a linear scale, and it is more evident from this plot the frequency range at which the noise begins to dominate the signal. The CS_v of the noiseless velocity has a sigmoidal shape. Most of the contribution comes from intermediate frequencies, and at high frequencies it approaches an asymptotic value which represents the mean-square instantaneous velocity. The CS_v of
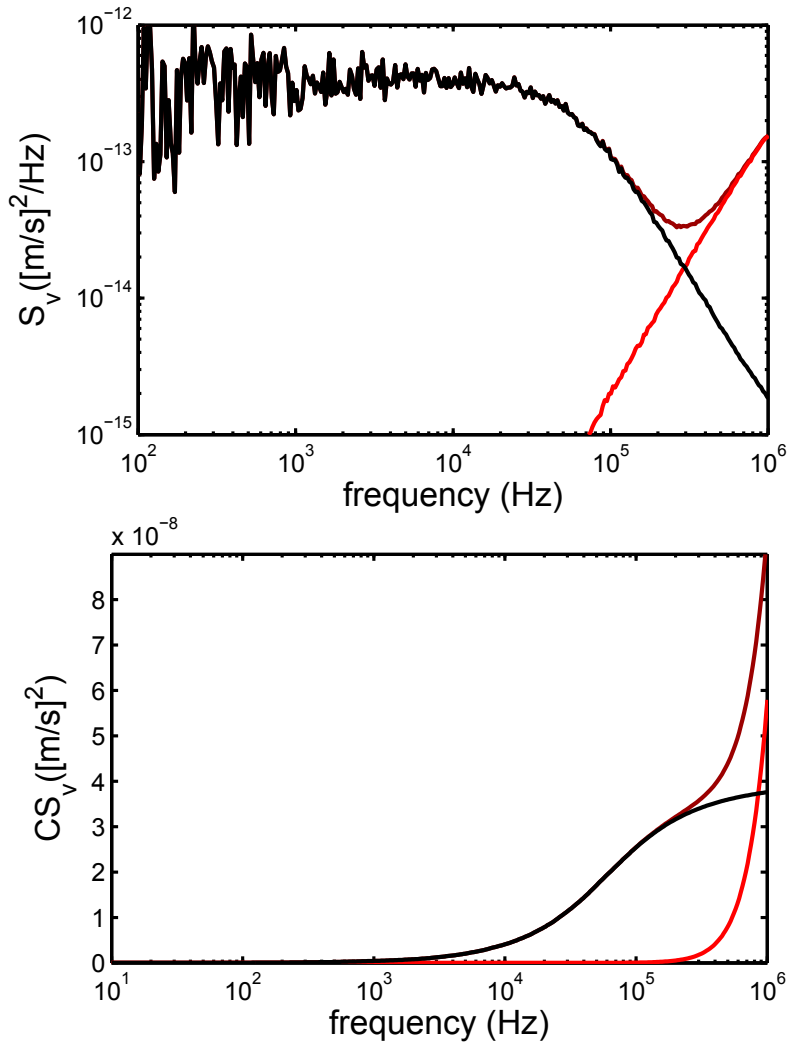
Figure 2.7: The velocity PSD (top) and corresponding cumulative velocity PSD corresponding to a simulated Brownian trajectory, a sample of which is shown in Fig. 2.5. In the cumulative PSD it is more clear at which frequencies the noise begins to become significant relative to the signal.
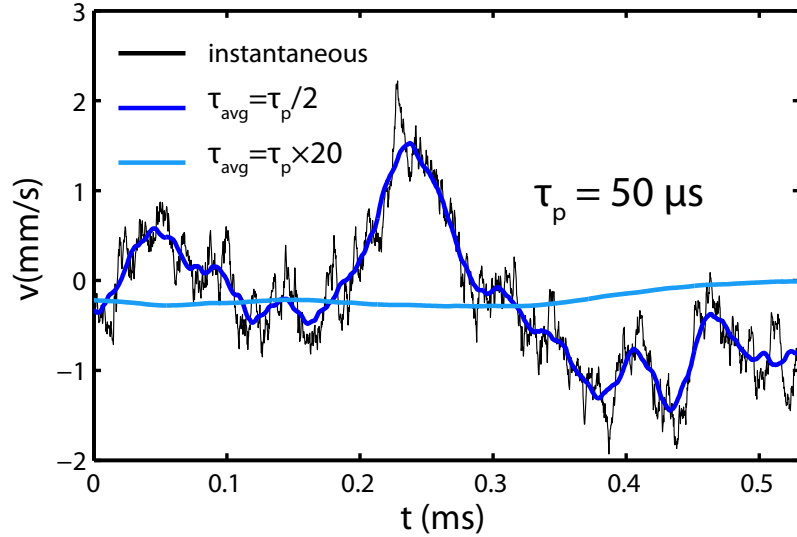
Figure 2.8: Sample of simulated Brownian velocity (black curve), and the result of filtering with two different window sizes; $\tau_p/2$ (blue curve) and $20\tau_p$ (cyan curve). The characteristic time scale for velocity fluctuations in this simulation is $\tau_p = 50\mu s$.

the noise grows as ω^3, transitioning rapidly from being negligible to being many orders of magnitude greater than the signal.

In order to measure velocity with high SNR, it is necessary to perform low pass filtering of the position data prior to differentiation. Low pass filtering suppresses the noise, but also suppresses the signal. If the low-pass frequency is too low, the filtering will reduce the variance of the signal as well as that of the noise.
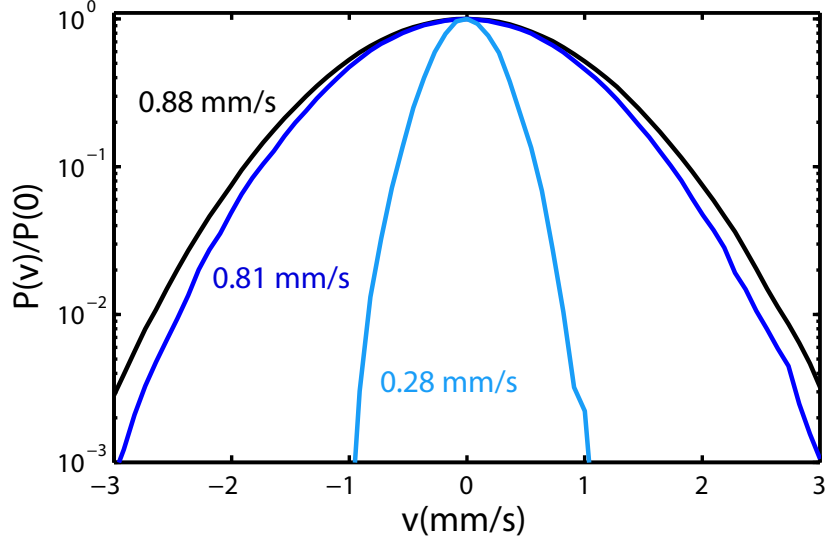
Figure 2.9: Normalized velocity distribution for unfiltered and filtered velocity of a simulated Brownian trajectory, a sample of which is shown in Fig. 2.8. The filtered velocity has narrow distribution than the unfiltered velocity, because filtering suppresses high frequency components that contribute to the total width of the distribution

2.3.2   Effects of low-pass filtering

Figures 2.8, 2.9 and 2.10 illustrate the effects of filtering on the velocity of a simulated Brownian trajectory. Velocity fluctuations of Brownian particles have a characteristic time scale associated with them known as τ_p. The velocity in this simulation was generated with, τ_p was set to 50 μs. A sample of the velocity is shown in Fig. 2.8, along with the results of filtering the velocity with running-average filters: a 'fast' filter with a window size of $\tau_p/2$, and a 'slow' filter with a window size of $20\tau_p$. The fast filter suppresses only the short time fluctuations while the slow filter suppresses most of the fluctuations.

One of the main goals of this work is to measure the velocity distribution, thus it is important to understand how it is affected by low-pass filtering. The distribution of the instantaneous velocity and filtered velocities are shown in Fig. 2.9. The effect of low pass filtering is to make the distribution narrower. The mean square velocity of the trajectory determines the associated mean kinetic energy, and thus effective temperature of the Brownian particle. Low pass filtering results in narrow distributions; some of the kinetic energy (that contained at high frequencies) is suppressed by the filter.

Figure 2.10 shows the S_v and CS_v for raw and filtered signals. The ripples in the filtered velocity spectrum are an artifact of the filtering method. Filtering has negligible effect at low frequencies but suppresses components contained at high frequencies. The cumulative spectrum can be interpreted as showing how the variance of the filtered signal depends on the frequency of the low-pass filter.

If the filter frequency is such that, at that frequency, CS_v of the signal is flat, and has reached its asymptotic value, then the statistics of the filtered signal will closely match the real signal. If CS_v is less than its asymptotic value at the filter frequency, then the will deviate significantly from the real signal.
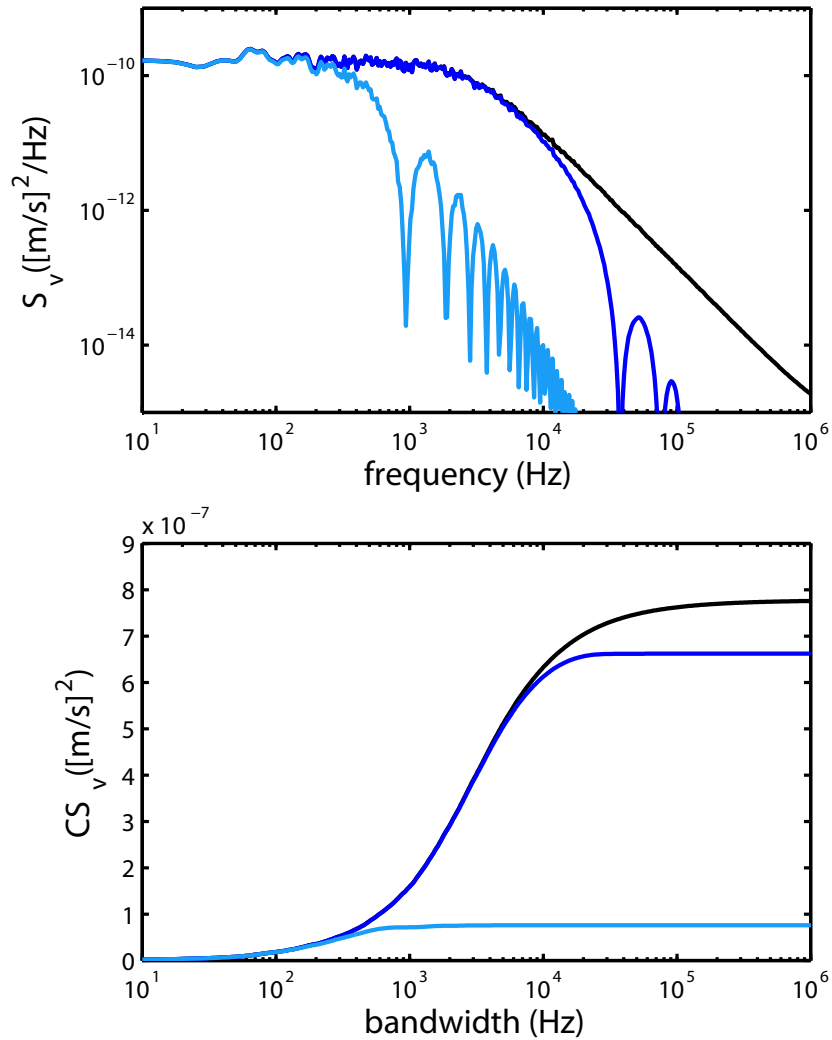
Figure 2.10: Velocity PSD (top) and cumulative velocity PSD (bottom) for for unfiltered and filtered velocity of a simulated Brownian trajectory, a sample of which is shown in Fig. 2.8. The spectral distribution illustrates the effect of filter frequency on the resulting variance. The cumulative PSDs for the filtered velocities begin to plateau at the low-pass filter frequency, and do not reach the asymptotic value of the instantaneous velocity.

39

Chapter 3

Einstein-Ornstein-Uhlenbeck theory of Brownian motion

The force exerted on a moving sphere by a fluid depends on the history of the sphere's motion. The characteristic time scale of the 'memory' of this force is τ_p, and is discussed in Ch. 6. If changes in the sphere's velocity occur over time scales longer than τ_p, then the force on the sphere can be approximated as the force on a sphere moving at constant velocity for all time, which is $F_{fr} = -\gamma_s v$, where γ_s is the Stokes damping coefficient for the particle. For a for a sphere with radius r in a fluid with dynamic viscosity η, Stokes law gives: $\gamma_s = 6\pi\eta r$.

If Stokes damping is assumed for the Brownian motion of a particle with mass m_p, the result predicts that the time scale for velocity fluctuations will be $\tau_p = m_p/\gamma_s$. If τ_p is comparable to τ_f, the assumption of Stokes damping is invalid, and the memory effect must be taken into account. However, if $\tau_p \gg \tau_f$, the assumption is valid. This is the case for Brownian motion of dielectric microspheres in gas. The resulting theory is known as Einstein-Ornstein-Uhlenbeck theory, and its results are presented in this chapter. When the memory effect is taken into account, the corresponding theory increases in

complexity due to the coupling between the Brownian motion and the hydro-dynamic memory. Those results will be discussed in Ch. 6.

In all of the following derivations, $\langle \ldots \rangle$ formally represents an average over many identical systems started at the same initial conditions each with different $F_{th}(t)$. This is not *a priori* equivalent to the time average of equilibrium motion of a single particle.

$$\langle f(t_1, t_2) \rangle \overset{?}{=} \lim_{T \to \infty} \frac{1}{T} \int_0^T f(t, t + t_2 - t_1) dt. \tag{3.1}$$

The ergodic theorem posits that it is true, although it has only been proven for specific cases.

3.1 Einstein vs Langevin

Einstein's seminal paper on Brownian motion contained two major results. The first is his expression for the mean-square displacement of a free Brownian particle:

$$\langle [\Delta x(t)]^2 \rangle = 2Dt \tag{3.2}$$

where $\langle [\Delta x(t)]^2 \rangle \equiv \langle (x(t) - x(0))^2 \rangle$ is the MSD of a free Brownian particle in one dimension for time interval t, and D is the diffusion constant. The second result was a derivation of an expression for the diffusion constant, which combined thermodynamics and mechanics:

$$D = k_B T / \gamma_s \tag{3.3}$$

Where k_B is Boltzmann's constant T is the temperature [4].

41

Using 3.2 to determine the mean squared average velocity in time interval t gives $\sqrt{\langle \bar{v}_t^2 \rangle} \equiv \sqrt{\langle [\Delta x(t)]^2 \rangle}/t = \sqrt{2D}/\sqrt{t}$, which diverges as $t \to 0$. Since equipartition predicts a well defined (and certainly finite) mean squared instantaneous velocity of $\sqrt{\langle \bar{v}_0^2 \rangle} = k_B T/m_p$, where m_p is the mass of the particle, 3.2 must break down below some time scale.

A more complete description of Brownian motion can be obtained from the Langevin equation [5, 7, 13]:

$$m_p \ddot{x}(t) = -\gamma_s \dot{x}(t) + F_{th}(t) \tag{3.4}$$

where $\dot{x}$ and $\ddot{x}$ are the particle's velocity and acceleration, respectively, and F_{th} is the instantaneous thermal force exerted on the particle by random collisions with fluid molecules. In fact, the damping term is also caused by collisions with molecules; it is the deterministic part of that force, and can be determined by measuring the response to an external force. F_{th} is the part of the force exerted by the fluid which deviates from the deterministic, average force.

When the $m_p \ddot{x}$ term in the Langevin equation is ignored, the resulting dynamics correspond Einstein's prediction. This inertial term is negligible for times $t \gg \tau_p$, and the predictions of the Langevin equation agree with those of Einstein at long time scales. This is known as the diffusive regime. At shorter times, the two predictions diverge. Over very short time intervals $(t \ll \tau_p)$, in what is known as the ballistic regime, the dominant force is that of the particle's inertia and trajectories are approximately straight lines with constant velocity. Solutions of the Langevin equation contain an account of the
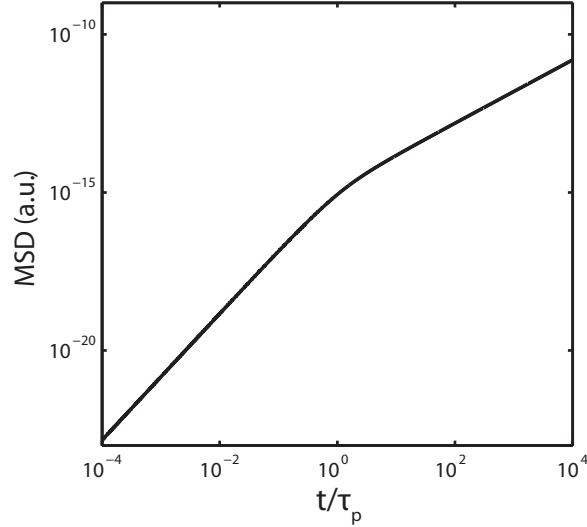
Figure 3.1: Double logarithmic plot of the mean square displacement of a free particle given by Eq. 3.5.

transition between ballistic and diffusive motion. It is within this transition that velocity fluctuations occur.

3.2   Solutions for a free particle

One of the fundamental properties of a Brownian particle's trajectory is its mean square displacement. It is fundamental because it can be easily determined from a recorded trajectory, and its t-dependence reveals much of the underlying dynamics.For a free particle, Eq. 3.4 predicts a mean-square displacement of:

$$\langle [\Delta x(t)]^2 \rangle = \frac{2\tau_p^2 k_B T}{m_p} \left(\frac{t}{\tau_p} - (1 - e^{t/\tau_p}) \right) \tag{3.5}$$

43
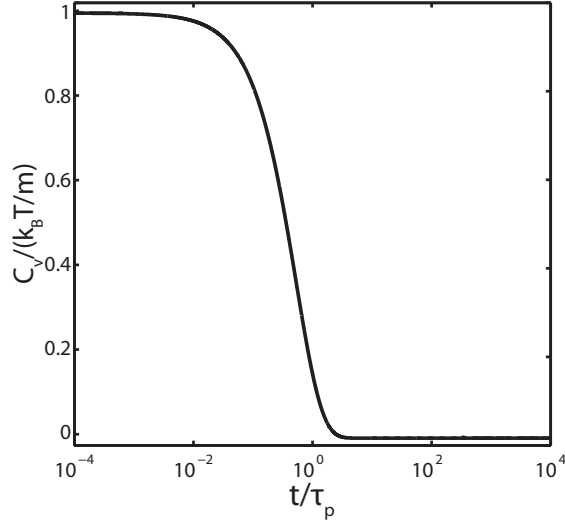
Figure 3.2: Semi logarithmic plot of the velocity autocorrelation of a free particle given by Eq. 3.8.

which is plotted in Fig. 3.1. For $t \gg \tau_p$, Eq. 3.5 reduces to Einstein's prediction:

$$\langle [\Delta x(t)]^2 \rangle = 2Dt \tag{3.6}$$

which corresponds to a line with slope 1 on a log-log plot. For $t \ll \tau_p$, Eq. 3.5 describes ballistic (constant-velocity) motion:

$$\langle [\Delta x(t)]^2 \rangle = \frac{k_B T}{m_p} t^2. \tag{3.7}$$

which corresponds to a line with slope 2 on a log-log plot.

Closely related to the mean square displacement is the velocity auto-correlation function $C_v(t)$, which describes the time-dependence of velocity fluctuations. For a free particle, the prediction from Eq. 3.4 is:

$$C_v(t) = \frac{k_B T}{m_p} e^{-|t|/\tau}. \tag{3.8}$$

44

which is shown in Fig. 3.2. $C_v(t)$ is actually proportional to the second derivative of the MSD with respect to time. In the ballistic regime $C_v = k_B T / m_p$, equal to the mean squared thermal velocity. In the transition to the diffusive regime, C_v decays exponentially to zero; in the diffusive regime the velocity is uncorrelated.

The Fourier transform pairs of the MSD and velocity autocorrelation are the position and velocity power spectral densities, S_x and S_v [1]. The power spectral density of a signal conveys information about underlying physical processes, and the effect of noise to its measurement, in a more direct way than the temporal correlation functions. For a stationary process $u(t)$, the total area of S_u gives the variance of u, $\langle u^2 \rangle$. $S_u(\omega)$ quantifies the relative contribution of fluctuations near frequency ω to the total variance. Equation 3.4 predicts position and velocity power spectral densities of:

$$S_x = \frac{2\gamma k_B T}{m_p^2 \omega^4 + \omega^2 \gamma^2} \tag{3.9}$$

$$S_v = \frac{2\gamma k_B T}{m_p^2 \omega^2 + \gamma^2} \tag{3.10}$$

which are shown in top panels of Figs. 3.3 and 3.4 for different γ_s. The slope of S_x in the two different regimes corresponds to that of the MSD.
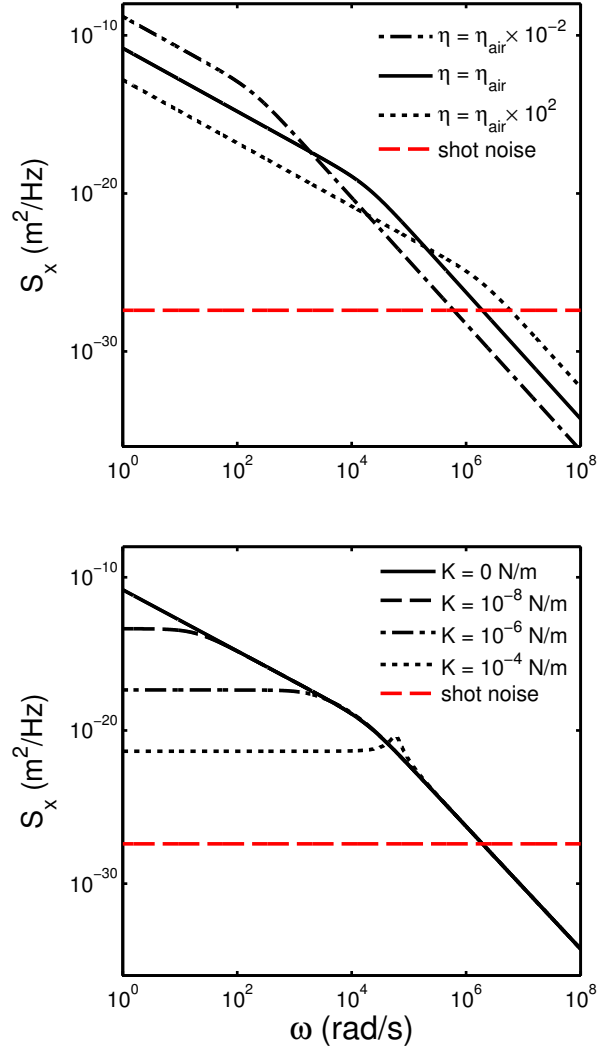
Figure 3.3: Position PSDs predicted by EOU theory. Top: plot of Eq. 3.9 for a free particle with varying viscosity. Bottom: plot of Eq. 3.12 for a particle in a harmonic trap with varying trap strengths.
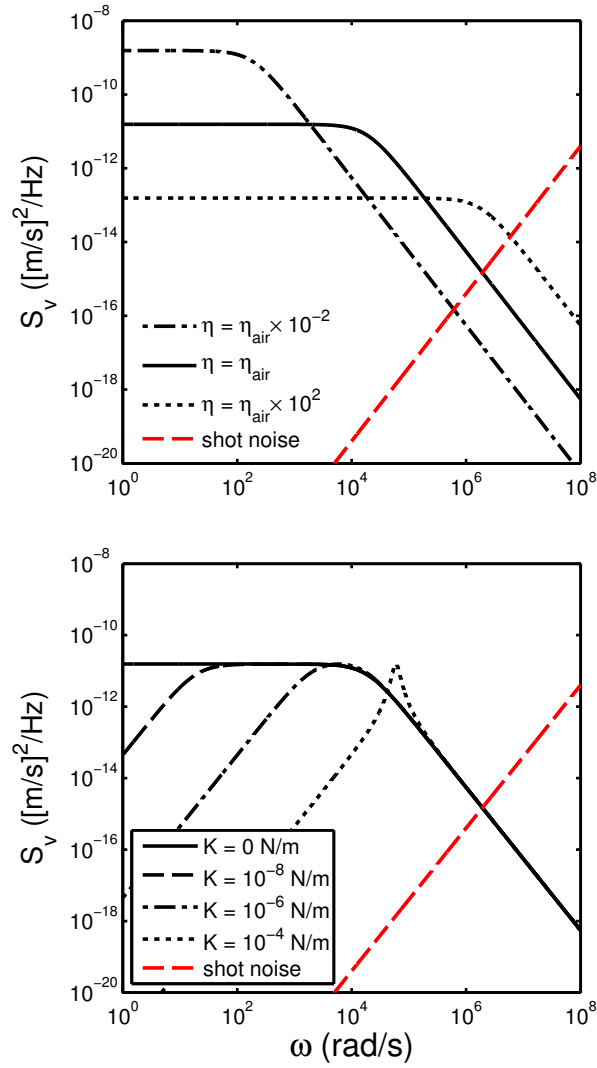
Figure 3.4: Velocity PSDs predicted by EOU theory. Top: plot of Eq. 3.10 for a free particle with varying viscosity. Bottom: plot of Eq. 3.13 for a particle in a harmonic trap with varying trap strengths.

3.3 Brownian motion in a harmonic potential

To correctly describe brownian motion in an an optical trap, it is necessary to include the trapping force $F = -Kx$ in the Langevin equation, where K is the trap spring constant:

$$m_p \ddot{x}(t) = -\gamma_s \dot{x}(t) - Kx + F_{th}(t). \tag{3.11}$$

For a Brownian particle in a harmonic potential, the position and velocity PSDs are:

$$S_x = \frac{2\gamma k_B T}{m_p^2 (\omega_0^2 - \omega^2)^2 + \omega^2 \gamma^2} \tag{3.12}$$

$$S_v = \omega^2 S_x = \frac{2\omega^2 \gamma k_B T}{m_p^2 (\omega_0^2 - \omega^2)^2 + \omega^2 \gamma^2} \tag{3.13}$$

Where $\omega_0 = \sqrt{K/m_p}$ is the characteristic frequency of the harmonic potential. The effect of different trap strengths on the position and velocity PSDs is in the lower panels of Figs. 3.3 and 3.4. There is a qualitative crossover in behavior at $\omega_0 = 1/2\tau_p$. When $\omega_0 < 1/2\tau_p$, the system is overdamped; the effect of the potential occurs only in the diffusive regime. In the overdamped case, there are three different regimes defined by the characteristic frequencies: $\omega_k \equiv \omega_0^2 \tau_p$ and $\omega_p \equiv 1/\tau_p$. For $\omega < \omega_k$, S_x is constant; the amplitude of oscillations is limited by the harmonic potential. For $\omega_k < \omega < \omega_p$, $S_x \propto \omega^{-2}$ (slope -2 on a log-log plot). In this regime, the amplitude of motion is limited by Stokes

---

[1]S_x is the Fourier transform of the position autocorrelation, which differs from the MSD by a factor of -2 and an offset of $\langle x^2 \rangle$, the mean-square position. For a free particle, $\langle x^2 \rangle = 0$, thus the position autocorrelation is not well defined, and this corresponds to a divergence of S_x as $\omega \to 0$.
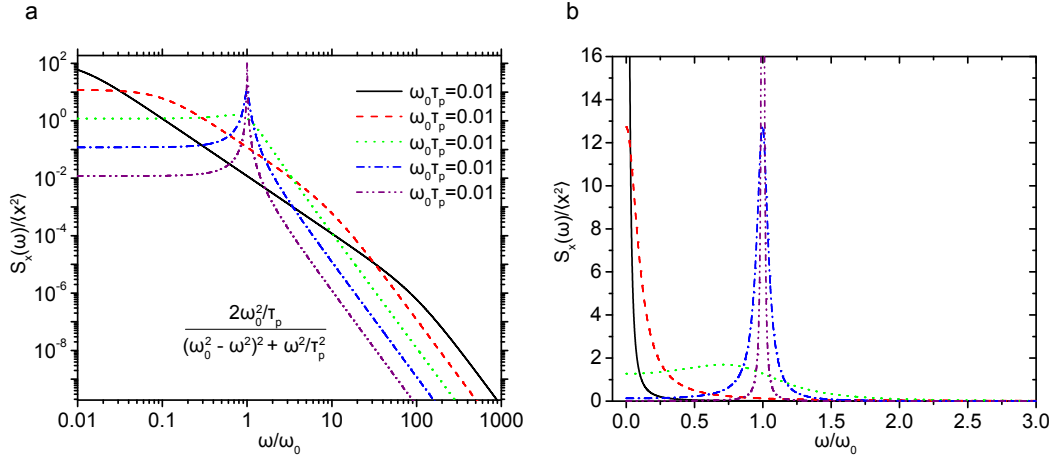
Figure 3.5: Normalized position PSD for various levels of $\omega_0\tau_p$, shown on a (a) double-logarithmic scale and (b) linear scale. The horizontal axis is normalized by ω_0. Image courtesy of Tongcang Li.

damping, while the restoring force of the trap is negligible in comparison to viscous forces. For $\omega > \omega_p$, S_x has slope -4 on the log-log plot. This regime is dominated by the inertial force; the velocity is small enough that damping forces are negligible compared to the inertial force necessary to accelerate the particle.

When $\omega_0 > 1/2\tau_p$, the system is underdamped. The effect of the potential occurs in the ballistic regime, and thus the particle will tend to oscillate multiple times within the trap before its motion is damped out. In that case S_x develops a resonant peak centered near ω_0. The bead's Brownian motion appears less like a random walk and more like sinusoidal oscillation with noisy phase. The weaker the damping, the narrower and taller the resonant peak.

49

The MSD and C_v corresponding to the overdamped case are:

$$\text{MSD}(t) = \frac{2k_BT}{m_p\omega_0^2}\left[1 - \frac{1}{2|\omega_1|\tau'_+}e^{-t/\tau'_-} + \frac{1}{2|\omega_1|\tau'_-}e^{-t/\tau'_+}\right]. \tag{3.14}$$

$$C_v(t) = \frac{k_BT}{m_p}\left[-\frac{1}{2|\omega_1|\tau'_-}e^{-t/\tau'_-} + \frac{1}{2|\omega_1|\tau'_+}e^{-t/\tau'_+}\right], \tag{3.15}$$

Where $\omega_1 = \sqrt{\omega_0^2 - (2\tau_p)^{-2}}$ is the corner frequency, and

$$\tau'_\pm = \frac{2\tau_p}{1 \pm 2\tau_p|\omega_1|}. \tag{3.16}$$

while in the underdamped case, the MSD and C_v are:

$$\text{MSD}(t) = \frac{2k_BT}{m_p\omega_0^2}\left[1 - e^{-t/2\tau_p}\left(\cos\omega_1 t + \frac{\sin\omega_1 t}{2\omega_1\tau_p}\right)\right], \tag{3.17}$$

and

$$C_v(t) = \frac{A}{2\gamma_s m_p}\left(\cos\omega_1 t - \frac{\sin\omega_1 t}{2\omega_1\tau_p}\right)e^{-t/2\tau_p} \tag{3.18}$$

3.4 Equilibrium instantaneous velocity probability distribution

Statistical mechanics predicts a Maxwell Boltzmann distribution for the velocity of an ensemble of Brownian particles. At a fixed instant in time, the probability that a randomly chosen particle has a (one-dimensional Cartesian component of) velocity between v_i and $v_i + dv_i$ is given by $p(v_i)dv_i$, where:

$$p(v_i) = \frac{m_p}{2\pi k_BT}\exp\left(-\frac{m_pv_i^2}{2k_BT}\right) \tag{3.19}$$

However, we perform experiments on single particles, and are interested in the velocity distribution of that particle's velocity as it fluctuates in time. We

50
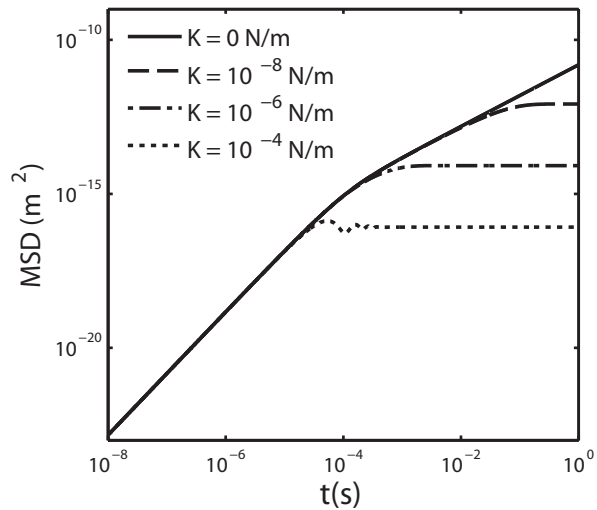
Figure 3.6: Double logarithmic plot of the mean square displacement of a particle in a harmonic potential given by either Eq. 3.17 or 3.14.
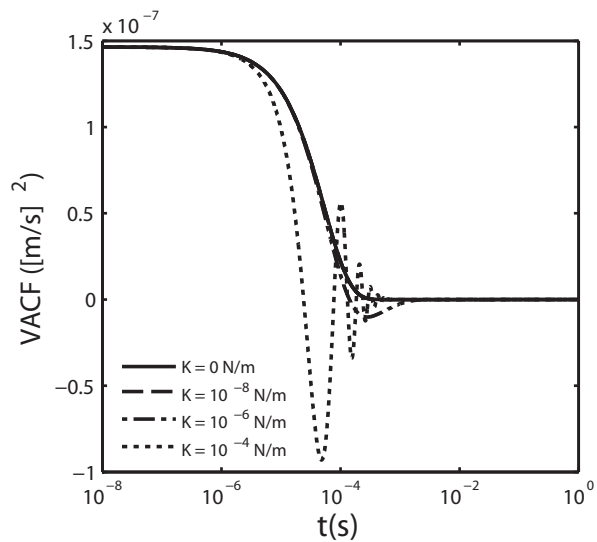
Figure 3.7: Semi logarithmic plot of the velocity autocorrelation of a free particle given by particle in a harmonic potential given by either Eq. 3.18 or 3.15.

would like to know whether, for a single particle, with velocity v_0 at $t = -\infty$, for an arbitrarily chosen $t > 0$, the probability of $v(t)$ to lie between v and $v + dv$ is given by the same probability density as that in Eq. 3.19.

The ergodic theorem predicts that the answer is yes, however, the ergodic theorem not been universally proven. This is one of the reasons why it is important to measure the velocity of a single Brownian particle and experimentally determine whether its distribution is the same as predicted by the equipartition theorem.

Chapter 4

Trapping and detection of microspheres in air

To date, the majority of experimental study of Brownian motion has concentrated on that of particles in water. Other than initial trapping, all other aspects of measurement of the velocity of Brownian particles are simpler in air than in water. The dynamics of velocity fluctuations of Brownian motion in air occur over longer time scales than in water, allowing for longer averaging time for position measurements and thus much better signal-to-noise in velocity measurement.

This section describes our experimental setup for launching and trapping microspheres in air and vacuum. The same setup was also used to perform active 3D cooling of the center of mass motion of a trapped microsphere to mK temperatures [55].

4.1   Launching microspheres in air

In vacuum, dielectric surfaces attract each other by the van der Waals force: surface charge of opposite polarity is spontaneously induced on both surfaces resulting in electrostatic attraction [57]. When two surfaces are immersed in water, the polar water molecules screen the surface charge and substantially

reduce the attraction between the two dielectric . In air, the screening effect is negligible, and glass microspheres in air adhere to each other and to any surface with which they come into contact.

The minimum force necessary to separate two surfaces is known as the "pull off" force. The pull off force between a microsphere and a flat surface is [58,59]

$$F_{\text{sphere-flat}} = 4\pi r\Gamma, \tag{4.1}$$

where r is the radius of the microsphere and Γ is the effective solid surface energy. The pull-off force between two identical spheres is

$$F_{\text{sphere-sphere}} = 2\pi r\Gamma, \tag{4.2}$$

half that between a sphere and a plane. In reference [59], the pull-off force between two 1 μm diameter silica microspheres was measured to be about 88 nN, and the force between such a microsphere and a flat silica surface was measured to be 176 nN. In comparison, the gravitational force on the same size bead is $\sim$ 10 fN, while the maximum force that can be exerted by an optical tweezer is $\sim$ 0.1 nN. Both of these are far too small to overcome the pull-off force.

A simple method to separate a bead from a surface is to apply to the surface an acceleration sufficiently large such that the resulting inertial force overcomes the attractive force. The required acceleration to separate a bead from a flat surface scales as r^{-2}. For the 1 μm diameter microsphere, the required acceleration is $\sim 2 \times 10^8$ m/s^2.
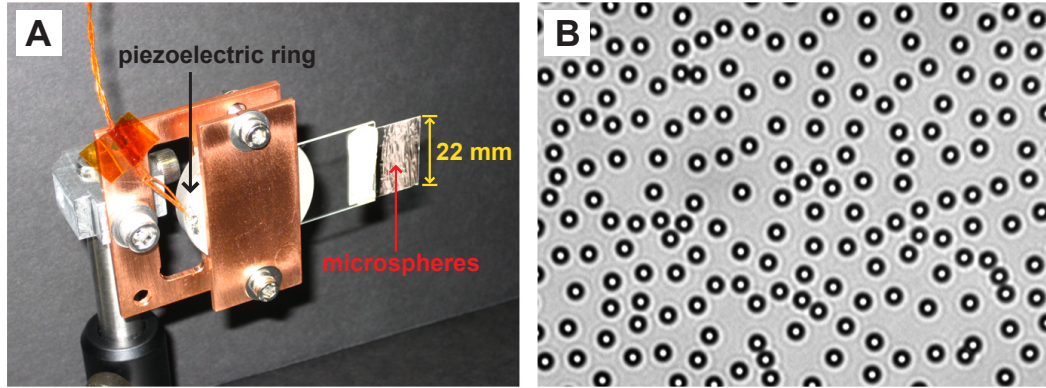
Figure 4.1: (A) A home-built ultrasonic transducer for launching glass microspheres in air, consisting of a piezoelectric ring and a glass microscope slide sandwiched between a pair of copper plates. The microspheres adhere to the coverslip due to van der Waals attraction. (B) 3.0 μm diameter silica microspheres distributed on the surface of the coverslip after ultrasonic vibration, imaged under a microscope with a 40x objective lens.

Microspheres were launched into air from the surface of a glass slide by mechanically vibrating the slide with very high frequency and high amplitude. The vibration was driven by a home-built ultrasonic transducer, which consisted of a piezoelectric ring and a 1 mm thick glass microscope slide sandwiched between two copper plates (Fig. 4.1A). The electrical contacts of the piezoelectric ring were on its two faces, one of which was grounded by the copper plate. The other, isolated by the glass slide, was connected to the drive electronics by a copper wire soldered to its surface. Gluing a much thinner (~0.2 mm thick) No. 2 microscope coverslip to the end of the slide resulted in larger vibration amplitude than that of the thick slide by itself. Dry microspheres were applied to the coverslip in a thin layer.

The piezoelectric ring was driven by a high power square wave at 340
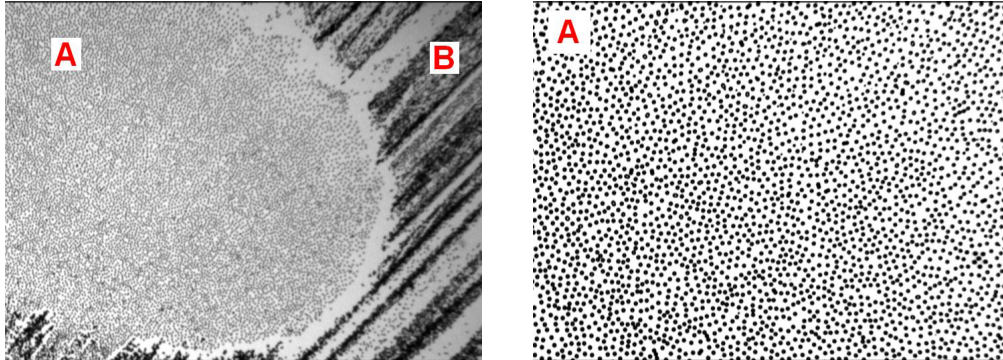
Figure 4.2: Microscope images of 3.0 μ diameter microspheres on the surface of a glass slide. Left: taken using a 4x objective lens. Right: taken using a $10\times$ objective lens, in the region labeled 'A'. Image courtesy of Tongcang Li.

kHz for a short duration of time ($\sim$10 ms). The quantity and size distribution of launched particles depended on the magnitude of the launching RF power, the air pressure, and the number of beads remaining on the slide. At very low power, only loosely bound clumps of particles were launched. When the power is increased, the threshold for the minimum bead size that can be launched decreases. The ultrasonic power for launching 3 μm diameter microspheres is $\sim$4 W, while for beads just half the size, the required power is already $\sim$130 W. The limit to the minimum size of bead which can be launched is 1 μm, a limit determined by the damage threshold of the piezoelectric ring, which was several hundred watts Ref. [60] provides additional information about the launching mechanism and driving electronics.

It is fortuitous that $F_{\text{sphere-sphere}} < F_{\text{sphere-flat}}$: as a result, microspheres separate from one-another before separating from the oscillating glass surface, ensuring that most microspheres are launched as single particles rather than

in 'clumps'. Fig. 4.2 shows microscope images of a glass slide after ultrasonic vibration. The area labeled 'A' was vibrated at sufficiently high amplitude to overcome $F_{\text{sphere-sphere}}$ and the beads are uniformly distributed. The area labeled 'B' did not vibrate at sufficient amplitude and the beads remain stuck together as they were when applied to the slide.

4.2   Trap optics

The trap configuration used to trap microspheres was that of a counter-propagating dual-beam optical trap. A single-beam gradient force trap would have been simpler to implement, but the refractive index mismatch between air and silica is much larger than in water, and much more power is back-scattered by a trapped bead. A single-beam trap would have required a very high NA lens for the gradient force to overcome this scatting force, and high NA lenses for vacuum use are prohibitively expensive, and typically have a very short working distance, which would result in a coating of microspheres on the lens after several rounds of launching. A dual-beam configuration allowed the use of lenses with lower NA and longer working distance than allowed by a single-beam trap, since in the dual-beam configuration, the gradient forces of the two beams add and their scattering forces cancel. A dual beam configuration is also well suited for trapping high refractive index microspheres in water [61]. One disadvantage of a dual beam trap is that misaligned trapping beams result in a much more complicated trapping potential which can have multiple minima, and exert non-conservative forces; doing net work on the trapped

particle [62,63]. For this reason, precise alignment of the two beams is critical.

Figure 4.3 shows a detailed optical schematic of the trapping and detection system used for instantaneous velocity measurement in air. The two trapping beams were generated by an ultra-stable NPRO (non-planar ring oscillator) laser (Lightwave Electronics[1] Model: 126-1063-700). Its rms intensity fluctuations are $< 0.05\%$ between 10 Hz and 2 MHz and shot noise limited above 10 MHz. It emits at a single frequency with a line-width of < 5 KHz/ms and a coherence length > 1000 m (detailed characterization of the properties of NPRO lasers can be found in Ref. [64]). A third, 532 nm wavelength laser beam was used for secondary detection, alignment and illumination. It was generated by a diode-pumped solid-state CW laser (Coherent Inc. model: Verdi V10).

It is important that the two trapping beams do not interfere, since interference at the trap could introduce stationary or dynamic intensity variations at length scales of the laser wavelength and potentially cause perturbation of the equilibrium motion of the trapped particle. One measure taken to avoid this was the use of the two outputs of a polarizing beam-splitter cube to generate orthogonally polarized trapping beams. However, reflection from mirrors and transmission through birefringent media can affect the polarization of the two beams. Another degree of protection from interference was provided by using acousto-optic modulators (AOMs) to control the power in the two beams.

---

[1]Since acquired by JDSU
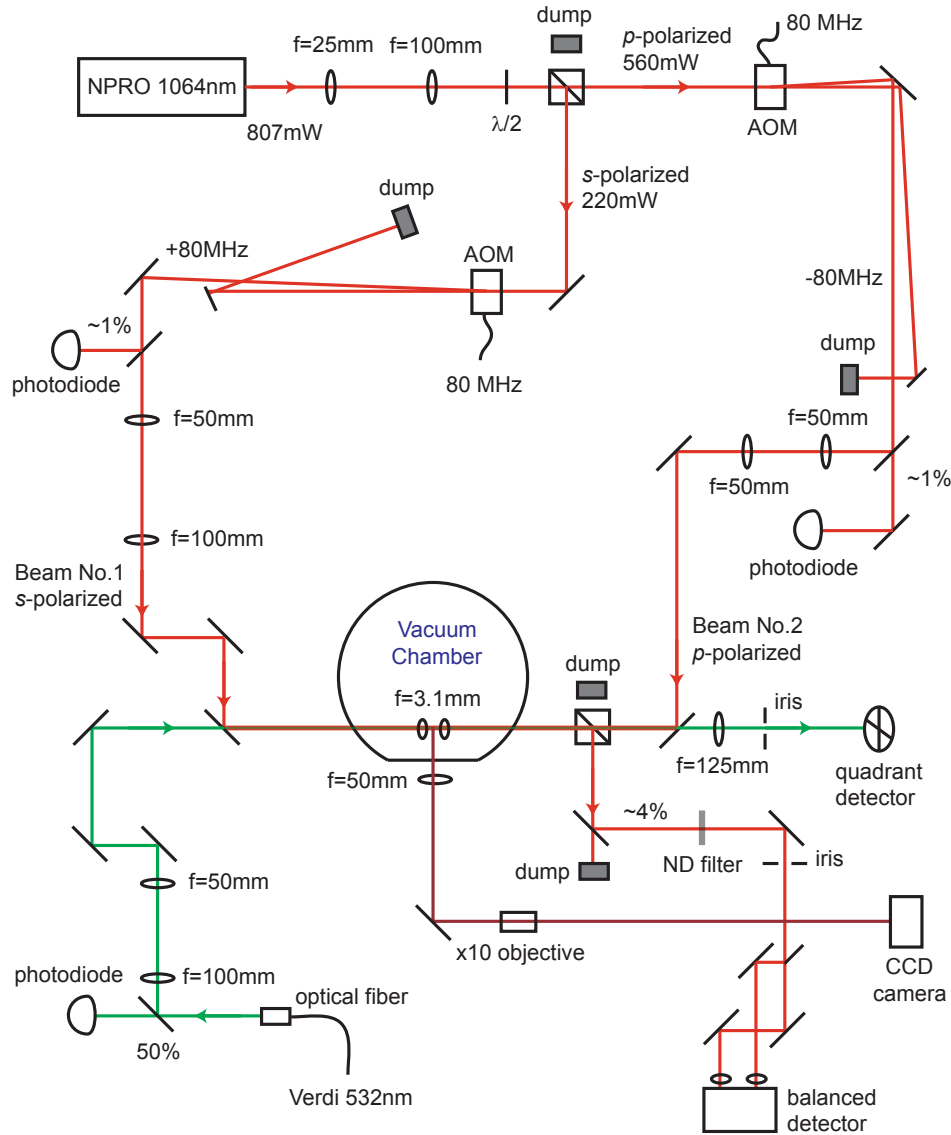
Figure 4.3: Schematic of the optical system for trapping and detection of microspheres in air. The 1064 nm laser is shown in red, and the 532 nm laser is shown in green. Beam No. 1 was used for trapping and detection and enters the trap from the left. Beam No. 2 was used only for trapping and enters the trap from the right. Image courtesy of Tongcang Li.

One beam was the order $+1$ diffraction peak from the AOM while the other was the order -1 diffraction peak. As a result, the frequencies of the beams were shifted in opposite directions, resulting in a total separation of 160 MHz.

The intensity of the three laser beams was controlled using AOMs. Photodiodes were used to monitor the powers of each beam. For each beam, the measured power was used as the error signal for an analog proportional-integral-derivative (PID) circuit whose output was used to control and stabilize each beam's power via the AOMs. The set point for the PID controllers was sent via a digital-to-analog converter (DAC) from the control computer.

The two trapping beams entered the vacuum chamber from either side and were focused by two identical aspheric lenses. After passing through the trapped bead, the beams were re-collimated by the opposite lens, and one of the re-collimated beams was used for high bandwidth back-focal-plane detection. In addition, some of the scattered light was used to perform spatial imaging of the trapping volume. A lens outside the vacuum chamber was used to create an image of the trapped microsphere in front of a $10\times$ microscope objective which magnified that image onto a CCD camera behind it. This diagnostic tool was useful to observe shifts in the axial position of the microsphere within the trap as well as to confirm the presence or absence of a microsphere in the trap.

A top-down view of inside the vacuum chamber is shown in Fig. 4.4. The ultrasonic transducer is mounted vertically, $\sim$5 cm above the optical trap. The two identical aspheric lenses used for trapping had focal length 3.1 mm

60
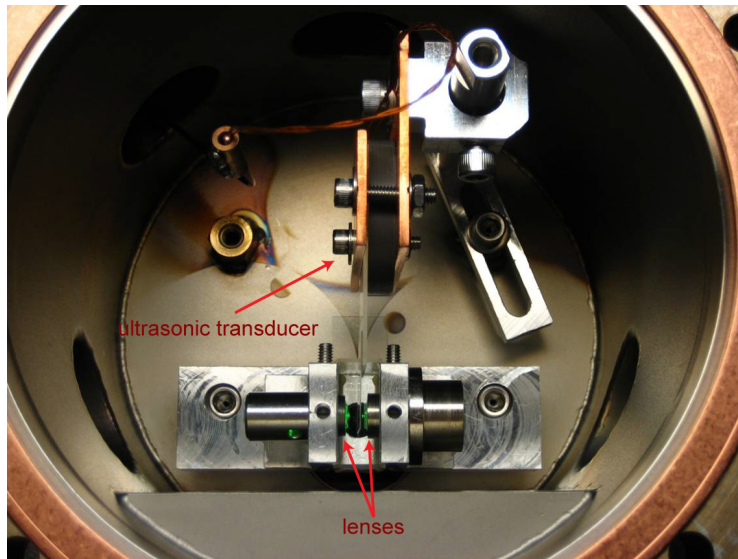
Figure 4.4: Top view inside the vacuum chamber showing the two trapping lenses and the piezoelectric ultrasonic launching transducer. The glass slide from which beads are launched was ∼5 cm above the trap. Image courtesy of Tongcang Li.

and NA of 0.68. The lenses were mounted inside the vacuum chamber, epoxied to steel brackets which were bolted on to an aluminum base. The separation of the lenses was adjusted using a collimated input beam. The separation was set such that after passing through the two lenses, the beam emerged collimated. Such alignment resulted in a separation of ∼3.5 mm between the front surfaces of the lenses. Once the lenses were fixed, the 532 nm beam and second 1064 nm beam were aligned so that they overlapped with the first beam on both sides of the lens pair. Final precise alignment was performed using a pinhole located at the trap focus.

A schematic of the pinhole alignment setup is shown in Fig. 4.5. The pinhole had diameter 1.0±0.5 μm and was mounted on a 3-axis translation stage, controlled by 3 manual differential actuators, as well as a piezoelectric actuator for fine-tuning the vertical displacement. A lens focused the light exiting the pinhole onto a photodiode. First, the pinhole was centered on the focus of beam No. 1 by maximizing transmission. Next, the green beam and beam No. 2 were aligned such that their transmission through the pinhole in the other direction was also maximized. This allowed us to align the foci with an accuracy of about 0.5 μm. When beam No. 2 was being aligned, the lens and photodiode were repositioned to the other side of the trap.

The pinhole was also used to estimate the beam profiles of the two lasers at the focus by measuring transmitted power as the pinhole was scanned across the beam focus. The measured beam profiles were very close to Gaussian, and typical measured beam waists were 2.01 μm in the horizontal direction and 2.12
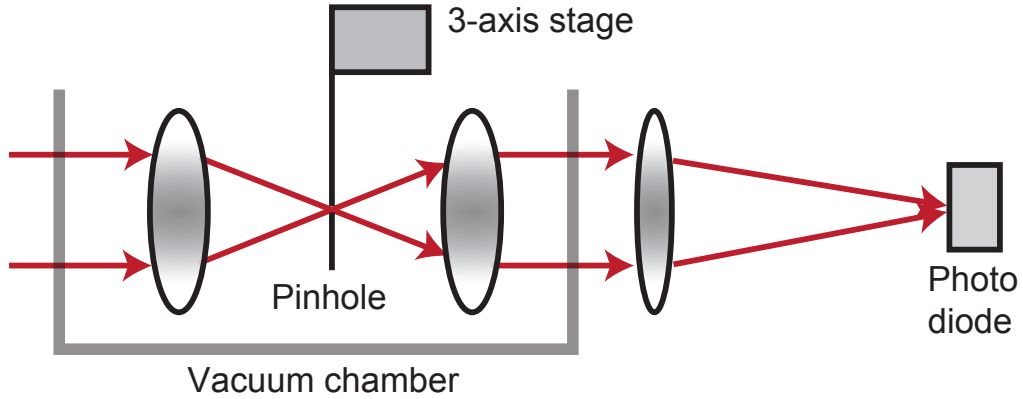
Figure 4.5: Schematic of setup used to measure the beam profile at the waist of the trapping beams. A pinhole was scanned across the waist, and the transmitted power was measured with a photodiode. Image courtesy of Tongcang Li.

μm in the vertical. Waist measurement did not take into account convolution with the finite extent of the pinhole, thus set an upper bound for the actual beam waists. Once the traps were aligned and characterized, the system was ready for launching and trapping of microspheres.

4.3 Trapping procedure

After being launched in air, microspheres fell at terminal velocity under the influence of gravity. Microspheres falling near the trapping region (at the foci of the two lasers) may be trapped as long as there is sufficient damping to reduce the kinetic energy of the particle to be less than the trap depth, ensuring the bead turns around before reaching the edge of the trap. If the air pressure is too low, particles will have too much energy and escape the trap.

However, once already trapped at high pressure, it is possible to reduce the air pressure without losing the bead from the trap.

Typically, microspheres were trapped within 2-3 launching attempts, and successful trapping could typically be achieved within 10 minutes. Once a bead was trapped, it was very stable. The longest observed lifetime of continuous trapping was 46 hours, during which the laser power was significantly varied. In vacuum, the trap was less stable; heating effects from trap misalignment are independent of pressure (if not exacerbated at low pressure due to warping of the chamber caused by the pressure differential) while damping decreases at low pressure, resulting in runaway heating. The lowest pressure at which we trapped a bead without active stabilization was ∼0.1 Pa.

Fig. 4.6 shows a trapped 4.7 μm diameter silica microsphere, made visible to the naked eye by scattering of the 532 nm laser. During acquisition of Brownian trajectories the 532 nm laser was turned off. Trapped beads were also visible on a VCR monitor connected to the CCD camera which imaged the scattered light from the bead, as shown in Fig. 4.7.

When the beam waists at the two foci were of the same size, we found that there was high probability of simultaneous trapping of multiple beads (typically two, though sometimes more). This could have been caused by nonzero separation of the two foci along the optical axis, which would result in a double well potential. The rate at which multiple beads were trapped was reduced significantly by making the waist of one of the beams larger than the other. The left panel of Fig. 4.7, shows the scattered light image of a
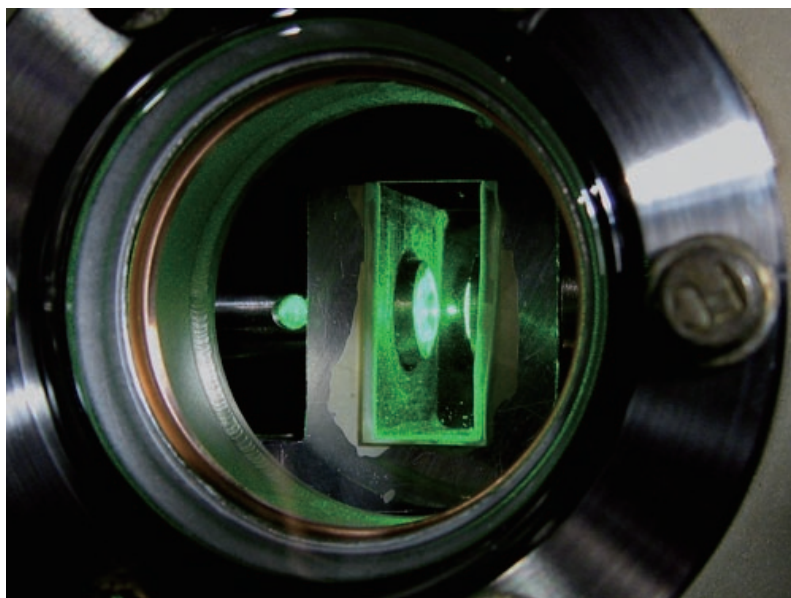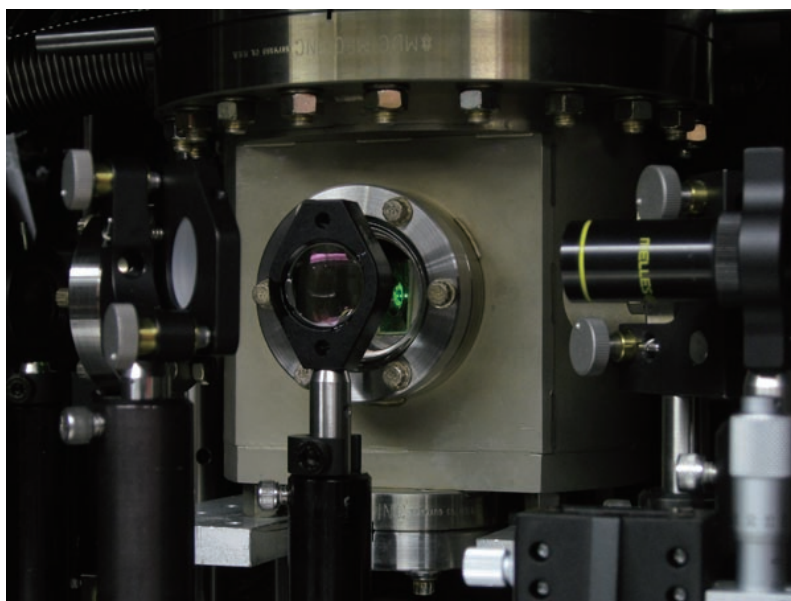
Figure 4.6: Photos of a 4.7 μm diameter silica microsphere trapped by a counter-propagating dual-beam optical tweezer. The trapping beams are outside the visible spectrum, but the bead is visible due to its scattering of a weak 532 nm laser beam used to illuminate the bead. Image courtesy of Tongcang Li.

Figure 4.7: CCD images of trapped beads, formed using scattered light collected from the side of the trap. Left: A single 3.0 μm diameter microsphere; Right: multiple beads in the trap. The air pressure was 752 torr, and the trapping beam powers were 119 mW and 100 mW. Image courtesy of Tongcang Li.

single bead, while the the right corresponds to multiple (2 or 3) beads trapped simultaneously. To ensure that only single beads were trapped at a time, the sizes of the incoming trapping beams were set such that waist of beam No. 1 was twice that of beam No. 2.

4.4   Vacuum system

The trapping chamber and most of the optics were mounted on a 3 ft × 3 ft optical breadboard, itself supported by elastomers on an air-floated optical table. The peak-to-peak vibration amplitude of the lab floor was approximately 30 μm, due to seismic vibrations. For the optical table with floating disabled, the peak-to-peak relative vibration was approximately 0.1 μm. Enabling floating reduced this to approximately 10 nm.

The pressure inside the trapping chamber was controlled using a sorp-

tion pump. A sorption pump consists of a container filled with porous, high-surface-area media. When the pump is cooled with liquid nitrogen, much of the gas in the vacuum system adsorbs to surfaces inside the pump. Once the desired pressure was reached, the pump was closed off by a valve to eliminate the need for continuous cooling. A sorption pump is preferable over mechanical pumps because it has no moving parts and thus introduces no vibration. Since pressure would only be reduced after a bead was in the trap, mechanical vibration of the pump could have perturbed the trapping optics, and thus the trapped bead, enough for the bead to escape from the trap.

The pressure in the trapping chamber was measured using a combination gauge (Kurt J. Lesker Company, model: KJLC 910) with an operating range of 10^{-10} torr to 1500 torr. The gauge uses both a Piezo and a Pirani sensor. The Pirani sensor is gas-type sensitive since it infers pressure by measuring thermal conductivity. The Piezo sensor measures the absolute pressure independent of gas type. The Piezo sensor is used for pressures above 15 torr, the Pirani sensor is used below 5 torr, and the two are used simultaneously between 5 and 15 torr. The accuracy is 1% in the range of 10 - 1000 torr and 10% at pressures below 10 torr.

4.5 Detection system

Fig. 4.8 shows the split-beam detection configuration used in this work. Half of the beam of the beam was reflected by a cut mirror(Thorlabs, model: BBD05-E03) [10], and the two halves were focused onto a balanced detector
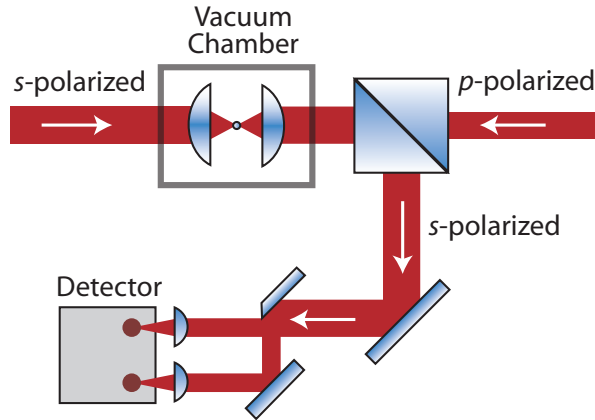
Figure 4.8: Simplified schematic showing the counter-propagating dual-beam optical tweezers, and a novel detection system with 75 MHz bandwidth and ultra-low noise. The s-polarized beam was reflected by a polarizing beam splitter cube after it passed through a trapped bead inside a vacuum chamber. The p-polarized beam passed through the cube. The detection beam was split into two halves with a cut mirror, and the two halves were focused onto the inputs of a balanced photodetector. Motion of the bead causes deflection of the beam. The difference of the two beams' power is proportional to the transverse displacement of the microsphere.

(Thorlabs, model: PDB120C) with 0.3 mm diameter InGaAs photodiodes, sensitive to wavelengths in the range of 800-1700 nm. The detector bandwidth was 75 MHz and transimpedance gain was 1.8×10^5 V/A.

4.6 Digital acquisition system

The high-bandwidth output of the balanced photodetector was digitized using a DAQ card (National Instruments, model: PCI 6133), with maximum sampling rate of 2 Ms/s, maximum sample length of 4 million samples and resolution of 12 bits. A LabVIEW program controlled the acquisition
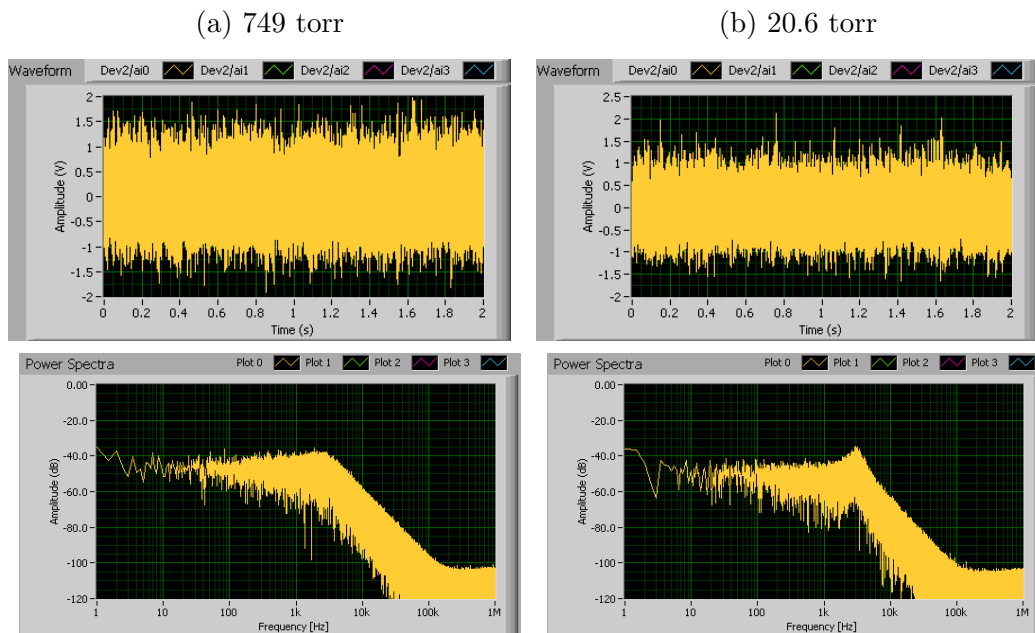
Figure 4.9: Waveforms and position power spectral densities for a 3 μm diameter silica microsphere trapped in air at a)749 torr and b) 20.6 torr. The low pressure position PSD shows the resonant peak that results from a heavily underdamped trap.

card, and was also used to set the operating powers of the lasers and to trigger launching of microspheres. Upon acquisition, the program calculated and displayed the waveform and PSD of the acquired data, examples of which are shown in Fig. 4.9.

Chapter 5

Measurements of Brownian motion in air

For the data presented in this section, unless otherwise stated, the powers of the two laser beams were 10.7 mW and 14.1 mW, the diameter of the bead was (nominally) 3 μm, the temperature of the system was 297 K, and the air pressure was 99.8 kPa or 2.75 kPa. The waists of the two beams (as measured using the pinhole), were 2.2 μm and 3.0 μm. The trapping was stable, and the heating due to laser absorption was negligible under these conditions. For each pressure level, the results were calculated from ten consecutive acquisitions of 4 million points each, acquired in quick succession. The position signal was recorded at the digitizer's maximum sampling rate of 2 Ms/s.

Figure 4.9 shows, for both pressures, the raw position waveforms and power spectral densities (PSDs) corresponding one of the 10 acquisitions generated in real-time by the LabVIEW acquisition program. The waveforms resemble random noise and do not convey much information. The units are in volts, as measured by the digitizer.

5.1   Mean-square displacement

Figure 5.1 shows the MSDs of a 3 μm silica bead as a function of time. For both pressures, the measured MSDs agree with Eq. 1.30 over three decades of time. The calibration factor $\alpha \equiv$ position/voltage of the detection system was the only fitting parameter of Eq. 1.30 for each pressure. τ_p and ω_0 were obtained from the measured normalized $C_v(t)$. The bead mass m_p was calculated from the diameter and density of the microsphere. The two values of α obtained for these two pressures differ by 10.8%. This was caused by distortion of the vacuum chamber at low pressure, which affected the equilibrium position of the bead relative to the detection laser.

The measured MSDs are completely different from those predicted by Einstein's theory of Brownian motion in a diffusive regime. The slopes (on a double logarithmic plot, Fig. 5.1A) of measured MSD curves at short time scales are twice those of the MSD curves of diffusive Brownian motion. This is because the MSD is proportional to t^2 for ballistic Brownian motion, while it is proportional to t for diffusive Brownian motion. In addition, in the short time ballistic regime, the MSD curves, as predicted by $\langle [\Delta x(t)]^2 \rangle = (k_B t/m_p)t^2$, are independent of air pressure. In contrast, the MSD in the diffusive regime does depend on the air pressure. At long time scales, the MSD saturates at a constant value because of the optical trap. Fig. 5.1B displays more detail of the MSD at short time scales.
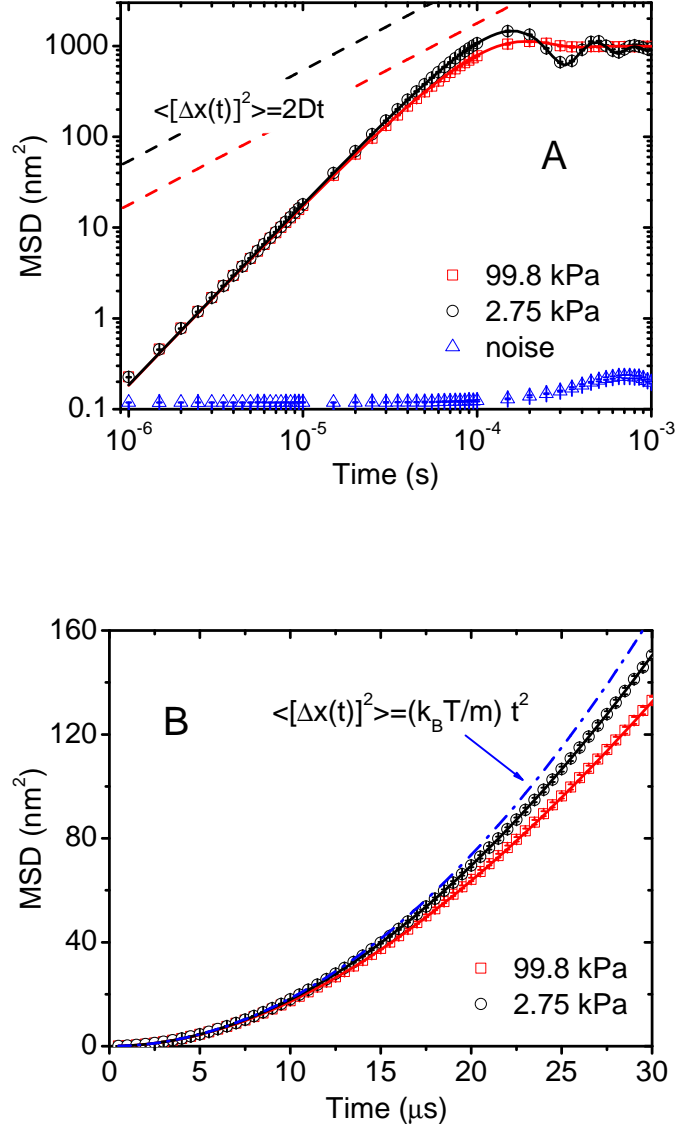
Figure 5.1: (A) The mean square displacements of a 3 μm silica bead trapped in air at 99.8 kPa (red squares) and 2.75 kPa (black circles). They were calculated from 40 million position measurements for each pressure. The "noise" signal (blue triangles) is recorded with no particle in the optical trap. The solid lines are theoretical predictions of Eq. 1.30. The prediction of Einstein's theory of free Brownian motion in the diffusive regime is shown in dashed lines for comparison. (B) MSDs at short time scales shown in detail. The dash-dot line indicates ballistic Brownian motion of a free particle.

5.2 Velocity autocorrelation

Figure 5.2 shows the normalized $C_v(t)$ of the bead at two different pressures. The oscillations were caused by the optical trap, and are particularly pronounced at 2.75 kPa. When normalized by the mean-square velocity $(C_v(0))$, Eq. 1.29 is independent of the calibration factor α of the detection system. The only independent variable is time t, which can be measured with high precision. Thus the normalized $C_v(t)$ provides an accurate method to measure τ_p and ω_0. Fitting of the normalized C_v to Eq. 1.29, resulted in values of $\tau_p = 48.5 \pm 0.1 \mu s$, $\omega_0 = 2\pi \cdot (3064 \pm 4)$ Hz at 99.8 kPa, and $\tau_p = 147.3 \pm 0.1 \mu s$, $\omega_0 = 2\pi \cdot (3168 \pm 0.5)$ Hz at 2.75 kPa. The trapping frequency changed by 3% because the distortion of the vacuum chamber at different pressures resulted in slight changes in the trapping potential. It was also possible to calculate the diameter of the silica bead from the τ_p value at 99.8 kPa [65]. The obtained diameter was 2.79 μm, which is within the uncertainty range given by the supplier. We used this value in the calculation of the theoretical MSD and normalized $C_v(t)$ curves.

For fixed pressure and temperature, τ_p should be independent of the trapping frequency. We verified this by changing the total power of the two laser beams from 25 mW to 220 mW. The measured τ_p changed less than 1.3% for both pressures, confirming the accuracy of our fitting method, and demonstrating that any heating effects due to the laser beams (which would change the viscosity and affect τ_p) were negligible.
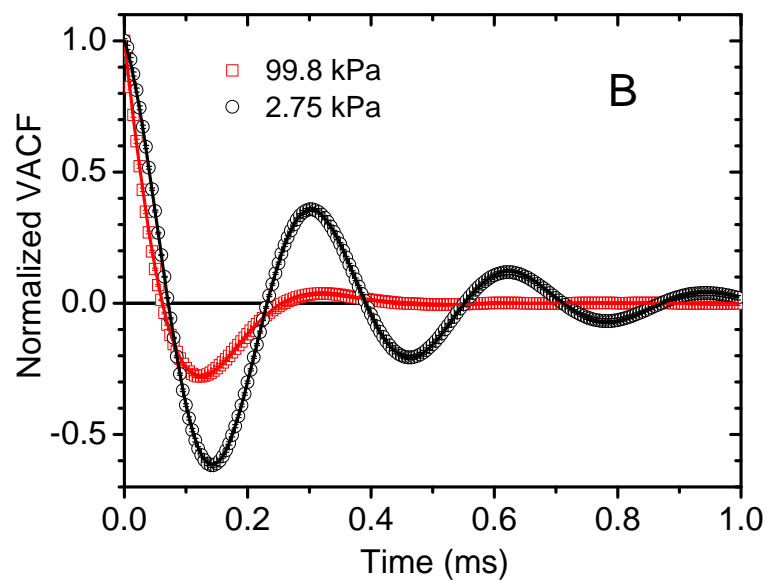
Figure 5.2: The normalized velocity autocorrelation functions for the 3 μm bead at 99.8 kPa (red squares) and 2.75 kPa (black circles). The solid lines show the result of fitting the data to Eq. 1.29

5.3   Power spectral density of position and velocity

Figure 4.9 shows, for both pressures, the raw position waveforms and power spectral densities (PSDs) corresponding one of the 10 acquisitions generated in real-time by the LabVIEW acquisition program. The waveforms resemble random noise and do not convey much information. The units are in volts, as measured by the digitizer. The PSDs (plotted, as is conventional, on a double-logarithmic scale) show the distribution of the signal among different frequency components and reveal physical information that is concealed by the randomness of the waveforms.

Figure 5.3 shows processed PSDs corresponding to the same data as shown in Fig. 4.9. The units were converted from volts to meters using the calibration parameter α determined from fitting the mean square displacement. The physics underlying the signal and noise is much more clearly conveyed in the frequency domain. The trapping parameters can be estimated by comparing Fig. 5.3 to the theoretical prediction of Eq. 3.12, plotted in Fig. 3.5. For the bead trapped at high pressure, location of the 'knee' reveals that the trapping frequency, $\omega_0/2\pi$, is ~ 3 KHz and the slight peak at the corner frequency suggests that the system is slightly underdamped ($\tau_p\omega_0 \approx 1$). At the lower pressure, the system is more underdamped, and a well pronounced peak appears at the trapping frequency. At high frequencies, the magnitude of the PSD is smaller for the bead trapped at low pressure. This is because the thermal force is proportional to the damping strength (in accordance with the fluctuation dissipation theorem) and thus is weaker at low pressure.

Figure 5.3: Position power spectral densities for a 3 μm diameter silica microsphere trapped in air at 749 torr (red squares) and 20.6 torr (black circles) as well as the PSD of the detector noise with an empty trap (blue triangles), scaled to match the magnitude of the high frequency noise floor visible in the position PSDs. At the lower pressure, the resonant peak of the underdamped oscillator becomes more pronounced, while at high frequencies position fluctuations are reduced, due to the weaker thermal force.

The plateau at frequencies above $\sim$100 KHz is due to detection noise, whose PSD dominates that of the bead's motion at high frequencies. To understand the noise of the system, 10 more acquisitions were made with an empty trap: the resulting signal is the combination of vibrational noise in the detection beam and electronic noise from the detector and digitizer. The PSD of the noise signal is also shown in Fig. 5.3, however it was scaled by a factor of 3 prior to plotting so that it overlaps with the high frequency noise floor in the position measurements. The reason that the noise with no bead had a higher magnitude than with a trapped bead is most likely because the power to the detector was different during the acquisition of noise. The magnitude of the contribution of laser pointing noise to the noise floor PSD is proportional to the input power squared. More laser power is transmitted through the trap when there is no bead to cause scattering.

Although the measured MSD and C_v clearly show signatures deep into the ballistic regime, that is not sufficient to confirm the observation of instantaneous velocity. Those functions are averages over a long measurement time. The longer the averaging time, the more the noise in the MSD and C_v is suppressed, because the noise is (typically) uncorrelated. The effect of noise on velocity measurement can be determined by looking in the frequency domain, where the noise spectra are not suppressed but rather added to the signal spectra.

At high frequency, detection noise, which has a flat power spectrum, dominates the position PSD. Directly differentiating this position signal would
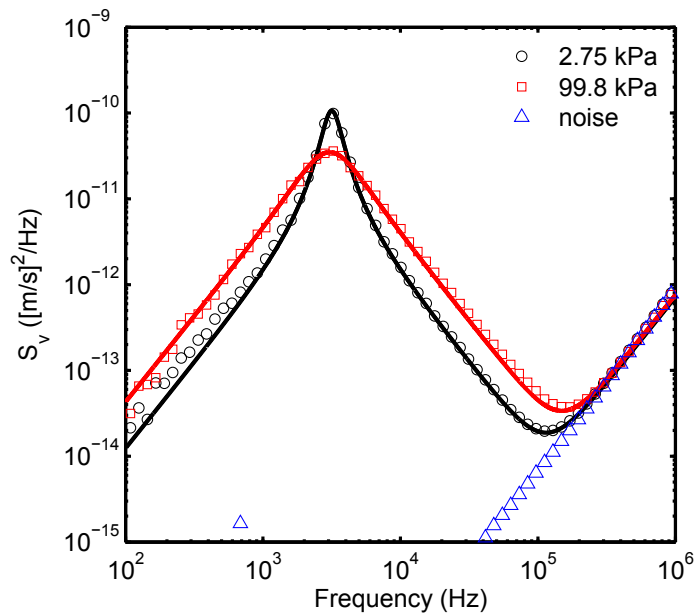
Figure 5.4: Velocity power spectral densities for a 3 μm diameter silica microsphere trapped in air at 749 torr (red squares) and 20.6 torr (black circles) as well as the PSD of the time derivative of detector noise (blue triangles), scaled to match the high frequency noise in the acquisitions with a bead present. The velocity signal is centered on the trap frequency, and has a much narrower distribution at low pressure. When the flat position noise spectrum is differentiated, it results in velocity noise with slope 2 on the log-log plot.

result in a velocity measurement dominated by noise. The velocity PSDs are shown in Fig 5.4. Most of the velocity signal is concentrated at the trap frequency. At low pressure, the motion is more oscillatory, concentrated within a narrower frequency range. The noise curve has a slope of 2. The scale on the log-log plot can be deceptive. Between 100 KHz and 1 MHz, the noise contributes more to the area of the velocity PSD than the velocity signal does between 100 Hz and 100KHz. A more accurate representation can be seen in the cumulative velocity PSDs in Fig 5.5 which reflects how the velocity signal is accumulated when bandwidth is increased. For both pressures the CS_V approaches the the same asymptotic value: the thermal mean square velocity, which depends only on particle mass, however at low pressure, this value is reached at lower frequencies, because more of the signal is concentrated at the trap frequency. The noise contribution grows as bandwidth to the third power, but only begins to dominate the signal at frequencies where the signal is already close to its asymptotic value, meaning that, with correct choice of bandwidth for low-pass filtering, an accurate measurement of instantaneous velocity can be recovered.

5.4 Instantaneous velocity measurement

Noise was reduced by averaging every 10 successive position measurements and differentiating the averaged position, resulting in instantaneous velocity measurements with time resolution of 5 μs. Although averaging reduced the temporal resolution by a factor of 10, it greatly increased the signal-to-noise
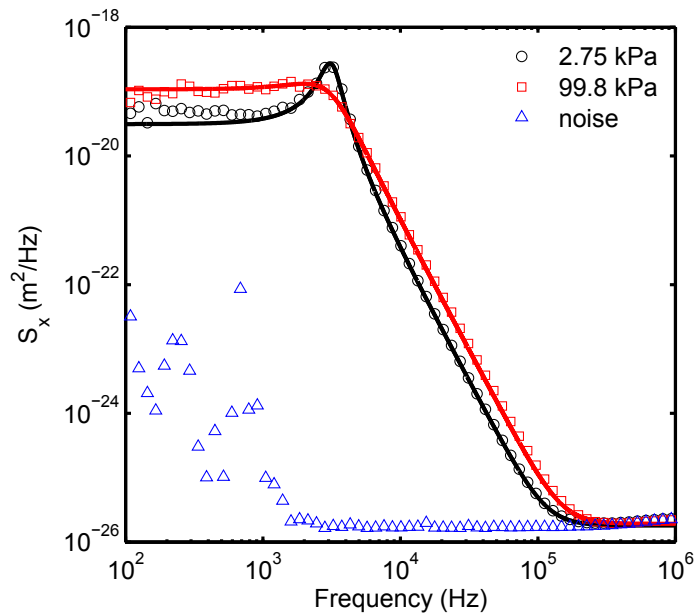
79
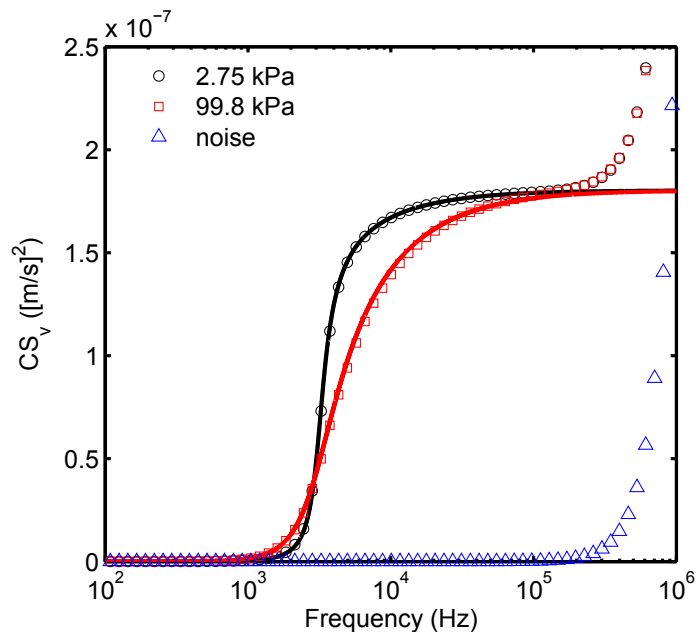
Figure 5.5: Cumulative velocity power spectral densities for a 3 μm diameter silica microsphere trapped in air at 749 torr (red squares) and 20.6 torr (black circles) and for no bead (blue triangles). At both pressures the CS_V approaches the thermal mean square velocity, which is independent of pressure. The noise contribution grows as bandwidth to the third power.

ratio of the measured velocity. As discussed in section 2.3, the averaged velocity is close to the instantaneous velocity as long as $CS_v(\omega)$ at $\omega = 1/(2\pi\tau_{av})$ is in its flat, plateau region. For this data, $\tau_p = 48$ μs at 99.8 kPa and $\tau_p = 147$ μs at 2.75 kPa.

Figure 5.6 shows 2 ms long snapshots of position and velocity traces from the recorded trajectories. The position traces of the bead at the two different pressures appear very similar to one another. On the other hand, the velocity traces are clearly different. The instantaneous velocity of the bead at 99.8 kPa fluctuates more rapidly than that at 2.75 kPa, because the momentum relaxation time is shorter at higher pressure.

The distributions of the measured instantaneous velocities (Fig. 5.7) are in agreement with the Maxwell-Boltzmann distribution (Eq. 3.19). The measured rms velocities were $v_{rms} = 0.422$ mm/s at 99.8 kPa and $v_{rms} = 0.425$ mm/s at 2.75 kPa. These are very close to the prediction of the energy equipartition theorem, $v_{rms} = \sqrt{k_B T / m_p}$, which is 0.429 mm/s. As expected, the velocity distribution was independent of pressure. The rms value of the (unscaled) noise signal was 0.021 mm/s, corresponding to 1.0 Å spatial resolution in 5 μs. This measurement noise was about 4.8% of the rms velocity, corresponding to an SNR[1] of 26 dB. Fig. 5.7 represents direct verification of the Maxwell-Boltzmann distribution of velocities and the equipartition theorem of energy for Brownian motion.

---

[1]SNR defined as $10\log\left(\langle v^2_{\text{signal}}\rangle/\langle v^2_{\text{noise}}\rangle\right)$
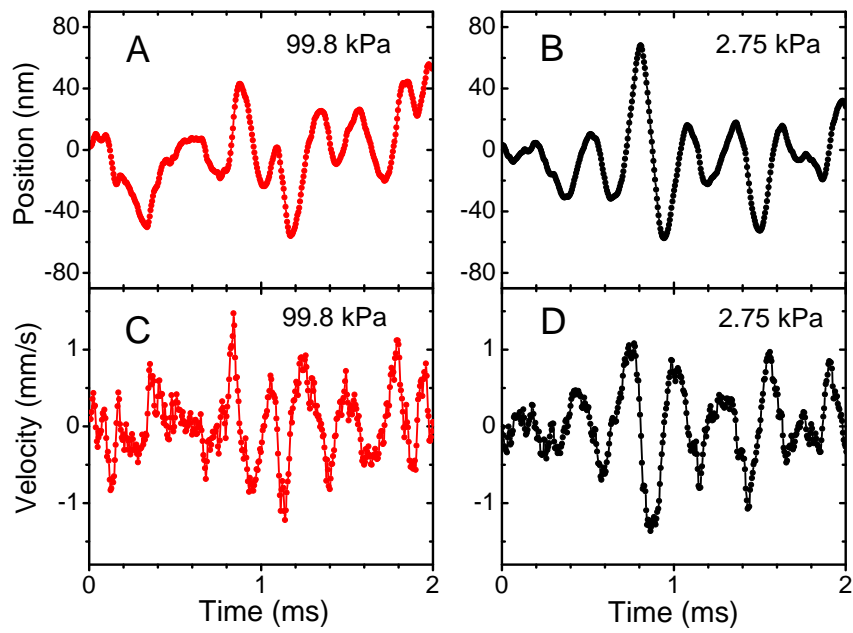
Figure 5.6: One-dimensional trajectories of a 3 μm diameter silica bead trapped in air at 99.8 kPa (A) and 2.75 kPa (B). The instantaneous velocities of the bead corresponding to these trajectories are shown in (C) and (D).
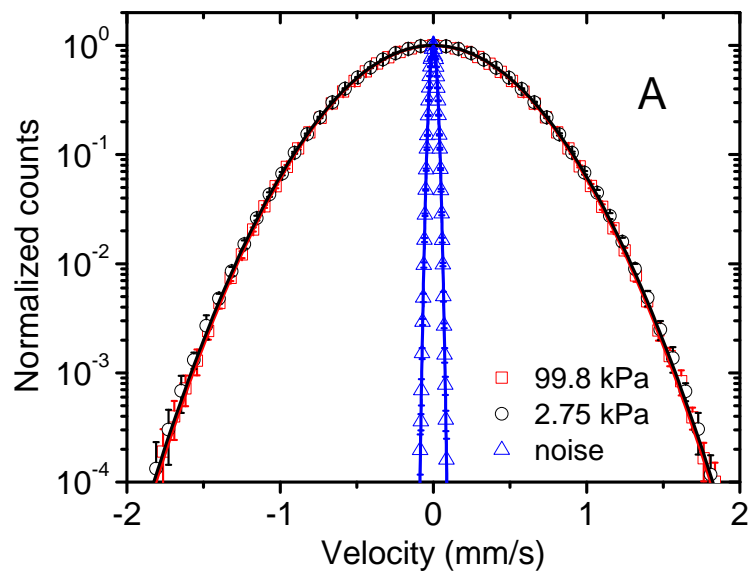
Figure 5.7: The distribution of the measured instantaneous velocities of a 3 μm silica bead. The statistics at each pressure are calculated from 4 million instantaneous velocities. The solid lines are Maxwell-Boltzmann distributions. We obtained $v_{rms} = 0.422$ mm/s at 99.8 kPa (red squares) and $v_{rms} = 0.425$ mm/s at 2.75 kPa (black circles) from the measurements. The rms value of the noise (blue triangles) is 0.021 mm/s.

5.5 Outlook

The ability to measure the instantaneous velocity of a Brownian particle will be invaluable in studying non-equilibrium statistical mechanics [66, 67] and can be used to cool Brownian motion by applying a feedback force in a direction opposite to the velocity [68, 69]. In vacuum, our optically trapped particle promises to be an ideal system for investigating quantum effects in a mechanical system [70–73], due to its near-perfect isolation from the thermal environment. Combining feedback cooling and cavity cooling, we expect to cool the Brownian motion of a bead starting from room temperature to the quantum regime, as predicted by recent theoretical calculations [72, 73]. We have directly verified the energy equipartition theorem of Brownian motion. However, we also expect to observe deviation from this theorem when the bead is cooled to the quantum regime. The kinetic energy of the bead will not approach zero even at 0 K because of its zero-point energy. The rotational energy of the bead should also become quantized.

Chapter 6

Brownian motion with memory

The results of Ch. 3 were derived assuming that the damping force on a sphere moving at velocity v relative to the surrounding fluid is given by Stokes law: $F_{\text{Stokes}} = -\gamma_s v$. However, when a bead changes speed in a dense, viscous liquid, it triggers a dynamic, gradual change in the flow around the bead, and this flow affects the force on the bead at future times. The force at any instant depends on the history of the bead's motion, not just the bead's velocity at that instant. This is referred to as the memory effect. This effect was in fact understood by Sir George Stokes: the same paper which contains Stokes law also gives the frequency dependent damping on an oscillating sphere in liquid. [74]. Both the amplitude and the phase of the damping force has frequency dependence. The memory effect exists in air as well, but in air the time scales of Brownian motion and the memory effect are distinctly separated.

For microspheres in liquids, $\tau_p \approx \tau_f$. When two dynamic processes occur at similar time scales, the coupled behavior becomes much more complicated than the uncoupled behavior. In this case, the fluid flow resulting from the bead's Brownian motion 'sloshes around' at similar time scales as the bead, the fluctuations become much more erratic, as sometimes the slosh-

ing adds constructively, and some times it cancels out. This situation raises the possibility for deviation from equipartition; there is strong correlation between the bead's motion and the fluid's force on the bead which may lead to a non-Gaussian distribution for the force.

6.1   Fluid dynamics: forces on a moving sphere

Although fluid dynamics can be notoriously nonlinear, in the case of Brownian motion the Reynolds number is $\ll 1$ and the linearized approximation of fluid dynamics is accurate. Linearity means that a solution for arbitrary motion can be written in as a sum of solutions for oscillatory motion at many different frequencies.

This section will present the full expressions for hydrodynamic interaction between a sphere with arbitrary velocity submerged in fluid, followed by a brief discussion of the nature of that force.

The interaction between the fluid and a sphere can be isolated by considering the force necessary to maintain oscillation of a mass-less spherical shell with velocity $v(t) = \text{Re}(v_0 e^{i\omega t})$. The damping can be described by $\gamma[\omega]$, with $F_{fr}(t) = \text{Re}(v_0 \gamma[\omega] e^{i\omega t})$. The solution requires solving for the fluid flow around the bead and integrating the viscous and normal forces over the sphere's surface. The result gives $\gamma[\omega]$:

$$\gamma[\omega] = \gamma_s(1 + \sqrt{-i\omega\tau_f}) - \frac{i\omega m_f}{2} \tag{6.1}$$

where

$$m_f \equiv \frac{4\pi r^3 \rho_f}{3} = m_p \frac{\rho_f}{\rho_p} \tag{6.2}$$

is the mass of the fluid displaced by the bead, and

$$\tau_f \equiv \frac{r^2 \rho_f}{\eta} = \tau_p \frac{9}{2} \frac{\rho_f}{\rho_p} \tag{6.3}$$

is a characteristic timescale of the fluid flow around the bead, which shall be explained below.

The expression for the friction force at time t_0, exerted on a sphere arbitrary velocity $v(t)$ defined in the interval $-\infty < t < t_0$, can be found by inverse Fourier[1] transformation of equation 6.1. The result is [75]:

$$F_{fr}(t_0) = -\gamma_s \left[v(t_0) + \sqrt{\frac{\tau_f}{\pi}} \int_{-\infty}^{t_0} \frac{\dot{v}(t)}{\sqrt{t_0 - t}} dt \right] - \frac{m_f}{2} \dot{v}(t_0) \tag{6.4}$$

Equations 6.1 and 6.4 each have three terms, which correspond to different aspects of the fluid flow generated by the bead. Figure 6.1 illustrates flow around the bead in different regimes in which the three effects are isolated.

6.1.1 Dissipative forces

The first term is of Eq. 6.4 identical to Stokes damping. It is the only non-vanishing term for motion at constant velocity in a fluid with zero density. The corresponding flow field for this situation is shown in Fig. 6.1B. Roughly speaking, the net damping force is determined by integrating, over the bead's

---

[1]Technically it is calculated using inverse Laplace transformation, which are more convenient with causal-like boundary conditions
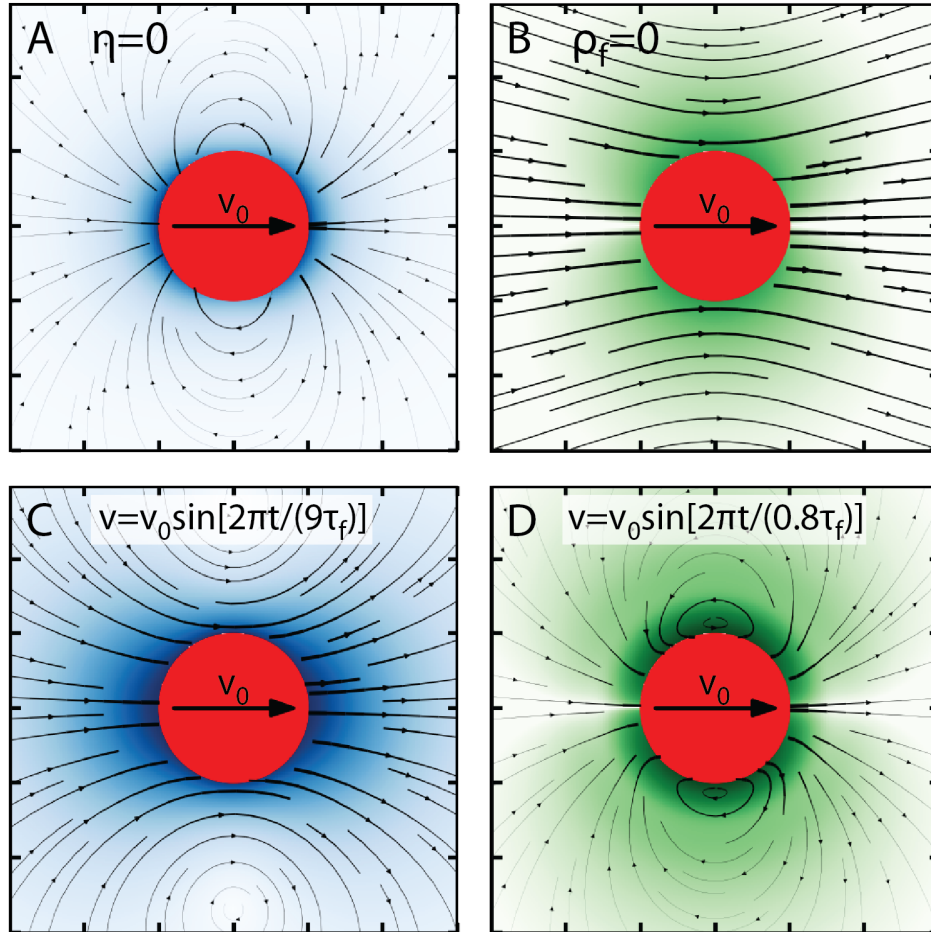
Figure 6.1: Theoretical flow fields for different regimes of fluid flow around a sphere, each case shows the fluid flow in an instant when the bead is moving to the right with velocity v_0. The 'camera' is stationary and the bead is moving past it. Blue shading represents fluid velocity magnitude on a linear scale, while green shading represents the component of shear stress which contributes to damping. (A) Potential flow of an inviscid fluid, resulting in only the effective mass force. (B) Flow of a hypothetical fluid with viscosity but no density, (equivalently, flow in a dense, viscous fluid in which the particle has been moving at constant velocity) resulting in Stokes damping. (C) and (D), Full hydrodynamic flow around an oscillating particle, with oscillation period 9 τ_f and 0.8 τ_f, respectively.

surface, the component of the stress tensor parallel to the surface. In Figs. 6.1B and D, the green shading indicates the magnitude of the relevant component of the stress tensor corresponding to the fluid flow indicated.

The second term of Eq. 6.4 does not lend itself to straightforward interpretation in neither the time nor the frequency domain. It is known as the Basset force [75–77]. It arises due to vorticity that originates at the surface of an accelerating particle and diffuses outward, expanding to the size of the bead in time τ_f. The strength of the Basset force is proportional to $\sqrt{\eta \rho_f}$. As the density approaches zero, the vorticity diffuses away too quickly to affect the motion of the sphere. When the viscosity approaches zero, the interaction strength between the bead and the vorticity approaches zero.

In Equation 6.1, the Basset force can be split into its real and imaginary components:

$$\gamma[\omega] = \gamma_s(1 + \sqrt{\frac{\omega \tau_f}{2}}) - \frac{i\omega m_f}{2}(1 + 9\sqrt{\frac{1}{2\omega \tau_f}}) \qquad (6.5)$$

The real part acts in phase with the velocity and represents the damping-like, dissipative component of the force. The imaginary part acts out-of-phase with the velocity and can be thought of as an inertia-like, conservative component of the thermal force. The strength of the in-phase component relative to that of Stokes damping is negligible at low ω and increases at high frequencies. For $\omega > 2/\tau_f$, the dissipative component of the Basset force is stronger than Stokes damping.

An example of the fluid flow responsible for the increase in damping

89

is illustrated in Fig. 6.1D, which should be compared to Fig. 6.1B. Fig. 6.1D shows the fluid field around a sphere oscillating at $\omega \approx 8\tau_f$, at the instant of maximum velocity. The fluctuation of the sphere's direction creates a toroidal vortex around the equator of the sphere: the fluid nearest the surface moves in the same direction of the sphere, while fluid further away moves in the opposite direction of an earlier phase of the sphere's oscillation. Vorticity in a fluid obeys a diffusion equation. Its spread driven by the viscous force between adjacent layers of water moving different speeds. Over time viscosity tends to reduce velocity gradients and localized information diffuses outwards. The spatial extent of the vortex generated by the oscillating bead depends on the oscillation frequency. When the frequency is high, the vortex is close to the surface and creates more shear in the velocity at the surface than in the case of a sphere moving at constant velocity and thus a stronger damping force.

6.1.2 Conservative forces

The third term of Eq. 6.4 results in what is known as the added mass. In a dense fluid, the gravitational mass of an object is modified due to pressure from the fluid it displaces. Similarly, an objects inertial mass must be modified to account for the inertia the displaced fluid, and this effect is contained in the third term in equations 6.1 and 6.4. The effective particle mass is thus $m^* = m_p + m_a$. Where, for a sphere in an unbounded fluid, the added (inertial) mass of the displaced fluid is $m_a = m_f/2$ [78]. It is the only force experienced by a sphere accelerating in an inviscid, incompressible fluid, and can be derived

90

using the approximation of potential flow [79].

Figure 6.1A illustrates the fluid flow around a moving sphere for a fluid with zero viscosity but nonzero density. The only non-vanishing force term in this case is effective mass term. The magnitude of the fluid flow velocity is indicated in blue. Assuming the fluid is incompressible, the illustrated flow instantaneously tracks the velocity of the bead, thus a force on the sphere must accelerate the mass of the shaded volume of fluid as well as the mass of sphere. The flow field extends to infinity, but most of the contribution comes from the fluid near the bead.

The imaginary component of the Basset force in Eq. 6.5 is in some ways comparable to the effective mass term. The relative strength of the imaginary, inertial component of the effective mass is negligible at high frequencies but increases for low frequencies, contributing more than the added mass for $\omega < 40/\tau_f$. Fig. 6.1C shows the velocity of the flow field around a sphere oscillating at a frequency of $\omega \approx 0.7\tau_f$. The momentum of the fluid flow at the instant of maximum velocity is shaded in blue. This fluid flow does not instantaneously follow changes in the bead's velocity, but some of it contributes to the bead's apparent inertia.

When $\omega \to 0$, the contribution of the Basset force to the inertial mass goes to infinity. This corresponds to the entrainment of an infinitely large volume of fluid that occurs after motion at constant velocity for an infinitely long time. The resulting force itself is not infinite, but can be nonzero even when the velocity and acceleration of the sphere is zero.

6.1.3 An example in the time domain

The behavior of the Basset force can be illustrated in the time domain by considering the force necessary to maintain constant velocity for an initially stationary sphere accelerated by an impulse at $t = 0$. Immediately after the impulse, the fluid at the surface of the sphere has the same velocity as the sphere, but fluid slightly further is stationary, resulting in a very strong velocity shear and thus strong damping force. Over time, this shear at the surface relaxes as information about the velocity change diffuses in the direction perpendicular to the sphere's propagation, transitioning from a flow like that of Fig. 6.1D to one more like that of Fig. 6.1C. By the time that $t \approx \tau_f$, the spatial extent of the vorticity expands to a volume of fluid comparable to the size of the bead. The fluid around the bead is temporarily entrained and the shear at its surface, and thus the damping force, undershoots that of the steady state Stokes damping. Eventually the vorticity expands to infinity and the flow field approaches to the case of Fig. 6.1B.

6.2 Effect on Brownian motion

To include the effects of hydrodynamic interaction, the term $\gamma_s v$ the Langevin equation of Eq. 3.4 must be replaced with the friction force of Eq. 6.4:

$$m_p \ddot{x}(t) = -Kx - \left[\frac{m_f}{2} \ddot{x}(t) + \gamma_s \left(\dot{x}(t) + \sqrt{\frac{\tau_f}{\pi}} \int_{-\infty}^{t} \frac{\ddot{x}(t')dt'}{\sqrt{t - t'}} \right) \right] + F_{th}(t) + F_{ext}(t),$$

$$(6.6)$$

Moreover, the corresponding thermal force fluctuations can no longer be

described as delta-correlated. The thermal force is less a series of independent kicks and more the result of fluctuating fluid flows that persist over time. The same kind of vorticity that is generated by damping a sphere's motion can spontaneously form and decay due to thermal fluctuations in the fluid. Thus, for consistency with equilibrium, the thermal force has non-white spectrum and non-delta autocorrelation:

$$S_{F_{th}}(\omega) = 2\gamma_s k_B T (1 + \sqrt{\omega \tau_f / 2}), \tag{6.7}$$

$$C_{F_{th}}(t) = 2\gamma_s k_B T \left[\delta(t) - \frac{1}{2} \sqrt{\frac{\tau_f}{\pi}} t^{-3/2} \right]. \tag{6.8}$$

The resulting theoretical predictions for hydrodynamic Brownian motion are given in Section 1.2. To illustrate the differences between Brownian motion in air and liquid, this section will compare three different sets of results for a 3 μm diameter silica microsphere (density ρ_p=2×10³ kg/m³), in a harmonic trap with trap constant K=10^{-6} N/m. The first is the prediction of EOU theory for the microsphere in air. The second is the prediction of EOU theory using the viscosity of water and the effective mass of the microsphere in water ($\eta = 1.00$ mPa·s, $\rho_f = 1 \times 10^3$ Kg/m³): it ignores the Basset force term. The third uses the results of the complete hydrodynamic theory of Section 1.2.

Also included in the comparison is the effect of white-spectrum position shot noise with an amplitude $\sqrt{S_{x_n}} = 20$ fm/$\sqrt{\text{Hz}}$, assuming detection power and optical gain are identical for the three systems (in reality, the optical gain would probably be less in water due to the smaller relative refractive index).

6.2.1 Position PSD

Figure 6.2 shows the the predictions of S_x for the three systems. The noise is shown as a red dashed line. Interestingly, the noise overpowers the Brownian motion in air at a lower frequency than it does the two predictions for water. At low frequencies, the EOU theory and hydrodynamic theory converge. At intermediate frequencies, the hydrodynamic theory begins to dip below the EOU theory. This is caused by the inertial component of $\gamma[\omega]$ in the denominator of Eq. 1.48. At high frequencies, the hydrodynamic theory has higher amplitude than EOU theory. This is a result of the $\mathrm{Re}(\gamma[\omega])$ term in the force spectrum in the numerator of Eq. 1.48; the increasing magnitude of the colored thermal force at high frequencies. In the limit of large ω, the EOU S_x decays (on the log-log plot) with a slope of -4, while the colored term in the force causes the hydrodynamic S_x to decay with a shallower slope of -3.5.

6.2.2 Velocity PSD

Figure 6.3 shows the corresponding predictions for S_v, in which the difference between the three is somewhat more pronounced. The flat shot noise in the position spectrum results in 'pink' noise in the velocity spectrum, with slope 2 when drawn on a log-log plot. The velocity of the particle in air has a much more narrow distribution among frequency components, centered around ω_0. At high ω the hydrodynamic velocity PSD decays with slope -1.5 while the EOU prediction decays with slope -2. Equipartition requires the area of both curves be equal to $k_B T/m^*$. The larger amplitude of the

Figure 6.2: Comparison of position PSDs predicted by EOU in air (dash-dot line), EOU in water (dotted line) and the full hydrodynamic theory in water (solid line). Also shown is the shot noise spectrum corresponding to a position sensitivity of 20 fm/$\sqrt{\text{Hz}}$. Higher viscosity results in much larger amplitude at low frequency and at high frequencies. Addition of the Basset force term results in slightly suppressed amplitude below $\sim 2\pi \times 10^7$ Hz due to the imaginary part of the damping in the denominator. Above $\sim 2\pi \times 10^7$ Hz the real part of the damping in the numerator, the color in the thermal force, results in more fluctuation at high frequencies than EOU theory predicts.

hydrodynamic S_v at high frequencies is compensated by its smaller amplitude at intermediate frequencies. This is related to the nature of the Basset force - at long time scales it increases the inertial mass of the bead and suppresses the amplitude of fluctuations. As a trade-off, more energy is taken away from the bead's motion at short time scales, resulting in stronger damping and a stronger thermal force.

6.2.3 Mean-square displacement

The three MSD curves are shown on a log-log plot in Fig. 6.4. The difference between the EOU and hydrodynamic theories for water are very minimal here. The MSD for the bead trapped in air approaches the asymptotic value of $\langle x^2 \rangle = k_B T / K$ more quickly than the beads in water. In the ballistic regime, the MSD of the bead in air is $\sim 25\%$ higher due to its lighter bare mass.

6.2.4 Velocity autocorrelation

The theoretical predictions for velocity autocorrelation are shown in Fig. 6.5. Here the difference between the three systems stands out much more clearly.

The effective mass term results in an important implication for Brownian motion in liquid. Hydrodynamic theory predicts $C_v(0) = k_B T / m^*$ where the effective mass m^* is the sum of the mass of the particle and half the mass of the displaced fluid [78]. Thus the predicted velocity of the particle will be
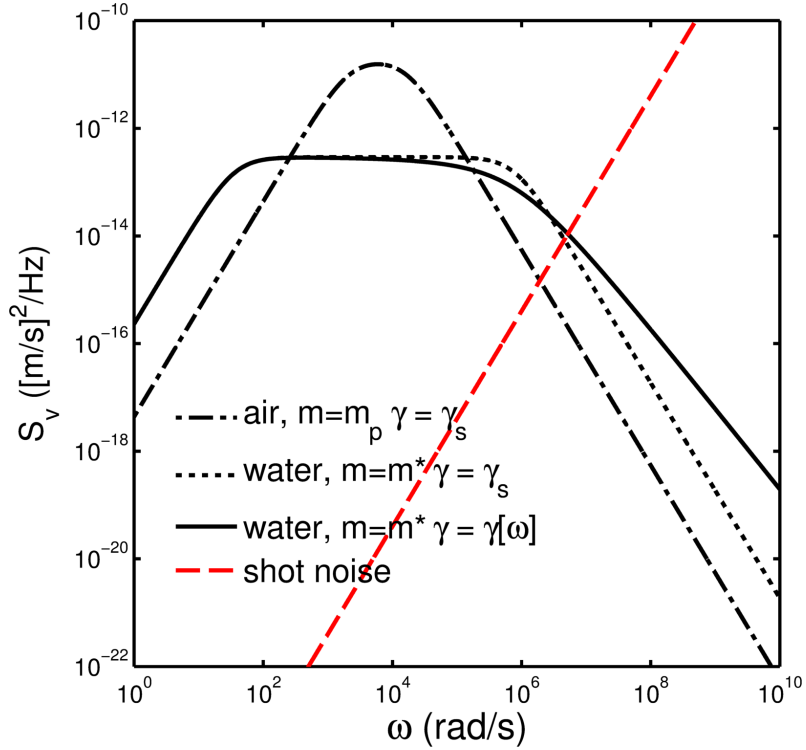
Figure 6.3: Comparison of velocity PSDs predicted by EOU in air (dash-dot line), EOU in water (dotted line) and the full hydrodynamic theory in water (solid line). Also shown is the shot noise spectrum corresponding to a position sensitivity of 20 fm/$\sqrt{\text{Hz}}$, which in the velocity spectrum results in 'pink' noise with slope 2. The velocity of the bead in air is distributed over a much narrower frequency range. The hydrodynamic S_v gives velocity with slightly broader distribution than that of the EOU theory.
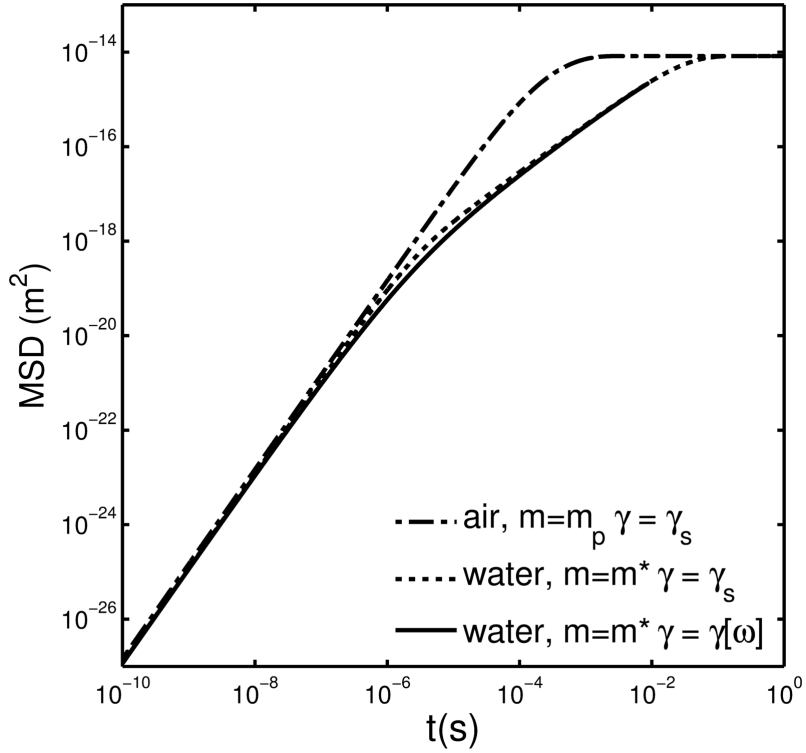
Figure 6.4: Comparison of MSDs predicted by EOU in air (dash-dot line), EOU in water(dotted line) and the full hydrodynamic theory in water (solid line). The biggest difference is the slower approach to the plateau of the two systems with higher damping. All three curves approach the same asymptotic value of $\langle x^2 \rangle = k_B T / K$. The effective mass of the beads in water is 25% heavier than the bare mass of the bead in air, thus the magnitude of the MSD in the Ballistic regime is correspondingly smaller. However on a log scale, such a difference is barely noticeable.

$v^*_{rms} = \sqrt{k_B T / m^*}$ in the ballistic regime, in contradiction to the prediction of the equipartition theorem. The apparent contradiction is resolved when the finite compressibility of the fluid is taken into account. In a compressible fluid, information about the particles velocity takes time to propagate through the fluid. The effects of compressibility become significant at timescales shorter than $\tau_c = r/c$, where c is the speed of sound in the fluid [78]. In order to measure the true instantaneous velocity in liquid as predicted by the equipartition theorem, the temporal resolution must be much shorter than τ_c.

In the case of the microspheres in Ch. 8, for the barium titanate microsphere in acetone (c=1180 m/s), $\tau_c \approx 2$ ns, while for the silica microsphere in water (c=1480 m/s), $\tau_c \approx 1$ ns. In both cases these timescales are far shorter than those at which we observe Brownian motion. The effects of compressibility are well separated from the regime of coupled hydrodynamic Brownian motion. If compressibility were taken into account, theory predicts that velocity autocorrelation begins to rise around τ_c and plateaus at the mean square velocity of the bare mass, corresponding to decoupling between the motion of the bead from the fluid envelope around it.

The bead in air has slight anticorrelation due to a small amount of resonance allowed by the lower damping. The C_v predicted by EOU approach a plateau much more rapidly than the hydrodynamic theory.
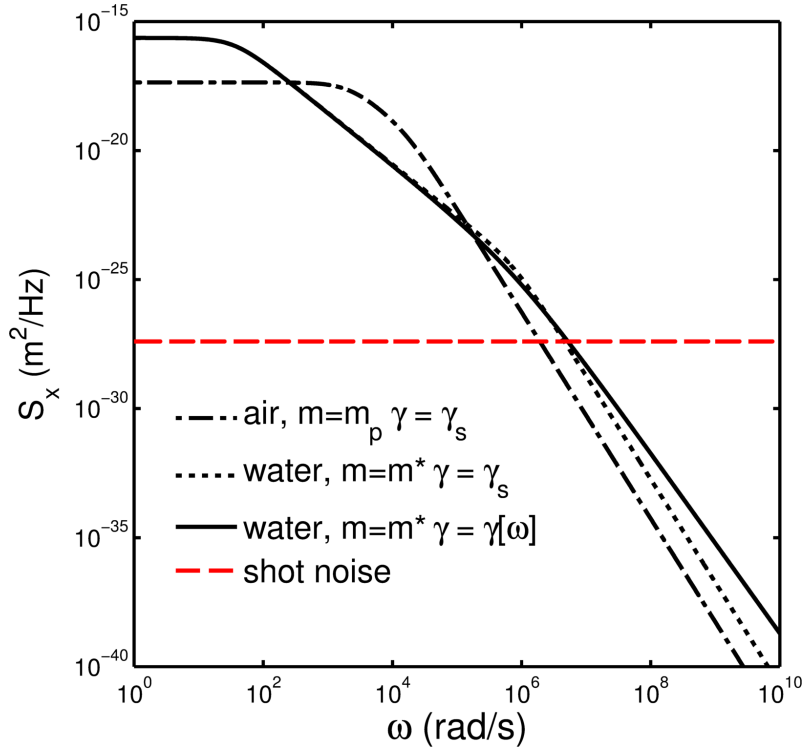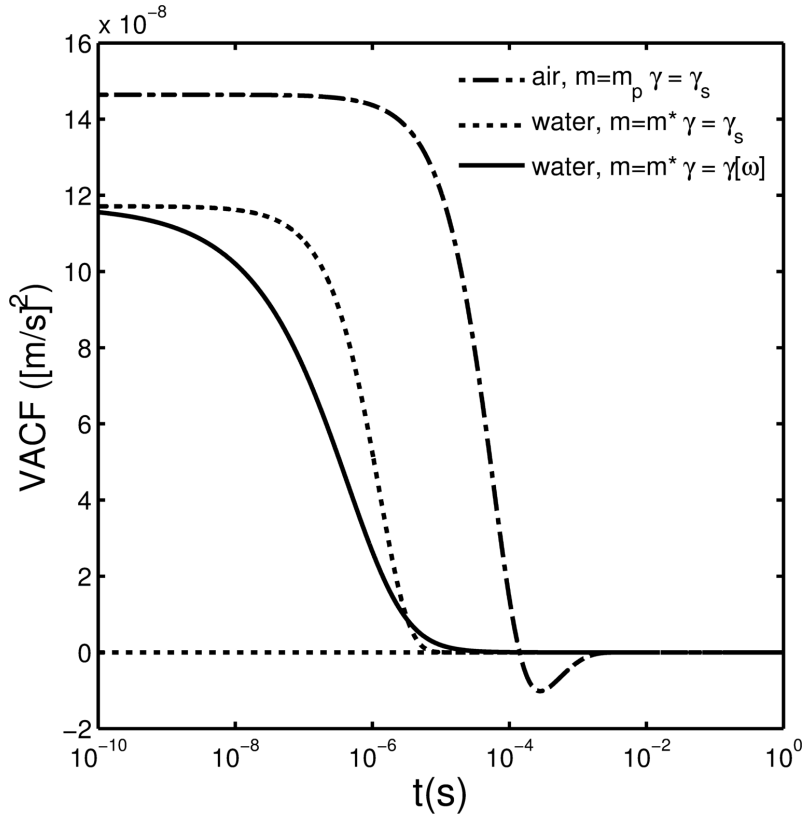
Figure 6.5: Comparison of velocity PSDs predicted by EOU in air (dash-dot line), EOU in water(dotted line) and the full hydrodynamic theory in water (solid line). Velocity correlation is proportional to the second derivative of the MSD, but there is much more variation between the prediction for the velocity autocorrelation of the three systems compared to that of the MSD (the linear scale on the vertical axis helps accentuate the difference). The beads in water have a smaller equilibrium velocity than the bead in air due to the effective mass. The EOU C_v have a much flatter plateau region than the hydrodynamic prediction.

6.2.5 Implications for velocity measurement

The cumulative velocity PSDs are shown in Fig. 6.6, along with CS_{v_n}, the variance of noise in the measured velocity. Qualitatively, the CS_v curves are closely related to the velocity autocorrelation curves in Fig. 6.5, except shown in the frequency domain rather than the time domain. However, from the CS_v curves it is possible to directly estimate the effect of low pass filtering on the signal and the noise, which is not as obvious from the velocity autocorrelation curves, in which there is no straightforward way to even quantify noise. The cumulative velocity PSD of the noise has ω^3 dependence, acting as an almost vertical wall concealing the signal above a certain frequency. The three cumulative velocity spectra approach their asymptotic value ($\langle v^2 \rangle$) at very different rates.

To better compare the effect of measurement bandwidth on signal and noise, Fig. 6.7, shows the quantity $\delta^{-2} \equiv 1 - CS_v/\langle v^2 \rangle$, on a log-log scale. δ can be loosely identified as the signal-to-noise ratio for instantaneous velocity measurement, caused either by additive noise or by distortion from low-pass filtering.

The contribution from the noise is $\delta_{\text{noise}}^{-2} = S_{x_n}\omega_b^3/(6\pi\langle v^2 \rangle)$. The full expressions for CS_v for Brownian motion are rather complicated but they obey simple power laws at high frequency: $\delta_{\text{EOU}}^{-2}(\omega_b) = (2\pi\omega_b\tau_p)^{-1}$ for the EOU theory and $\delta_{\text{hydro}}^2(\omega_b) = (8\tau_v\omega_b/\pi)^{-1/2}$. The difference in the power laws comes from the $\sqrt{\omega}$ in the numerator of the hydrodynamic PSD.
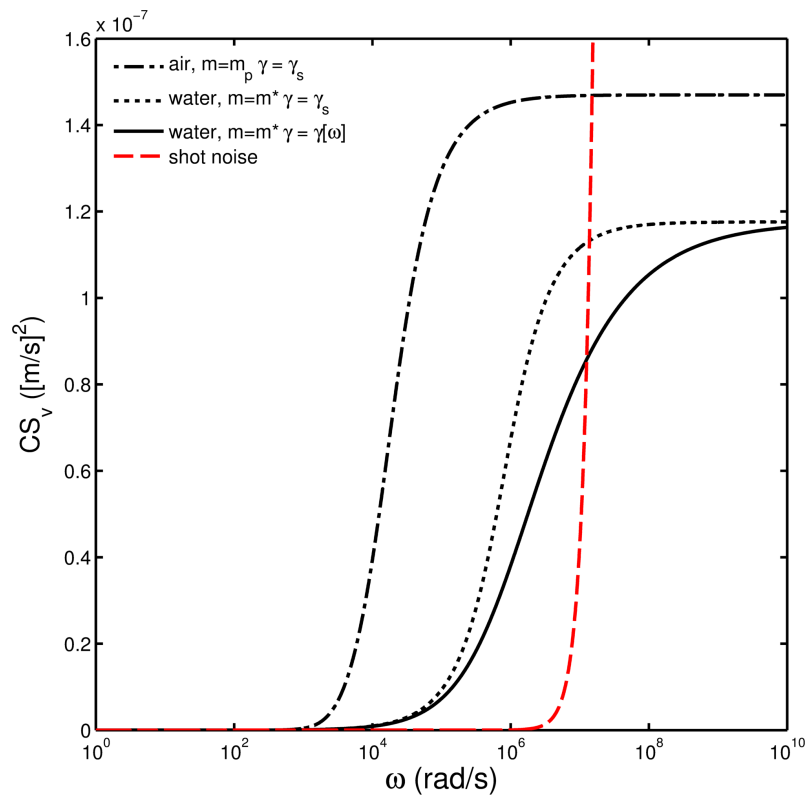
Figure 6.6: Comparison of cumulative velocity PSD
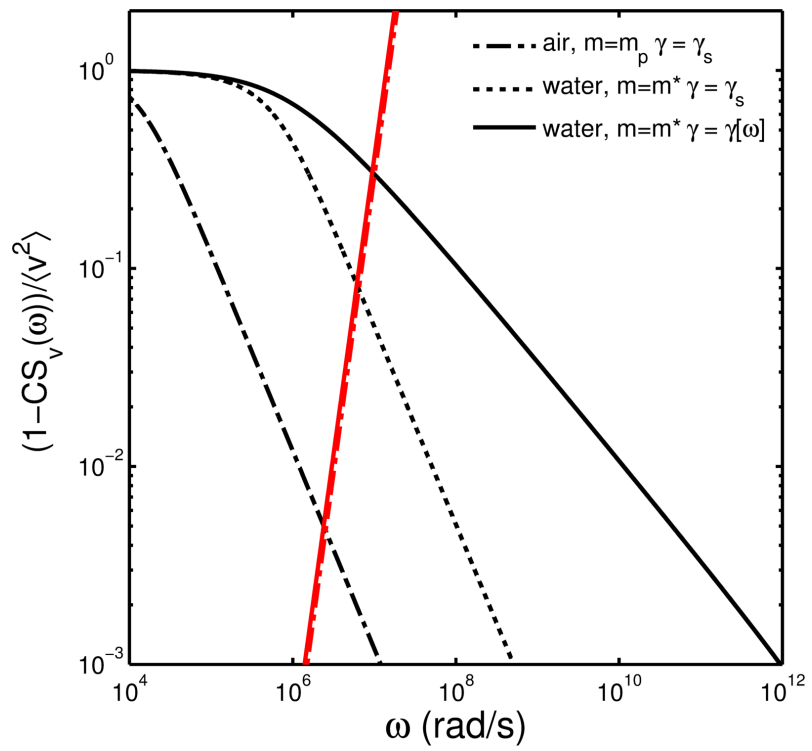
Figure 6.7: Power law dependence of 1-CS_v and the contribution of noise.

The contribution from noise increases with increasing bandwidth, while the contribution from the filter decreases with increasing bandwidth. One possible choice for a tradeoff is to choose ω_b such that the effects of noise and of low pass filtering are of equal magnitude, ie. $CS_{v_n}(\omega_b) = \langle v^2 \rangle - CS_v(\omega_b) = \langle v^2 \rangle / \delta^2$. In Fig. 6.7, this corresponds to the point where the black curve intersects with the red curve. The frequency at which they intersect, ω_m, determines the necessary measurement bandwidth, while the vertical coordinate, δ_m^2 gives a measure of the signal-to-noise that will be achieved. EOU theory predicts:

$$\omega_m = \left(\frac{1}{2\pi\tau_p} \frac{6\pi}{S_{x_n}} \frac{k_B T}{m_p} \right)^{1/4} \tag{6.9}$$

and

$$\delta_m^2 = (2\pi\tau_p)^{3/4} \left(\frac{6\pi}{S_{x_n}} \frac{k_B T}{m_p} \right)^{1/4} \tag{6.10}$$

While hydrodynamic theory predicts:

$$\omega_m = \left(\frac{\pi}{8\tau_v} \right)^{1/7} \left(\frac{6\pi}{S_{x_n}} \frac{k_B T}{m^*} \right)^{2/7} \tag{6.11}$$

and

$$\delta_m^2 = \left(\frac{8\tau_v}{\pi} \right)^{3/7} \left(\frac{6\pi}{S_{x_n}} \frac{k_B T}{m^*} \right)^{1/7} \tag{6.12}$$

Figure 6.7 most clearly presents the difficulty of measuring velocity in liquid compared to measurement in air. For the position sensitivity of 20 fm/$\sqrt{\text{Hz}}$ measurement in air has $\delta > 10$; the variance of the noise is less than $1/100$ that of the velocity, while the variance in the measured velocity is at least 99% that of the instantaneous velocity, the average relative uncertainty for measured velocity is $1/10$.

104

With the same position sensitivity, velocity measurement in water has $\delta \sim 1.7$. The variance of the noise is $1/3$ that of the instantaneous velocity, and the measured velocity is only 66% of the instantaneous. Not only is water more difficult to begin with, but marginal improvements are also more difficult. In air, doubling SNR requires twice as high a bandwidth and 2^4 better sensitivity. In water, doubling SNR requires a four-fold increase in bandwidth and 2^7 times better sensitivity. Velocity measurement in water with $\delta = 10$ requires a reduction of S_x by 12 orders of magnitude, or a position sensitivity of 20 am/$\sqrt{\text{Hz}}$.

6.3 Improving SNR of velocity measurement in liquid

While it may not be possible to measure the velocity for a silica bead in water, it is possible to choose different materials for the bead and the liquid which give better velocity SNR for a given position noise. We can rewrite Eq. 6.12 in terms of material properties:

$$\delta_m^2 \propto \left(\frac{k_B T}{S_{x_n}} \frac{r^3(\rho_p + \rho_f/2)^5}{\eta^3 \rho_f^3} \right)^{1/7} \tag{6.13}$$

$$\omega_m \propto \left(\frac{k_B T}{S_{x_n}} \right)^{2/7} \left(\frac{\eta \rho_f}{r^8(\rho_p + \rho_f/2)^5} \right)^{1/7} \tag{6.14}$$

The strongest dependence is on bead density, (which should be maximized). The fluid density and fluid viscosity should be minimized. It appears that increasing bead diameter also increases δ, but complete description requires the consideration of the dependence of optical gain on bead diameter,

which is discussed in Chapter 2.

The ideal bead material for measuring the velocity of Brownian motion is barium titanate glass. It is available in highly spherical microspheres, which have been previously used for whispering gallery mode resonators [80] and superresolution [81], both of which take advantage of its exceptionally high index of refraction (2.1). The high index of refraction is expected to offer improvement in the optical gain for position detection, lowering S_x. Of even more benefit to velocity measurement is its high density 4.2 g/cm^3, more than double that of silica.

Acetone has similar optical properties to water, but has lower density (0.785 g/cm^3 vs. 0.998 g/cm^3) and lower viscosity (0.322 mPa·s vs. 1002 mPa·s). The combined effect of barium titanate and acetone, compared to silica and water, assuming the same bead size and position sensitivity, gives a factor of improvement for δ^2 of 2.8. It also results in a slight decrease in the necessary detection bandwidth, by a factor of 1.7.

In the air experiment, the detection noise was not optimized. If care is taken to reduce external sources of noise, detection is limited by photon shot noise, which depends on the detected laser power P. The effective position noise scales as $S_{x_n} \propto P^{-1}$. We developed a detection system in which the detected power was increased by a factor of 20 compared to the air experiment, which wasn't even shot noise limited to begin with. This gives another factor of 1.5 increase in δ^2.

Due to the complex dependence of optical gain on bead diameter, the location of the bead within the trap, and the NA of the trapping beam, it is difficult to estimate the dependence of δ on particle diameter. This optimization was performed by trial-and-error.

With the combined improvements of optimized bead and fluid materials, high power detection system, and particle diameter, we expected that, while it might not be possible to measure velocity with as high SNR as was done in air, we could expect measurement with δ^2 of at least 12.

Chapter 7

Trapping and detection of microspheres in water and acetone

As discussed in the previous chapter, the key ingredients of high SNR measurement of Brownian velocity in liquid are high optical gain, high detection power, low density fluid, and high density microspheres. The setup of our experiment to measure velocity was designed with these elements in mind. The trap geometry and flow cell system were designed to allow trapping of beads with high terminal velocity, and to be compatible with reactive, low viscosity fluids such as acetone. Water-immersion lenses were used for diffraction-limited focusing and detection. The biggest single contribution to successful velocity measurement was the use of barium titanate glass microspheres, which have exceptionally high density and very high refractive index, acting to improve both the signal and the detection.

A simplified schematic of the trapping and detection configuration is shown in Fig. 7.1. A counter-propagating dual-beam trap configuration, the same as that used in the air experiment, was also chosen for trapping and measuring particles in liquid. The primary reason was that the high refractive index barium titanate microspheres necessary for velocity measurement results
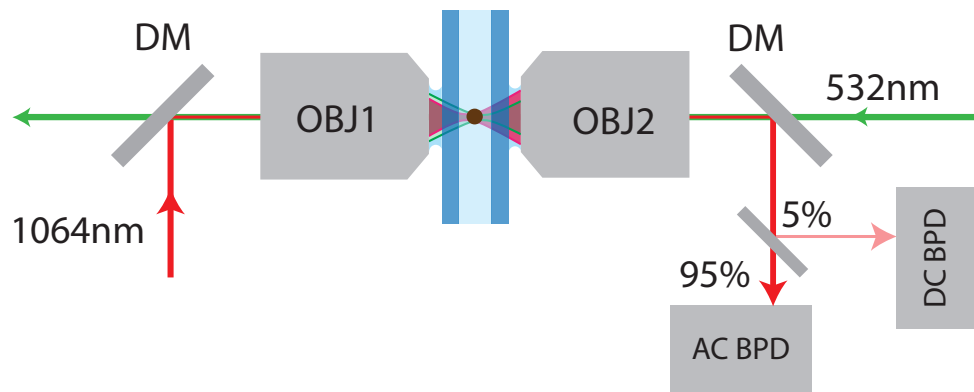
Figure 7.1: A simplified schematic of the optical trap and position detection system. A microsphere is trapped by counter-propagating 1064 nm (shown in red) and 532 nm (shown in green) laser beams, focused by identical microscope objectives (OBJ). The 1064 nm laser is then used to detect the horizontal motion of the bead. It is split between a low power DC balanced photodetector (DC BPD) and a high power, AC coupled balanced photodetector (AC BPD) (DM: dichroic mirror).

in a strong scattering force, rendering single-beam trapping unstable. Again, like in the air experiment, the optical trap used for trapping in water was designed to have a horizontal optical axis, such that the flow cell was mounted vertically. This provided several advantages over the more common design of a horizontal sample chamber and vertical optical axis. It reduced the likelihood of dirt collecting on the inside surfaces of the flow cell which could distort the trapping and detection beams. Also, barium titanate microspheres in acetone have such a high terminal velocity ($\sim$10 μm/s), that in a horizontal chamber, they would collect on the bottom surface within seconds, far from the trapping plane. This configuration also allowed for the laser beams to remain in a single horizontal plane close to the optical table, which made adjustment of optics easier. Reduction of the vibration amplitude of optical components was also easier because all of the optical elements could be mounted close to the surface of the optical table. The experiment was conducted on the same air-floated optical table as that used for trapping in air.

An additional advantage of the dual beam configuration was that it allowed for more flexibility in optimizing the optical gain, whose magnitude has nontrivial dependence on the relative position between the trapped bead and the detection laser as well as the numerical aperture of the detection laser. It was possible to adjust the relative position between the bead by either adjusting the position of the trapping lenses or by changing the power and geometry of the trapping beams. The presence of the counter-propagating beam made it possible to use a low NA detection beam, and to move the bead

relative to the detection beam without affecting the detection optics.

7.1 Flow-cell trapping chamber

Preliminary experiments were performed using 'disposable' sample chambers, which were filled with bead solution and then sealed. Such a design posed several problems. In a horizontal sealed chamber, once the particles settle on the bottom of the chamber, trapping requires translation of the chamber so that the trap is near the wall of the chamber. This was not possible with the narrow clearance of our objectives, which have a short working distance.

The situation was improved by constructing a microfluidic flow cell, closely based on a design from the Minitweezers project [82]. An illustration of the chamber, mounting and plumbing connections is shown in Fig. 7.2. Beads and fluid were introduced into the chamber via a syringe, thus the chamber could be reused, and the flow through the chamber could be controlled to optimize conditions for trapping. Although such chambers were more difficult to construct than those the more common sealed design, the flow cells did not need to be replaced as often, since new particles can be re-introduced whenever trapping is desired. Once a particle is trapped, pure solution can be gently flowed through the cell to clear out any stray microspheres or other contaminants liable to enter the trap over time and affect the Brownian motion signal.

The maximum allowable (outer) thickness of the complete flow cell was limited by the combined working distance of the two objectives, which was
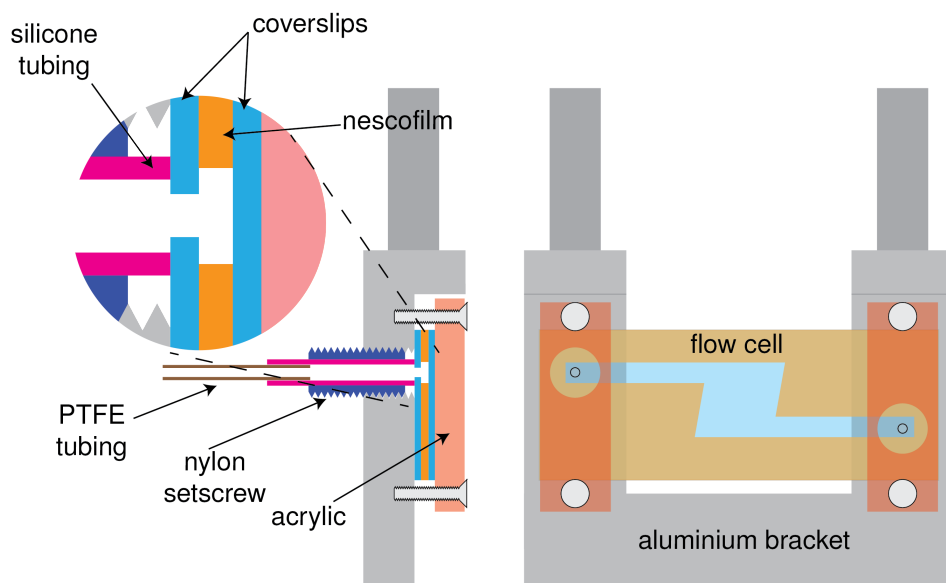
Figure 7.2: Schematic of the flow cell shape with cliff, mounting geometry, and fluid connections.

roughly 300 μm. If the inner chamber of flow cell is too narrow, boundary effects become non-negligible: if the trapped bead is too close to the chamber wall, the presence of the boundary affects statistics of Brownian motion. A rule of thumb is that the bead-wall distance should be 10 times the bead diameter [83].

The flow cell was constructed using a layer of Nescofilm (Bando Chemical Ind. LTD., thickness ~80 μm) sandwiched between two 24 mm × 60 mm No. 0 microscope coverslips (Gold Seal model: 24X60-0-002) with thickness ~100 μm. Nescofilm was used rather than the Parafilm used in reference [82] due to its resistance to acetone and slightly smaller thickness (80 μm)[1].

The input and output ports to the flow cell were made by drilling ~1 mm diameter holes were drilled into each side of one of the coverslips (prior to assembly). The holes were made by drilling into a stack of coverslips using a diamond drill bit at very high speed on a CNC milling machine. A scalpel was used to cut the shape of the flow cell into the Nescofilm. The inside of the Nescofilm formed the inner walls of the flow cell, creating a sealed volume between the two drilled holes. The typical shape was similar to that in Fig 7.2. 1 mm wide entry and exit channels, aligned with the holes in the coverslip, connected the inputs of the flow cell to a larger, ~3 mm × 3 mm trapping chamber at its center.

The flow cell was assembled by sandwiching the Nescofilm between two

---

[1]As of July 2014 Nescofilm is no longer available from distributors in the United States.

microscope coverslips. One with holes and one without. A pressure-resistant seal between the glass and Nescofilm was made by heating the sandwich under pressure. The sandwich was placed on a lab hotplate, at around 155° C for about 4-5 minutes, with an aluminium weight on top of it to apply pressure. The sandwich was mounted to an aluminium bracket using acrylic plates. The aluminium bracket had threaded holes aligned with the drilled holes in the coverslip. Silicone tubing was inserted inside a drilled nylon setscrew. When the set screw was screwed into the aluminium bracket, the tubing was pressed onto the coverslip and a pressure seal formed around the drilled hole. PTFE tubing was used to connect the needle of a syringe to the nylon tubing. The outside of the PTFE tubing was pressed into the inside of the silicone tubing and held by friction.

The flow cell and bracket were suspended between the two objectives by a 3-axis translation stage. The mounting geometry was such that the bracket could be removed and installed without the need to remove the closely-spaced trapping objectives. The translation stage provided adjustment of the location of the optical trap within the trapping chamber.

Microspheres are shipped from the supplier in the form of a dry powder. Trapping in liquid requires a solution of microspheres with minimal concentration. The solution was prepared by adding a small quantity of the powder to a vial of high purity water or acetone. Uniform mixing was achieved by immersing the vial in the bath of an ultrasonic cleaner. Ultrasonic agitation was sufficiently strong to separate and disperse the microspheres. The solution

was then transferred from the vial to a 1 cc syringe. The syringe was mounted in a syringe pump suspended above the flow cell. The syringe pump allowed introduction of the solution into the microchamber at a precisely controlled flow rate. Hand-pumping of the syringe introduced the risk of breaking the seal of the flow cell by applying too much pressure. The exit port of the flow cell was connected to a waste collection vial mounted on the optical table below the flow cell.

Barium titanate microspheres were more difficult to trap than silica particles. Particularly in acetone, in which they have a very high terminal velocity, the microspheres sank to the bottom of the flow cell very rapidly. The Nescofilm edge of the bottom of the flow cell distorted one or both of the trapping beams enough that it was not possible to pick up a sunken bead. The only way to trap barium titanate beads in acetone was to 'catch' them while they were sinking to the bottom. For this reason the Nescofilm chamber was designed with the shape shown in Fig. 7.2: the input channel connected to the trapping chamber at the top, and the output channel connected at the bottom. By activating the syringe pump, microspheres would skirt along the bottom of the input channel until they reached the trapping chamber, where they would fall from the 'cliff' below the edge of the input channel. The cliff was under-cut at an angle so that falling beads fell away from the chamber wall, and could be 'caught' in a region with no Nescofilm in the way. Once a particle was trapped, the flow cell was translated to move the trap away from the cliff area to reduce the chance that stray particles would interfere with the

trap.

7.2 Trap lenses

Although they are not explicitly designed to focus lasers, microscope objectives are often chosen for optical trapping, because the optics of diffraction-limited imaging is closely related to that of diffraction-limited focusing of a laser beam. However microscope objectives also include features to correct for chromatic aberration, coma and flat imaging plane, which do not improve diffraction-limited laser focusing along the optical axis but increase the complexity of the lens and number of optical elements, usually at the cost of reduced transmission. The transmission at 1064 nm can be particularly low since imaging lenses are typically designed for the visible spectrum. On the other hand, the fundamental design criteria for high-end microscope objectives overlap with the requirements of a lens used for optical trapping: high NA and diffraction-limited imaging.

The most common microscope objective lenses that are designed for high NA, diffraction-limited imaging, are based on what is known as an 'oil immersion' design. Optimal imaging for such a lens occurs when there is no variation in refractive index between the image plane and the sample. This is achieved by imaging the part of the sample in contact with the plane of the coverslip. Refractive-index-matching oil is applied in the gap between the last lens of the objective and the coverslip. Using such a lens to image at some depth beyond the coverslip rapidly degrades its performance due to aberration

116

introduced by the addition of the coverslip - sample medium (usually water) interface. Likewise, using an oil immersion lens to focus a laser at some depth beyond the coverslip will result in a non-Gaussian beam focus, whose properties depend on the distance between the focus and the coverslip, even for distances as short as tens of μm.

Water immersion microscope objectives are designed for imaging in water some depth below the cover slip. Rather than matching the coverslip index, water (or index matching oil with the same refractive index as water) is used between the objective and the coverslip to match the index of the medium. This reduction allows for a design optimized for imaging hundreds of microns beyond the coverslip into water. Water immersion lenses are superior for optical trapping and detection in water because they provide a near-diffraction-limited focusing at distances beyond the cover slip where trapped microspheres are away from the influence of boundary effects imposed by the coverslip. However, there is less demand for water immersion objectives, so they are mainly available as very high-end objectives, with high cost and with many features that are unnecessary for optical trapping.

Our trap was formed using two identical finite-conjugate water-immersion microscope objective lenses (LOMO, model: OM-25)[23], with nominal NA of 1.23, focal length 2.5 mm, and working distance of 140 μm. The

---

[2]The LOMO objectives are in fact based on an late 19th century Zeiss design 'acquired' by LOMO after World War II [84].

[3]As of July 2014 the lenses are no longer available from vendors in the USA

objectives feature a coverslip-thickness-correction adjustment ring, which was set to its lowest setting, 0.1 mm, on both objectives. The relatively simple design, by modern standards, results in a lens that costs an order of magnitude lower than other water immersion lenses with comparable NA.

The transmission 1046 nm was estimated by measuring the transmission through the two lenses with a flowcell in between. Water-index-matching oil was used between the flow cell and each lens, and the flow cell was filled with water. The resulting transmission was approximately 35%, corresponding to transmission of about 60% for each lens. Our laser had a maximum power of 1.2W, but after losses from fiber coupling, the objectives, and scattering from a trapped bead, the maximum power available to the high power detector was slightly more than 100mW, only a factor of two below the detector's damage threshold.

Most modern microscope objectives are infinity conjugate; they are optimized for the specimen to be at the lens' focal plane, its image is formed at infinity. However, the LOMO objectives are finite conjugate: for optimal imaging, the specimen plane is slightly further from the lens than the focal point, and the image is formed 160 mm from the mounting threads of the objective. When used for optical trapping, a diffraction-limited spot is formed when the incoming beam is diverging from a point 160 mm away from the lens.

7.3 Lasers

In the air experiment, the counter-propagating beams originated from the same laser. Cross-coupling and interference were minimized by the use of orthogonally polarized and frequency shifted trapping beams. For trapping in water, it proved more convenient to use two separate lasers, one at 1064 nm, used for both trapping and detection, and one at 532 nm used for only trapping. A detailed schematic of the optical setup is shown in Fig. 7.3.

It was important that both lasers had low intensity fluctuations so as not to perturb the trapped bead. Most critical was intensity noise in the detection laser: although split beam detection suppresses intensity noise, it does not eliminate it completely.

The 1064 nm trapping and detection beam was produced by an internally-stabilized non-planar ring oscillator (NPRO) laser (Innolight GmbH[4], model: Mephisto), with a maximum output power of 1.2 W, a spectral line-width of 1 KHz over 100 ms, and with internal noise-eater enabled, <140 dB/Hz relative intensity noise spectral density. The 532 nm trapping beam was produced by a diode-pumped solid state laser (Coherent, model: Verdi V-10), the same laser used to illuminate trapped beads in the air experiment.

Both lasers were fiber coupled in order to reduce pointing noise. For the 532 laser, an analog PID circuit was used to set the power and suppress intensity noise; the output of the PID controlled an AOM, located upstream

---

[4]Since acquired by Coherent Inc.
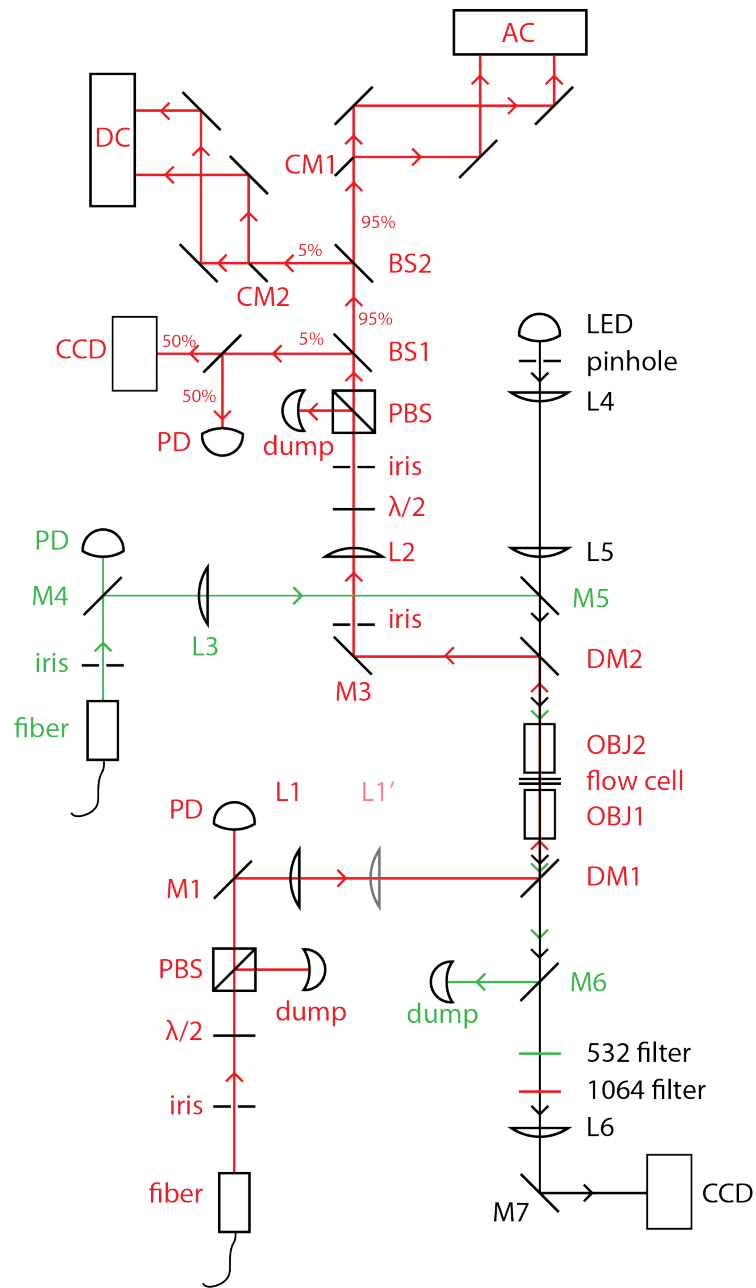
Figure 7.3: Schematic of optical setup for trapping and detection in liquids. The red line represents the optical path of the 1064 nm trapping and detection beam. The green line represents the path of the 532 nm trapping beam. The black line represents the optical path of the illumination beam.

of the fiber, the set point for the PID was generated by an ADC board controlled by the LabVIEW control program. The error signal was measured by a photodiode collecting light leaked through mirror M4 downstream of the fiber output. AOMs are known to degrade the beam profile and in some cases impart pointing noise to the transmitted beam [85]. For this reason the AOM was placed up-stream of the single mode fiber, through which pointing noise is converted into intensity fluctuations, which are then suppressed by the PID loop.

Initially, the power of the 1064 nm laser was controlled in a similar way, except an EOM (electro-optic modulator) was used rather than an AOM. However, electronic noise from the EOM driver introduced more noise to the laser intensity than there was in the absence of power stabilization. The control method was then modified: the power was controlled by a waveplate and polarizing beam-splitter mounted before the fiber input. The waveplate was mounted on a motorized rotary mount which was controlled by the LabVIEW program to set the desired laser power. The EOM was re-purposed to provide a high-frequency intensity modulation which was used for cut mirror alignment, described below.

7.4   Imaging

Optical imaging of the trapping region provided valuable visual access to the trapping region. The CCD image of the trap was used to 'catch' beads as they fell near the trap. It also provided information about the size and

type of trapped bead, the potential presence of contaminants or stray beads approaching the trap, or changes in the position of the trapped particles. It was also used in the alignment process of the two trapping beams.

The optimal configuration of the illumination optics for bright-field imaging (known as Köhler illumination) is for the lamp filament to be imaged onto the back focal plane of the condenser lens. In this case, in the specimen plane, the rays from any point of the filament are parallel. In the dual-beam configuration several constraints were imposed on the illumination optics. The objective OBJ2 had to be used as the condenser, rather than a specialized condenser lens. Also, mirrors DM2 and M5, were in the path of the illumination light, blocking a large portion of its spectrum and also imposing a minimum distance between the remaining illumination optics and OBJ2.

The light source used for optical imaging was was a 100 mW red LED with a 15 degree angle of divergence. A red LED was used for the light source rather than a white one because much of the spectrum of the light emitted by a white LED would be blocked by the mirrors DM2 and M5. A short focal length lens (25 mm) near the LED was used to focus the LED light through a pinhole. The pinhole was then imaged onto the back focal plane of the second objective using a long focal length lens to achieve Köhler illumination.

The image-containing light emerged from OBJ1, passed through two more mirrors, DM1 and M6. Since OBJ1 was a finite conjugate lens, an image of the trapping plane was produced 160 mm away. This virtual image plane was imaged onto a CCD using a single achromatic lens, M6. Moving the

CCD moved closer and further from the objective allowed for adjustment of location of the image plane. This was required because the trap minimum was not necessarily at the focal plane of the objective.

7.5   Trapping optics

Both of the trapping lasers emerged from their fiber output couplers as collimated beams, both with $1/e^2$ waist of 1.5 mm. Since the objectives were finite conjugate, a lens was used to focus each beam 160 mm away from the objective: L1 for the 1064 nm beam and L3 for the 532 nm beam. These shall be referred to as the conjugate lenses. The 1064 nm beam was focused by L1, then reflected by DM1 and focused by OBJ1. It was then recollimated by OBJ2, and reflected by DM1 to be used for detection. The 532 nm beam was focused by L3, reflected by M5, transmitted through DM2, focused by OBJ2, recollimated by OBJ1, transmitted through DM1 and reflected by M6 into a beam dump. DM1 and DM2 are dichroic mirrors with high transmission for 532 nm and high reflectivity for 1064 nm.

The conjugate lenses were useful because they allowed for fine adjustment of the trapping beams. The conjugate lenses were mounted on x-y adjustable lens mounts as well as translation stages that allowed adjustment in the axial position of the lenses. Translating the lenses' x-y position resulted in adjustment of the optical trap in the trapping plane without affecting the trapping beams' angle of incidence. Translation of the lenses along the optical axis enabled adjustment of the axial position of the optical traps. The

123

conjugate lenses also made it convenient to adjust the beam size entering the objectives, and thus NA of the trapping beams. This was done by removing L1 (f=200 mm) and installing L1' (f=50 mm), 150mm away from the location of L1. This would ensure that the beam focus remained at the conjugate point of OBJ1, but the NA reduced by a factor of 4.

7.6   Trap alignment procedure

As noted in Chapter 4, counter-propagating dual-beam optical traps traps are particularly sensitive to misalignment, which can create artificial heating through non-conservative trajectories. Care was taken in setting up the traps to ensure misalignment was minimized.

First, the conjugate lens L1 was removed and mirrors M1 and DM1 were used to align the 1064 nm beam such that it was perpendicular to and centered on the fixed objective OBJ1. This was determined by observing the back-reflections from the multiple internal surfaces OBJ1, transmitted through DM1 which were visible in the imaging CCD camera. The two mirrors were used to adjust the beam angle and position until the back reflections were symmetric and concentric.

Both objectives were temporarily removed, and the path of the collimated beam marked with two irises to define the optical axis on the detection side of the trap. Both objectives were then installed, along with the flow cell. L1 was replaced, and its position was adjusted until the back reflections on the CCD were again symmetric and concentric. OBJ2 was aligned so that the

transmitted beam was collimated and centered on both irises.

Next, conjugate lens L3 was removed, and M4 and M5 were used to align the 532 nm trapping beam, using two reference points: the leakage through M6 of the light transmitted through the optical trap, and the back reflections from OBJ2 visible on the iris next to the output coupler of the green beam. L3 was replaced and aligned to center both reference points.

Rough alignment of the axial position of OBJ2 was performed such that the beam emerging from it was focused at a distance of 160 mm. The stability and behavior of the trap were quite sensitive to the axial position of OBJ2 since this directly affected the separation of the two trap minima. Further fine tuning was performed by optimizing the system with a particle present in the trap.

The index of refraction of silica is sufficiently low that a 3 μm diameter silica microsphere can be trapped using either one of the two trapping beams. The 1064 nm beam is held fixed as much as possible, since adjustment of this beam is coupled to adjustment of the alignment of the detection system. Thus most of the fine tuning is performed on the 532 nm trapping beam. The relative transverse alignment of the two beams can be observed by blocking and unblocking the 532 nm laser when a bead is in the trap. If the green beam was misaligned, the position of the bead would shift. The green beam was adjusted until it no longer caused a shift in the position of the trapped bead.

7.7 Detection System

A second conjugate lens, L2, was used to recollimate the 1064 nm detection beam. This was followed by a half waveplate and PBS, which were used to adjust the power to the detector. A glass plate (BS1) was used to reflect a small portion of the beam for monitoring - which was itself split with a 50/50 beam splitter between a photodiode and CCD camera. The photodiode was used to monitor the power to the detector, while the CCD camera was used to monitor the beam profile. The remaining light was split using BS2, between two cut-mirror detection systems. Most of the power (95%) went to a home built, high power, AC-coupled detector. 5% was sent to a commercial low power, DC-coupled detector (Thorlabs model:PDB110C). The cut mirrors (CM1 and CM2) and CCD camera were positioned such that all three were the same optical path length away from BS1, ensuring that the beam profile imaged by the CCD camera corresponded to the beam profile at both cut mirrors. The beam profile contained information about the location (or absence) of the bead within the trapping beam and changes or instabilities in the bead's position. It was also used to monitor the dependence of the optical gain on the beam profile at the cut mirror.

7.7.1 High power balanced detector

In order to reduce the contribution of photon shot noise to optical position measurement, we built a custom detector with much higher operating power (up to 100 mW per photodiode) than commercially available detec-

tors (the Thorlabs balanced detectors we used had a damage threshold of 5 mW per photodiode). There are three main differences between the design of our custom detector and that of commercially available detectors: lower transimpedance gain, larger photodiodes with higher damage threshold and the addition of AC coupling (high pass filter) before the transimpedance amplifier.

The main limitation to the maximum operating power is thermal damage to the photodiodes. The damage threshold can be increased by using larger area photodiodes. However, though increasing photodiode area increases its capacitance C_p, and the bandwidth of a transimpedance amplifier goes as $\sqrt{1/C_p}$. The photodiodes used in our detector (Excelitas model: C30641) have a 1 mm diameter and capacitance of $<$50 pF when reverse biased at $>$5 V, a particularly low capacitance for such a high area. Similar photodiodes are used in photodetectors used for interferometric gravitational wave detection, which too require high detection power to reduce photon shot noise limit (although usually in circuits with much lower bandwidth) [86–88]. Some of the reduction in bandwidth can be compensated for by reducing the gain, which is permitted since, with the increase in laser power, the photocurrent will have much higher amplitude. While the (transimpedance) gain of the detector used in the air experiment was 1.8×10^5 V/A, the gain of our custom detector was below 1 KV/A.

Another limitation to the maximum input power of the detector is the resulting peak-to-peak voltage swing, which must be within the limits of
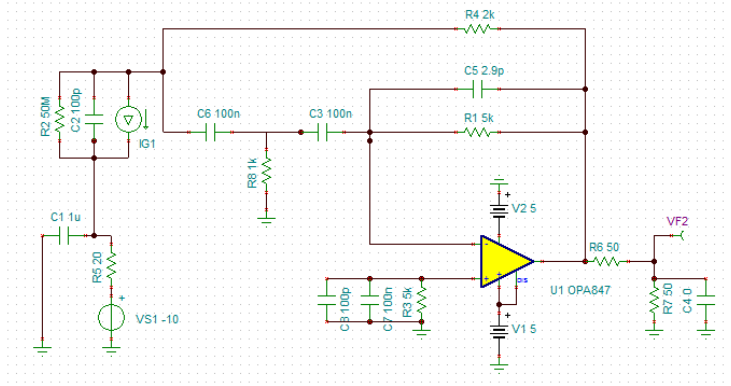
Figure 7.4: Schematic of the circuit for the high power balanced detector, used in SPICE simulations. The photodiode is modeled as a current source (IG1) with resistance (R2) and capacitance (C2) in parallel. Rather than the typical feedback loop of a resistor and capacitor in parallel, the feedback loop in this circuit is based on a Sallen-Key topology [89] which results in a second-order high-pass filter, whose response is determined by R4, C6, R8 and C3.

both the op-amp and the digitizer. A large contribution to the peak-to-peak amplitude in our detected signal was due to low frequency noise, particularly noise centered at harmonics of 60 Hz. These peaks appeared due to not only electronic interference but also acoustic vibration (a 120 Hz hum can be heard by putting ones ear against the wall of the lab). We circumvented this problem by adding a high pass filter before the transimpedance amplifier. A schematic of the detector is shown in figure 7.4. The high-pass filter had -3 dB frequency of ~ 600Hz.

Although high-pass filtering did not significantly affect velocity measurement, it increased the complexity of the fitting. Fitting was usually performed by a 3-parameter fit of either S_x or the MSD to Eq. 1.48 or 1.53. High pass filtering significantly modified S_x at low frequencies and the MSD
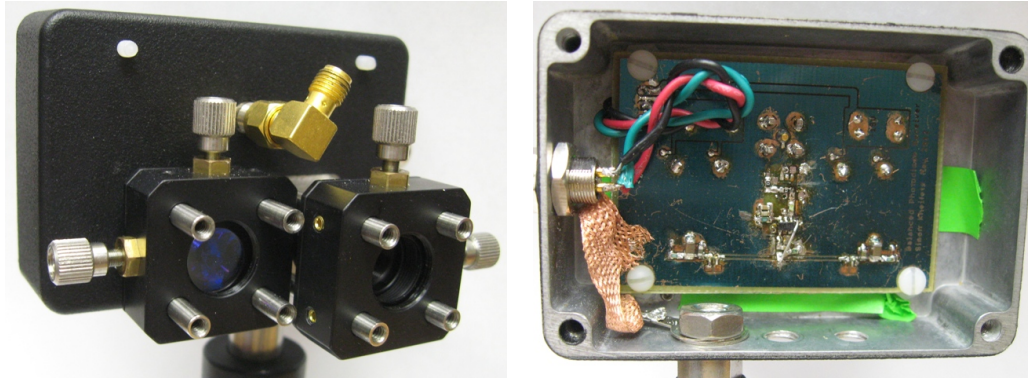
Figure 7.5: Photos of high power balanced detector. The circuit was built mainly using 0603 size surface-mount components to minimize the effects of parasitic capacitance, which could act to reduce the detector's bandwidth.

at long time scales, and directly fitting filtered data to theoretical equations would introduce systematic error into the fit parameters, particularly the trap strength, which only affects the dynamics at the low frequencies which are distorted by the AC coupling. However, as long as the effect of the high-pass filter is known precisely, it can be incorporated into the fit; the data can be deconvolved to infer the PSD or autocorrelation of the unfiltered signal.

For this reason we carefully measured the transfer function of the detector and incorporated it into fitting. The measured transfer function is shown in Fig. 7.6. The fall-off at high frequencies is not only due to the detector bandwidth but also the bandwidth of the digitizer.

7.8   Data acquisition system

The outputs of the AC and DC detectors were digitized using a high bandwidth, ultra low noise ADC board (GaGe model: Razor 1622 Express
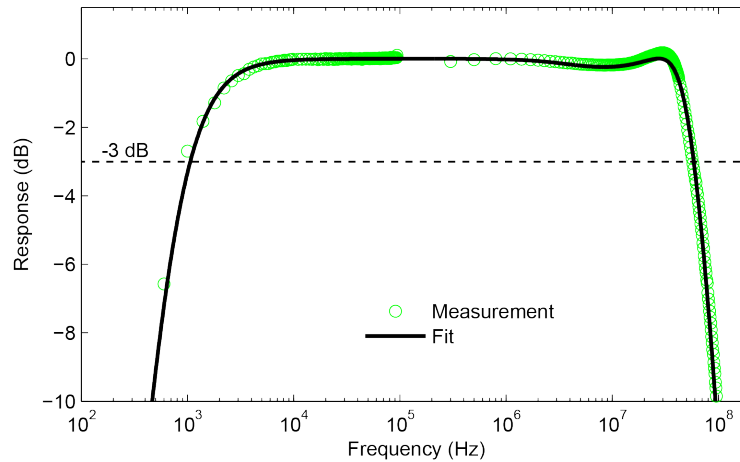
Figure 7.6: Measured AC detector transfer function and its fit. The green dots show the amplitude of the response function recorded through a 125 MHz bandwidth digitizer. The black line shows a fit with and 9 poles and 3 zeros. The resonant peak near 30 MHz is due to the digitizer

CompuScope). The board had two channels, 16 bits of resolution, a maximum sampling rate of 200 Ms/s (100 times faster than that used for the air experiment), and a maximum sample length of 64 million consecutive samples (or 128 million in single-channel operation).

Acquisition was triggered from the LabVIEW control program, and then the acquired data was sent to the control computer. 128 million samples at 16 bit resolution results in very large amounts of data (0.25 Gb, more after conversion into voltage from the raw binary format). So much so that it was necessary to specially program the LabVIEW code to transfer the data one 'page' at a time and then reconstruct it into a single file.

Along with the split-beam detector data, with each acquisition the control program also saved images from the optical imaging and beam profile

monitoring CCDs, the powers of the trapping beams, and the power of the beam entering the detectors.

7.9   Cut mirror alignment

It is important that the cut mirror splits the beam so that the photocurrents of each photodiode of the balanced detector cancel. On the DC coupled detector this can be done by zeroing the output of the detector. For the AC coupled detector, the output is always zeroed. The cut mirror for the AC detector is aligned by adding a 1 MHz amplitude modulation to the 1064 nm laser by applying a small oscillating signal from a function generator to the EOM. When the cut mirror is perfectly aligned, this intensity modulation is absent from the difference signal. If it is misaligned, the signal is visible, and its phase depends on the direction in which the mirror is misaligned.

A feature was written to the LabVIEW control program to lock-in on the modulated signal and read out its amplitude and phase (the phase was known because the function generator and digitizer were synchronized to the same clock). This allowed for precise alignment of the cut mirror. The amplitude modulation was switched off during acquisition of Brownian motion data.

7.10 Optimal filling of objectives

The size of the beam entering the objective, often expressed as the objective filling ratio, is a critical parameter which influences both the trapping strength and the detection efficiency [90]. When trapping particles smaller than the beam waist (< 1 μm diameter) optimal trapping and detection occurs for the smallest possible beam waist, and thus the beam should be as large as possible until clipping inside the objective introduces deviations from a Gaussian profile at the focus.

For larger beads, it is less obvious how to determine filling ratio to optimize detection sensitivity. We determined the optimum empirically by trapping with different configurations and determining the resulting optical gain.

Chapter 8

Measurements of Brownian motion in water and acetone

Unless otherwise stated, all of the data presented in this section come from continuous recordings of trajectories of the thermal motion of a $\sim 3~\mu$m diameter silica microsphere in water, and a $\sim 4~\mu$m diameter barium titanate microsphere in acetone. For both microspheres, the results were calculated from one continuous acquisition of duration ~ 0.35 s, consisting of 64 million points recorded at the digitizer's maximum sampling rate of 200 Ms/s. The recording of the barium titanate microsphere in acetone was acquired with the digitizer's 20 MHz anti-aliasing filter enabled. The recording of the silica microsphere was made with the filter disabled.

8.1 Mean square displacement

For both recordings, the bead diameter, trap strength and calibration constant were determined by fitting the calculated MSDs to the hydrodynamic prediction of Eq. 1.53. The calculated and theoretical MSDs are shown in Fig. 8.2. For the silica microsphere in water, fitting gives a diameter of $d = 2.86 \pm 0.03~\mu$m and trap strength of $K = 1.6 \pm 0.3$ N/m. For the barium titanate
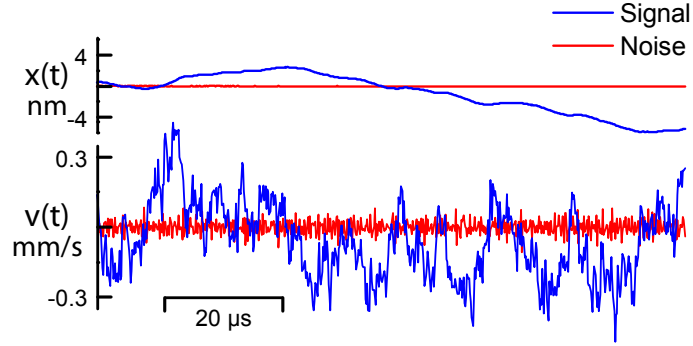
Figure 8.1: Top: A 100 μs long sample of the position fluctuations of a trapped 3.7 μm diameter barium titanate microsphere recorded by the AC detector (blue line), as well as the signal recorded with the same laser power incident on the detector but no microsphere in the trap (red line). Bottom: corresponding velocity calculated from the position measurement in the top trace, using an averaging time of 0.16 μs.

microsphere in acetone, fitting gives a diameter of $d = 3.72\pm0.06$ μm, and trap strength of $K = 3.2\pm0.2$ N/m. For both microspheres, the uncertainty of each fit parameter was determined from the variance in the results of independent MSD fits for 10 sub-trajectories. The red dash-dot lines in Fig. 8.2 represent the MSD of a bead moving at a constant velocity of $v_{th}^* \equiv \sqrt{k_B T/m^*}$. The equipartition predictions of v_{th}^* for the silica and barium titanate particles are 0.35 mm/s and 0.18 mm/s, respectively. For short times, the measured MSDs overlap with the red dash-dot lines of constant velocity, a signature that the dynamics has been observed well into the ballistic regime. The MSD of the silica particle deviates away from ballistic behavior at much shorter times than that of the barium titanate microsphere. For the silica microsphere in water, $\tau_f = 2.0$ μs, while for the barium titanate microsphere in water, $\tau_f = 8.5$. For
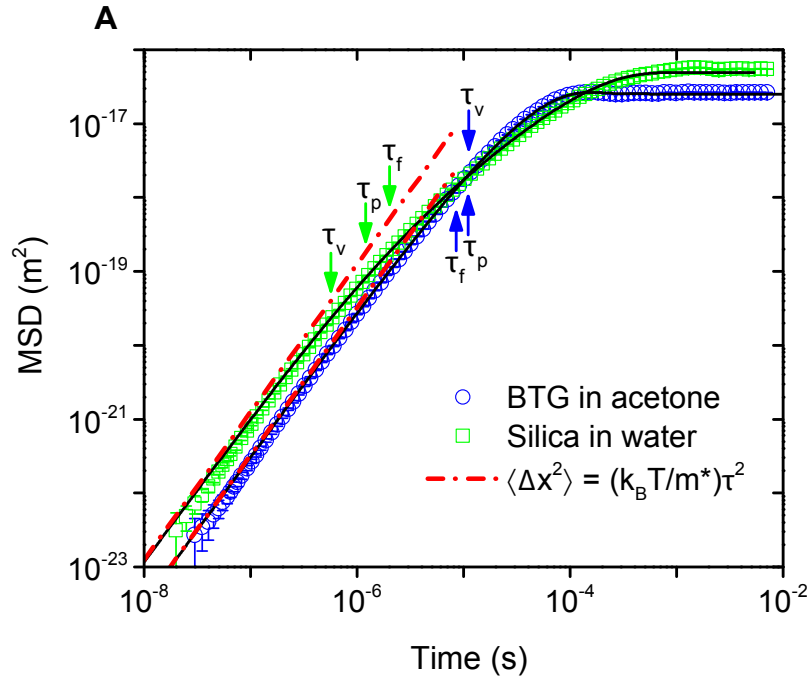
Figure 8.2: Double logarithmic plot of the experimental and theoretical MSD for two different bead-fluid combinations: an optically trapped barium titanate glass (BTG) bead (3.7 μm diameter) in acetone (blue circles; $\tau_p = 11.0$ μs, $\tau_f = 8.5$ μs, $\tau_v = 11.2$ μs), and a silica bead (2.8 μm in diameter) in water (green squares; $\tau_p = 1.2$ μs, $\tau_f = 2.01$ μs, $\tau_v = 0.57$ μs). The red dashed lines indicate the MSD of a particle moving at constant velocity v_{th}^*. The solid black lines correspond to the full hydrodynamic theory of equation 1.53 [91].

both microspheres, the harmonic potential caused the MSD to plateau around $\tau_k = \gamma_s/K$, before the purely diffusive regime is reached.

8.2 Velocity autocorrelation

The transition from ballistic motion is also evident in the calculated C_v curves, shown normalized by v_{th}^{*2} in Fig. 8.3. At short times, C_v decays, to first order, as $1 - \sqrt{t/\tau_v}$ (Eq. 1.54). The approximation is shown by the dashed red lines in Fig. 8.3. This faster-than-exponential decay results from a two-fold action of the Basset force, which increases both the strength of the damping force and the magnitude of thermal force fluctuations at short time scales. The more familiar long-time tails [15, 20, 44, 92] appear at times longer than τ_f. The barium titanate microsphere in acetone has a much larger τ_v (11 μs) than that of the silica microsphere in water (0.57 μs), due to the comparatively larger ρ_p of barium titanate and smaller ρ_f and η of acetone. The larger value of τ_v facilitates instantaneous velocity measurement.

8.3 Position and velocity PSDs

Figure 8.4 shows the position power spectral densities for the two microspheres, as well as the corresponding noise PSDs, calculated from acquisitions where no bead is in the trap, but the laser power incident on the detector, and thus the photon shot noise floor, matches that of the acquisition with beads in the trap. The noise floor for the barium titanate microsphere decays at 20 MHz because the low pass anti-aliasing filter of the digitizer was enabled. En-
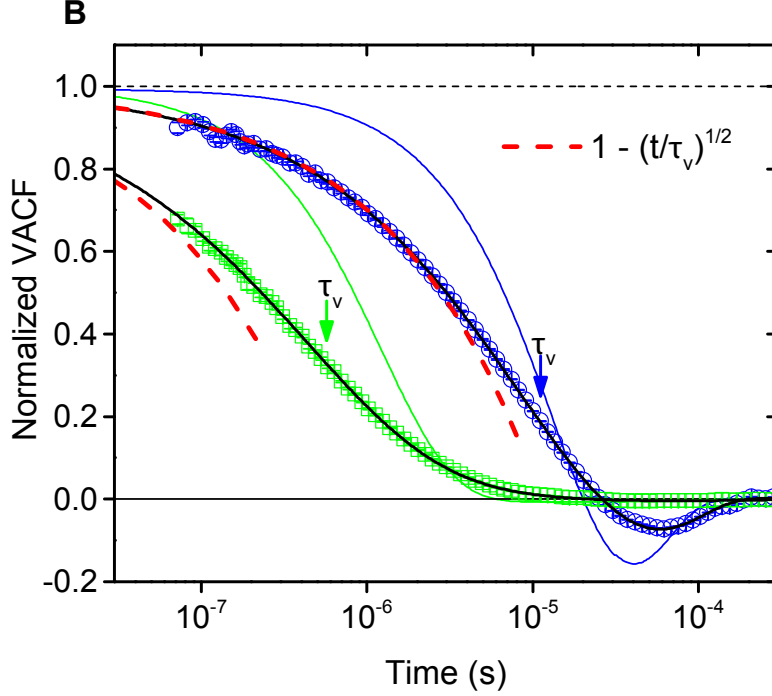
Figure 8.3: Semi-logarithmic plot of the corresponding experimental and theoretical $C_v(t)$ calculated from same data used for Fig. 8.2. The $C_v(t)$ are normalized by v_{th}^{*2}. The horizontal dashed black line guides the eye to the asymptotic value of the $C_v(t)$ at short times. The solid blue and green lines correspond to the predictions of EOU theory (neglecting hydrodynamic interactions) of Eq. 3.15. The dashed red lines correspond to the first-order approximation $1 - \sqrt{t/\tau_v}$ (Eq. 1.54). The solid black lines correspond to the full hydrodynamic theory [91].

abling the filter results in a small reduction in noise, by reducing the amount of noise that gets aliased when the velocity is low-pass filtered. The noise floor for the detection of the silica microsphere in water was 2.9 fm/$\sqrt{\text{Hz}}$, while the noise floor for position detection of the barium titanate glass microsphere in acetone is was 2.1 fm/$\sqrt{\text{Hz}}$.

137

The broad peak centered at 1 MHz in the noise PSD for the silica bead in water is caused by a slight misalignment in the detector's cut mirror, resulting in incomplete suppression of the laser intensity fluctuations.

Figure 8.5A shows the velocity PSD for the two beads (with noise subtracted). Here the difference between the barium titanate microsphere in acetone and the silica microsphere in water is very evident. The difference between the two is somewhat reminiscent of the difference between the velocity PSDs for the silica particle in air at two different pressures, of figure 5.4. The velocity of the silica particle is spread out over a much broader frequency range than the velocity of the barium titanate particle. Also evident is the difference of the slope of the measured PSD to the prediction of EOU theory (thin green and blue lines). The spectra of the two theories have the same area, but EOU theory predicts more velocity fluctuations at low frequencies and less at high frequencies. The basset force is responsible for this shift: the damping and thermal force are stronger for short-time (high frequency) velocity fluctuations due to the coupling of the bead's motion to vorticity close to its surface. At long times (low frequencies), the energy dissipated into the vorticity is returned to the bead in the form of inertial force. Fluctuations at long times are suppressed because the bead has more inertia at long times due to the fluid entrained around it.

Figure 8.5B shows the cumulative velocity PSD (normalized by v_{th}^{*2}) for the two beads (with noise subtracted). The approach of the measured CS_v, towards unity agrees with hydrodynamic theory and is strikingly different from
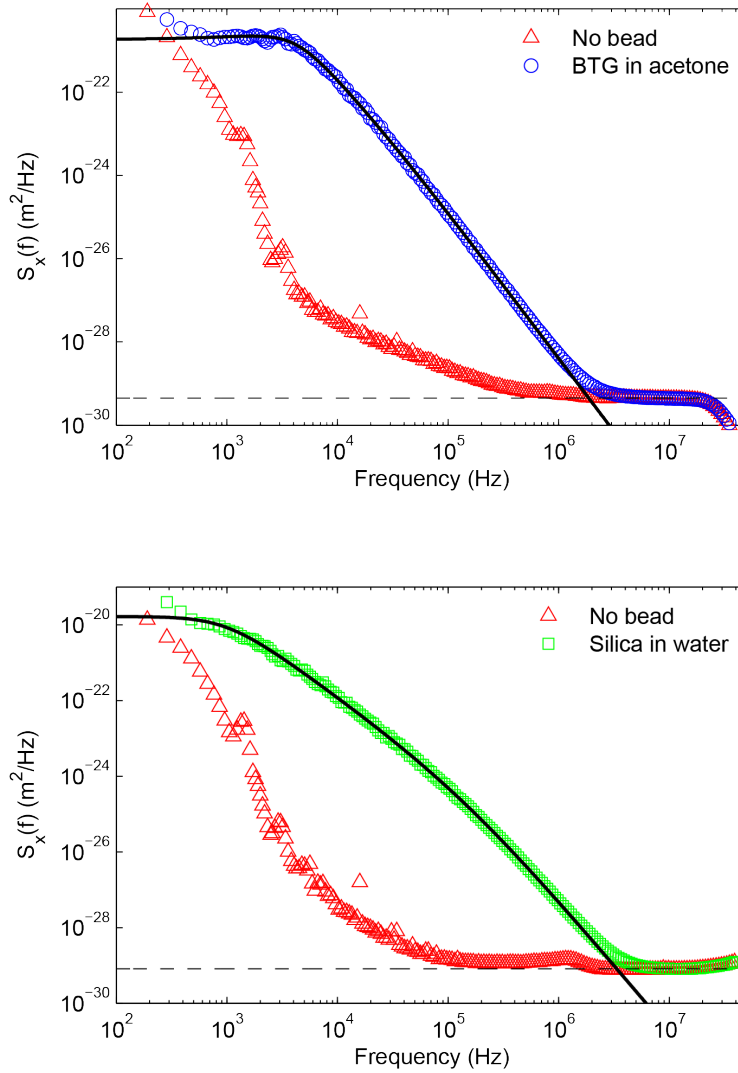
Figure 8.4: The position power spectral density for the barium titanate microsphere in acetone (top, blue circles) and the silica microsphere in water (bottom, green squares). The red triangles in both plots are power spectral densities of laser noise in the balanced detector, matching the input power of the acquisition with the bead present. In the top plot the 25 MHz anti-aliasing filter is enabled. The dashed lines correspond to noise floor of 2.9 fm/$\sqrt{\text{Hz}}$ in for the silica microsphere in water and 2.1 fm/$\sqrt{\text{Hz}}$ for the barium titanate microsphere in acetone.
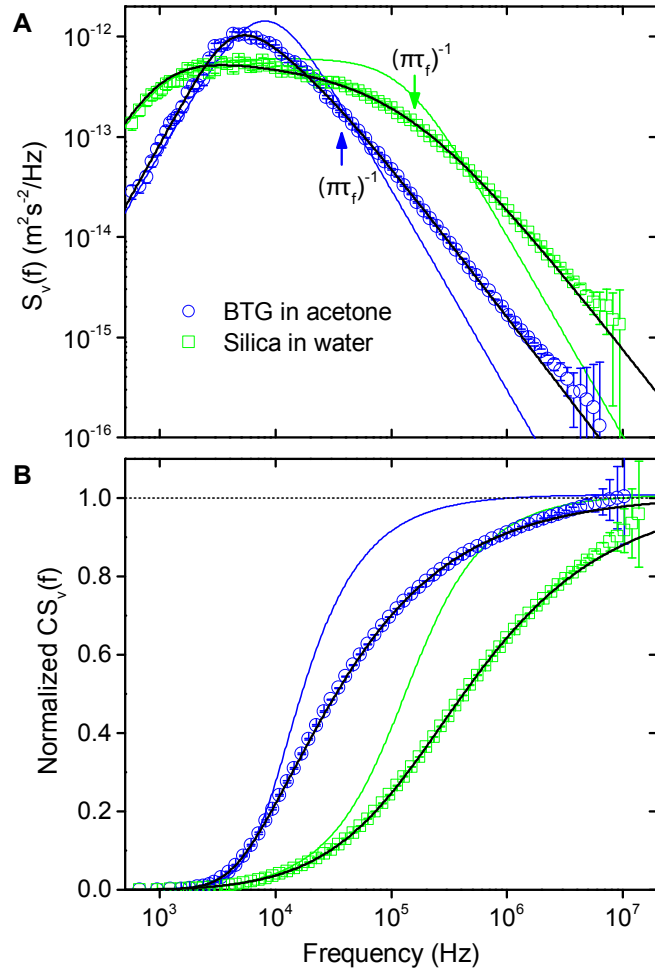
Figure 8.5: (A) Double logarithmic plot of the velocity PSD and (B) semi-logarithmic plot of the cumulative velocity PSD (normalized by v_{th}^{*2}) for the same particles as in Fig 8.2. The solid blue and green lines correspond to EOU theory and the solid black lines correspond to the full hydrodynamic theory [91]. The dashed black line guides the eye to the asymptotic approach towards unity.
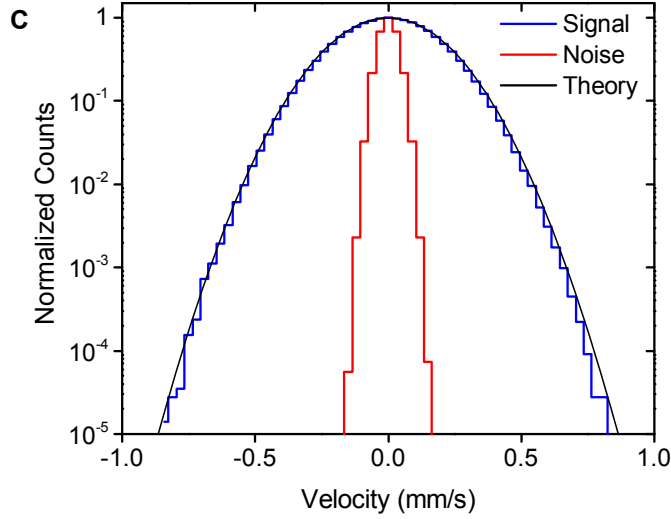
Figure 8.6: The instantaneous velocity distribution for the barium titanate microsphere in acetone (blue line) and the distribution of the velocity noise both calculated with an averaging time of 0.16 μs (red line). The black line shows the theoretical Maxwell Boltzmann distribution for a temperature of 291 K.

the prediction of EOU theory.

8.4 Instantaneous velocity measurement

Even though the heavier barium titanate bead has lower v_{th}^{*2}, its larger τ_v enables measurement further into the ballistic regime than for the silica microsphere in water. We achieve a noise floor of 2.9 fm/$\sqrt{\text{Hz}}$ in the position spectrum for the silica microsphere in water and 2.1 fm/$\sqrt{\text{Hz}}$ for the barium titanate microsphere in acetone, as reflected in Fig. 8.4. Although the noise floor for silica is comparable to that of barium titanate, and v_{th}^{*2} is four times as

large for the silica microsphere, the error in the measurement of instantaneous velocity for the silica microsphere is much larger than that in acetone. For the silica microsphere, τ_v is a factor of ten shorter than for barium titanate; less time is available to average the position signal before the velocity changes significantly from its instantaneous value. However, for the barium titanate microsphere in acetone the longer value of τ_v allows for a longer averaging time. The velocity in Fig. 8.1 is calculated using an averaging time of 0.16 μs per velocity sample. During the averaging time, the velocity autocorrelation decays to $C_v(t = 0.16 \ \mu\text{s}) = 0.89 v_{th}^{*2}$.

Figure 8.6 shows the velocity distribution calculated from the two million velocity measurements that result from averaging and differentiating the recorded position signal. The resulting mean square velocity of the signal is $v_{rms}= 0.174$ mm/s, while that of velocity noise is $v_{rms}=34$ μm/s, within the experimental uncertainty of the predicted Maxwell-Boltzmann distribution, $v_{th}^* =0.180$ mm/s. The bin size in the velocity histogram was chosen to match the root-mean-square magnitude of the noise. Our measured distribution corresponds to a mean kinetic energy 0.93 $k_B T$, to which the noise contributes 0.035 $k_B T$. This corresponds to a measurement of the instantaneous velocity with a signal-to-noise ratio of $\sim$14 dB. A shorter averaging time would increase the fraction of kinetic energy observed at the cost of a lower signal-to-noise ratio.

8.5 Measurements of the thermal force

From our position measurements, we can directly measure the velocity and acceleration of the particle. The acceleration is proportional to the sum of the thermal force, the trapping force and the damping force. By using the parameters determined in the fit, we can determine the magnitude of the damping and trapping forces based on the history of the particle's velocity. The acceleration that is unaccounted for must be due to the thermal force. In this way we are able to infer the thermal force exerted on the microsphere by the fluid, and use it to test predictions about its spectrum, and correlations.

While EOU theory predicts a thermal force with a white (single-sided) power spectral density of $S_{F_{th}} = 4k_BT\gamma_s$ [13], addition of the Basset term results in a colored component: $S_{F_{th}} = 4k_BT\gamma_s(1 + \sqrt{\omega\tau_f/2})$ [91]. The thermal force spectrum can be obtained by dividing the velocity spectrum by the mechanical response function determined by the fitting parameters. The result is shown in Fig. 8.7, in which thermal force spectrum is plotted on a log-log plot with the constant term subtracted. The result is a line with slope $1/2$ corresponding to the $\sqrt{(\omega)}$ term in the real part of the basset force, as predicted by the fluctuation dissipation theorem.

It is also possible to infer the thermal force fluctuations in the time domain. Color in $S_{F_{th}}$ necessarily implies a non-delta autocorrelation function, which can be obtained by Fourier transformation of the thermal force spectrum. The result is shown in (Fig. 8.8). Interestingly, the force is anticorrelated, displaying a $-3/2$ power law dependence over our measurement range.
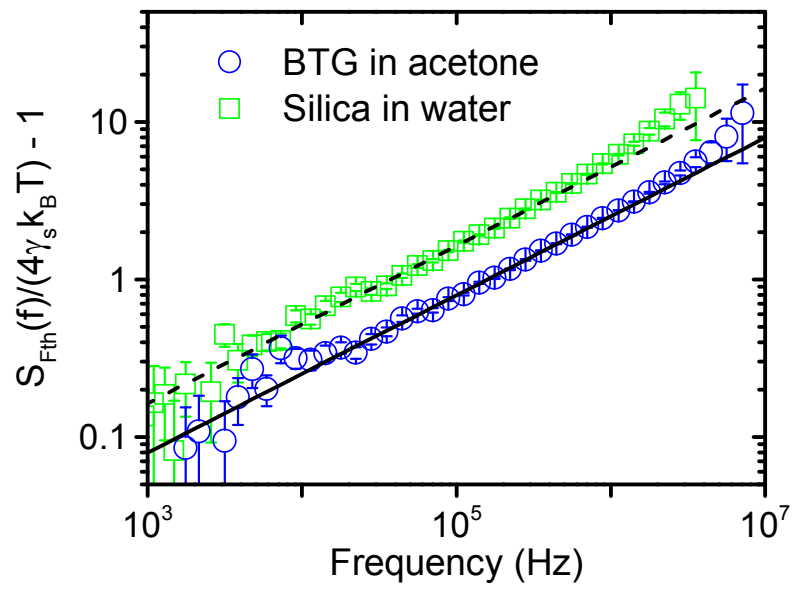
Figure 8.7: Double-logarithmic plot of the colored component of the thermal force power spectral density for the same particles as in Fig 8.2. The black solid and dashed lines correspond to the prediction of the full hydrodynamic theory for the barium titanate and silica microspheres, respectively [91, 93].
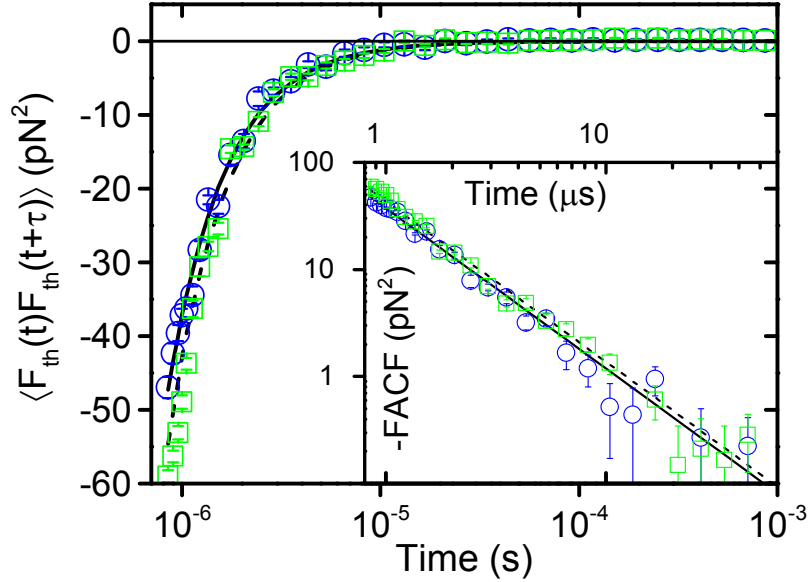
Figure 8.8: A semi-logarithmic plot of the autocorrelation of the thermal force for the two beads. The inset contains a double logarithmic plot of the absolute value of the force autocorrelation, showing its power law dependence. The black solid and dashed lines correspond to the prediction of the full hydrodynamic theory for the barium titanate and silica microspheres, respectively [91, 93].

Whereas Stokes damping leads to a delta-correlated thermal force consisting of uncorrelated 'kicks,' hydrodynamic coupling effectively adds a negative tail to each kick, which is represented by an additional term $-\gamma_s k_B T \sqrt{\tau_f/4\pi} t^{-3/2}$ in the force autocorrelation.

Last but not least is the measurement of the cross-correlation between the thermal force and the velocity $C_{vF_{th}}(\tau) \equiv \langle v(t)F_{th}(t+\tau)\rangle$. It seems natural to consider a causal relationship between the thermal force and the resulting velocity. The velocity in the present depends on the force in the past, thus it
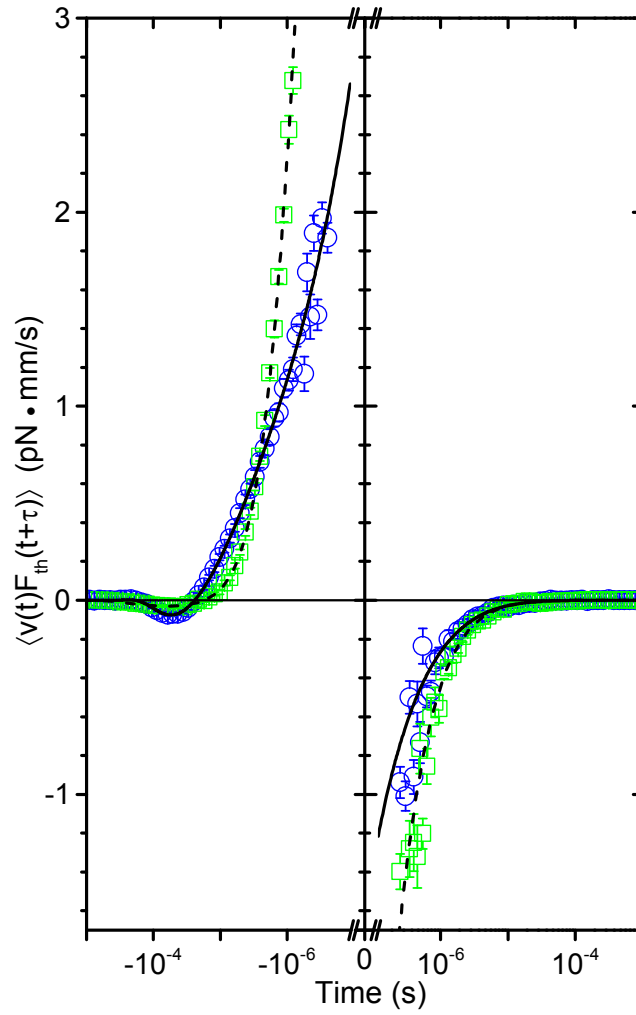
Figure 8.9: Semi-logarithmic plot of the cross correlation of the thermal force with the particle velocity. The cross correlation function is asymmetric in time. The black solid and dashed lines correspond to the prediction of the full hydrodynamic theory for the barium titanate and silica microspheres, respectively [91, 93].

is to be expected that $C_{vF_{th}}(\tau < 0)$ is nonzero and is some kind of decaying function of time. However, unlike autocorrelation functions, cross-correlation functions are not necessarily time-symmetric. On first inspection one would expect that the thermal force of the present should be independent of the velocity in the past. After all, it is the deterministic, damping force, which depends on past velocity; the thermal force should be random. This is not the case. The cross correlation function is calculated by Fourier transformation of the force-velocity cross-power spectrum, and is shown in Fig. 8.9. The horizontal axis is on a logarithmic scale; on the left hand side is correlation between velocity of the future and the thermal force of the past, which is nonzero, as expected. The right hand side shows correlation between velocity of the past and thermal force of the future. EOU theory predicts zero correlation for $\tau > 0$, but the data and hydrodynamic theory show that there is anticorrelation for $\tau > 0$.

Nonzero correlation does not in fact violate causality; this is an example of the mantra that correlation does not imply causation. The nonzero cross correlation can be explained by the fact that the thermal force as nonzero autocorrelation, thus the thermal force in the future is correlated to the thermal force in the past, which directly caused changes in the velocity in the present, thus the future force and present velocity are influenced by the same thermal force fluctuations of the past [93, 94].

8.6   Outlook

Prior to this work, the trajectory in velocity space of the Brownian motion of a particle in liquid was inaccessible. In earlier work, signatures of the ballistic regime were observed, but only in the time-averaged correlation functions in which uncorrelated noise gets suppressed [95]. The actual trajectory in velocity space could not be observed, because detection techniques were unable to resolve the particle's displacements over the short times during which velocity remains approximately constant.

In this work, the measurement was made possible by pushing the noise and bandwidth limits of single particle tracking and by careful choice of system parameters, resulting in the resolution of instantaneous velocity with an SNR of 16 dB. Our measurements confirmed a Maxwell-Boltzmann probability distribution for the velocity, with the particle mass replaced by an effective mass that accounts for the inertia of the displaced liquid.

The low noise of our detection system also allowed resolution of the time-averaged properties of the Brownian trajectories to much shorter time scales than before. This allowed for confirmation of previously untested predictions of the theory of hydrodynamic Brownian motion. This included the faster-than-exponential decay of the VACF, as well as short time correlations of the random thermal force.

There are many directions in which this work can be extended. To begin with, it may be possible to use the existing data to further study equilibrium

Brownian motion. There are also several possibilities for making more precise measurements of equilibrium dynamics. Also, the techniques of this work could be applied to the study of nonequilibrium statistical mechanics and equilibrium motion in complex fluids [96] or confined geometries [67, 97].

8.6.1 Further study of existing data

Following the initial publication of the data presented in Chapter 5 [10], the same data was used to demonstrate that for trajectories with fixed, nonzero initial velocity, the dispersion grows as time to the third power [98]. In water, the memory effect might result in deviation from this behavior.

Aside from the instantaneous velocity distribution, all other time-averaged functions presented in Chapter 5 are effectively two-point correlation functions. It should be possible to calculate higher-order correlation functions, or other statistical properties such as zero-crossing statistics, which could shed light on otherwise unseen physical processes.

Another interesting aspect of Brownian trajectories is that of time-symmetry. The entropy of the fluid-particle system stays constant, thus it should not be possible to determine the arrow of time from a recording of Brownian motion. However, most formulations of Brownian motion are written in a causal way (for instance, the Langevin equation). Studying the time-symmetry properties of recorded brownian trajectories could shed light on whether the system is truly in equilibrium.

8.6.2 Improving velocity measurement

It is natural to think about extending this work to reach even shorter time scales. The theory of hydrodynamic interaction presented in Chapter 6 does not take into account the nonzero compressibility of the fluid. With nonzero compressibility, there exists further detail in the trajectory of Brownian motion at even shorter time and length scales. At the time scale $\tau_c = d/c$, where d is the particle diameter and c is the speed of sound in fluid, Eq. 6.4 is no longer accurate. At such time scales, motion of the microsphere is decoupled from its fluid envelope; the fluid compresses rather than flowing out of the way. The effective mass term can no longer be lumped with the bare mass. If the particle's velocity is measured with time resolution shorter than τ_c, it is expected that its variance will be $v_{th}^2 = k_B T/m_p$ rather than $v_{th}^{*2} = k_B T/m^*$.

In order to access such short time scales, it will be necessary to push the limits even further by reducing the noise floor, increasing optical gain, and optimizing the materials to increase τ_c without decreasing the SNR. Increasing the laser power to reduce the noise floor ultimately faces the problem of heating of the fluid and microsphere near the high intensity of the focused detection beam. One possible strategy to improve the time resolution of velocity measurement without increasing the laser power is to switch from a CW detection laser to a pulsed detection laser. For the CW measurement used in this work, the averaging time of each sampled velocity is the same as the time between samples. If a pulsed laser were used, it could be possible, with the same average laser power and the same sampling rate, to have a much shorter

averaging time for each sample. As the averaging time is reduced, the variance of the measured velocity should increase from v_{th}^{*2} to v_{th}^2. As the averaging time is reduced, it is more likely to reveal any deviation of the shape of the velocity distribution from that of the Maxwell-Boltzmann distribution. By the central limit theorem, the distribution of a time averaged random variable will tend to approach a normal distribution, thus time averaging can conceal any underlying deviations.

As for the velocity distribution measured in this work, it only places an upper bound on deviation from the predicted distribution. There are three limitations: averaging time, as discussed earlier, measurement noise, which effectively imposes horizontal error bars on the measured distribution, and finally the number of samples, which limits how much of the tails of the distribution can be observed. It should be possible to improve on the latter limitation by recording the trajectory for a long period of time.

Another possible extension of this work would be to independently measure the mechanical response function of the microsphere. In Chapter 8, the thermal force was inferred by assuming a mechanical response function determined by theory and the fit parameters. This makes the assumption that the theoretical prediction is correct. A more robust method would be to independently measure the mechanical response of the microsphere by driving with an external force and measuring the response of the velocity. Then, the thermal force of the undriven motion can be determined more precisely and more directly. One method to apply an external driving force would be to

radiation pressure from a laser beam from the side of the microsphere, similar to the way a feedback force was applied in Ref. [55].

8.6.3 Nonequilibrium thermodynamics

Since the 1990s there as been increasing theoretical study of nonequilibrium thermodynamics, including the extension of the fluctuation dissipation theorem to systems not in thermal equilibrium [99]. Most tests of these predictions have been made by studying the fluctuation of the position of a Brownian particle in a nonequilibrium environment [67, 97, 100–104]. The ability to measure trajectories in velocity will allow direct access to statistics of the energy and entropy exchange between the microsphere and the fluid.

One possible extension is to measure the velocity of trapped gold nanospheres. Trapping of gold nanospheres in water should possible using the same optical trap used in this work [105], and trapping has been report of gold nanospheres as small as 10 nm and as large as 250 nm [106]. The density of gold is among the highest of any room-temperature solid, (19.3 g/cm^3), almost five times that of the barium titanate microspheres used in this work. The optical gain for a gold nanosphere should be much higher than that of a dielectric sphere of the same size, though it is harder to estimate because of the complex dielectric constant of gold. The skin depth, at which the field of a 1064 nm laser is attenuated by a factor of e, is ~ 20 nm. For diameters comparable to the skin depth, the polarizability, and thus optical gain, of a sphere, is proportional to $\alpha \propto |(\tilde{\epsilon_1} - \epsilon_2)/(\tilde{\epsilon_1} + 2\epsilon_2)|$, where $\tilde{\epsilon_1}$ is the complex

dielectric constant of the microsphere and ϵ_2 is the dielectric constant of the fluid. For a silica sphere in water, this factor is 0.12, for a barium titanate sphere in water, it is 0.43, while for a gold nanosphere it is 1.13. However, for sphere diameters much larger than the skin depth, this factor will be somewhat reduced.

A trapped gold nanosphere would absorb much more of the laser power than a dielectric sphere, which would cause heating. The resulting motion should deviate from the predictions of equilibrium Brownian motion because there is constant energy flow from the microsphere to the fluid [107–109]. Because the density of gold is much higher, the correlation time of the bead's velocity should be much longer than a dielectric sphere of the same size, thus it should be possible to resolve nonequilibrium motion of such a sphere in velocity space.

Another possibility is to measure the velocity of a trapped microsphere in a moving fluid. This would perhaps break the symmetry of the velocity distribution and of the velocity dynamics.

Appendix

Appendix 1

Additional Theory

1.1 Derivation of EOU theory

1.1.1 Solution of the Langevin equation for a free particle

The solutions for average behavior of the system described by Eq. 3.4, namely the resulting mean square displacement, (MSD) and velocity autocorrelation function (C_v), can by derived using the fluctuation dissipation theorem [12], however this case is simple enough that it can be solved in the time domain using only the following assumptions about mean and autocorrelation of the thermal force:

$$\langle F_{th}(t) \rangle = 0, \tag{1.1}$$

$$\langle F_{th}(t) F_{th}(t') \rangle = A\delta(t - t'), \tag{1.2}$$

where A is some proportionality constant and δ is the Dirac delta function. The first assumption states that on average the force does not push the bead in any given direction (any part that did would be contained in the systematic, damping term). The second assumption is a statement that value of the force at any instant in time does not (systematically) depend on its value at any other time. A reasonable assumption given that F_{th} is the sum of trillions of tiny molecular impulses.

155

Solving 3.4 for $v(t)$ with initial conditions $v(0) = v_0$, $x(0) = 0$ and some arbitrary $F_{th}(t)$ gives [13]:

$$v(t) = v_0 e^{-t/\tau_p} + \frac{e^{-t/\tau_p}}{m_p} \int_0^t e^{t'/\tau_p} F_{th}(t')dt'. \tag{1.3}$$

Taking the product of the velocity at two different times t_1 and t_2, with $t_2 > t_1$, and averaging over the distribution of $[F_{th}(t)]$ gives the velocity autocorrelation function, $C_v \equiv \langle v(t_1)v(t_2)\rangle$:

$$C_v = v_0^2 e^{-(t_1+t_2)/\tau_p} + \frac{Ae^{-(t_1+t_2)/\tau_p}}{m_p^2} \int_0^{t_1} \int_0^{t_2} e^{(t_1'+t_2')/\tau_p} \delta(t_1' - t_2')dt_1'dt_2' \tag{1.4}$$

$$= v_0^2 e^{-(t_1+t_2)/\tau_p} + \frac{Ae^{-(t_1+t_2)/\tau_p}}{m_p^2} \frac{\tau_p}{2}[e^{2t_1/\tau_p} - 1] \tag{1.5}$$

where, in the first line, the cross terms are not shown because they average to zero. The double integral is evaluated under the assumption that $t_2 > t_1$. If not, they must be switched. The expression is greatly simplified in the limit that $t_1 + t_2 \to \infty$:

$$\lim_{t_1+t_2\to\infty} C_v(t_1, t_2) = \frac{A}{2\gamma_s m_p} e^{-|t_2-t_1|/\tau_p}. \tag{1.6}$$

This long time result depends neither on the initial velocity, nor the magnitudes of t_1 or t_2. It depends only on the time difference $t \equiv t_2 - t_1$, thus we can write:

$$C_v(t) = \frac{A}{2\gamma_s m_p} e^{-|t|/\tau}. \tag{1.7}$$

Though an initial velocity was specified, it is forgotten by the system in the long time limit, and any a trajectory with initial velocity will revert to one

obeying equilibrium statistics after sufficient time. Consistency with equipartition requires that $\langle v^2 \rangle = C_v(0) = k_B T / m_p$, thus:

$$A = 2\gamma_s k_B T. \tag{1.8}$$

This result is a special case of the fluctuation-dissipation theorem: the strength of the thermal force is proportional to the strength of dissipation. One way to understand this relationship by considering the symmetry between damping, in which the particle's kinetic energy is converted into thermal motion of the fluid, and the thermal force, in which kinetic energy from fluid fluctuations is converted to kinetic energy of the sphere. The two effects can be thought of as the same interaction going in different directions in time, thus magnitude of one should be related to that of the other.

Integrating 1.3 a second time gives the position of the particle [13]:

$$x(t) = x_0 + \int_0^t v(t')dt'. \tag{1.9}$$

Using this expression, the mean square displacement can be written in terms of the velocity autocorrelation, $C_v(t_1, t_2)$:

$$\langle (x(t_2) - x(t_1))^2 \rangle = \left\langle \left(x_0 + \int_0^{t_2} v(t')dt' - x_0 - \int_0^{t_1} v(t')dt' \right)^2 \right\rangle \tag{1.10}$$

$$= \left\langle \left(\int_{t_1}^{t_2} v(t')dt' \right)^2 \right\rangle \tag{1.11}$$

$$= \int_{t_1}^{t_2} \int_{t_1}^{t_2} \langle v(t)v(t') \rangle dt dt'. \tag{1.12}$$

At this stage we again take the limit $t_1 + t_2 \to \infty$, and substitute Eq. 1.7 into the integrand. Since $C_v(t) = C_v(|t|)$ the inner integral must be split into two

parts for time ordering:

$$\langle (x(t_2) - x(t_1))^2 \rangle = \langle v^2 \rangle \int_{t_1}^{t_2} \left(\int_{t'}^{t_2} e^{-(t-t')/\tau_p} dt + \int_{t_1}^{t'} e^{-(t'-t)/\tau_p} dt \right) dt' \quad (1.13)$$

$$= 2\tau_p^2 \langle v^2 \rangle \left(\frac{t_1 - t_2}{\tau_p} - 1 + e^{-(t_1 - t_2)/\tau_p} \right) \quad (1.14)$$

This result is again independent of initial conditions and only depends on the time difference. The MSD is thus:

$$\langle [\Delta x(t)]^2 \rangle = \frac{2\tau_p^2 k_B T}{m_p} \left(\frac{t}{\tau_p} - (1 - e^{t/\tau_p}) \right) \quad (1.15)$$

For $t \gg \tau_p$ it reduces to Einstein's theory:

$$\langle [\Delta x(t)]^2 \rangle = 2Dt \quad (1.16)$$

while for $t \ll \tau_p$ it describes ballistic (constant-velocity) motion:

$$\langle [\Delta x(t)]^2 \rangle = \frac{k_B T}{m_p} t^2. \quad (1.17)$$

1.1.2 Solution of the Langevin equation with a harmonic potential

Since $\text{MSD}(t) \equiv \langle \Delta^2(t_1, t_1 + t) \rangle = 2(C_x(0) - C_x(t))$, we will calculate the MSD by first calculating C_x, the position autocorrelation function, which is the Fourier transform pair of the position PSD$S_x(\omega)$.

Taking the Fourier transform of both sides and solving for $\tilde{x}(\omega) \equiv \mathcal{F}[x(t)]$:

$$\tilde{x}(\omega) = \frac{\tilde{F}_{th}(\omega)}{-m_p \omega^2 + K - i\omega \gamma_s} \quad (1.18)$$

Squaring the magnitude of $\tilde{x}(\omega)$ gives the power spectral density[1] corresponding to $x(t)$

$$S_x = \tilde{x}(\omega)\tilde{x}^*(\omega) = \frac{S_{F_{th}}}{m_p^2(\omega_0^2 - \omega^2)^2 + \omega^2\gamma_s^2} \tag{1.19}$$

Where $\omega_0 \equiv \sqrt{K/m_p}$ is the trap resonant frequency and $S_{F_{th}}$ is the thermal force PSD which can be obtained from its autocorrelation function defined in Eq. 1.2:

$$S_{F_{th}}(\omega) = \int_{-\infty}^{\infty} A\delta(t)e^{i\omega t}dt = 2\gamma_s k_B T. \tag{1.20}$$

Any delta-correlated process has a flat PSD, which is why such processes are often referred to as "white noise". The resulting position autocorrelation is:

$$C_x(t) = \int_{-\infty}^{\infty} \frac{S_x(\omega)}{2\pi} e^{-i\omega t} d\omega \tag{1.21}$$

$$= \frac{2\gamma_s k_B T}{2\pi} \int_{-\infty}^{\infty} \frac{e^{-i\omega t}}{-m_p\omega^2 + K - i\omega\gamma_s} d\omega \tag{1.22}$$

$$. \tag{1.23}$$

The denominator of 1.23 can be written as $m_p^2(\omega^2 + \tau_+^{-2})(\omega^2 + \tau_-^{-2})$ where

$$\tau_\pm = \frac{2\tau_p}{1 \pm 2\tau_p\omega_1} \tag{1.24}$$

and $\omega_1 = \sqrt{\omega_0^2 - (2\tau_p)^{-2}}$ is the corner frequency. The system is underdamped when ω_1 is real ($\omega_0 > 1/2\tau_p$), critically damped when $\omega_1 = 0$ and underdamped when ω_1 is imaginary ($\omega_0 < 1/2\tau_p$). For the experiments discussed in Ch. 4, the system is always underdamped. For a microsphere in an optical trap in

---

[1]Unless otherwise stated, the power spectral densities given in this paper are all double sided

159

water, at laboratory scale laser power the system will be heavily overdamped, though an accurate description of such a system (given in Ch. 6), requires modification of Eq. 3.4 to take into account the inertia of the fluid.

Integration using the Cauchy residue theorem gives:

$$C_x(t) = \frac{2\gamma_s k_B T}{2m_p^2} \left[\frac{e^{it/\tau_-}}{\tau_-^{-1}(\tau_+^{-2} - \tau_-^{-2})} - \frac{e^{it/\tau_+}}{\tau_+^{-1}(\tau_+^{-2} - \tau_-^{-2})} \right] \qquad (1.25)$$

$$(1.26)$$

The VACF can be found by Fourier transformation of the velocity power spectrum, which is related to the position power spectrum by $S_v(\omega) = \omega^2 S_x(\omega)$. Equivalently, it can be found using the identity $C_v(t) = -(d^2/dt^2)C_x$, giving:

$$C_v(t) = \frac{2\gamma_s k_B T}{2m_p^2} \left[\frac{e^{-t/\tau_+}}{\tau_+(\tau_+^{-2} - \tau_-^{-2})} - \frac{e^{-t/\tau_-}}{\tau_-(\tau_+^{-2} - \tau_-^{-2})} \right] \qquad (1.27)$$

In the underdamped case, $\tau_\pm$ are real, resulting in

$$C_x(t) = \frac{A}{2\gamma_s m_p \omega_0^2} \left(cos\omega_1 t + \frac{sin\omega_1 t}{2\omega_1 \tau_p} \right) e^{-t/2\tau_p} \qquad (1.28)$$

and

$$C_v(t) = \frac{A}{2\gamma_s m_p} \left(cos\omega_1 t - \frac{sin\omega_1 t}{2\omega_1 \tau_p} \right) e^{-t/2\tau_p} \qquad (1.29)$$

Again, consistency with equipartition results in the same value for A as Eq. 1.8, giving $\langle x^2 \rangle = C_x(0) = k_B T/m\omega_0^2$ and $\langle v^2 \rangle = C_v(0) = k_B T/m\omega_0^2$. The MSD is:

$$\text{MSD}(t) = \frac{2k_B T}{m_p \omega_0^2} \left[1 - e^{-t/2\tau_p} \left(cos\omega_1 t + \frac{sin\omega_1 t}{2\omega_1 \tau_p} \right) \right], \qquad (1.30)$$

which, at short times, has the same limit as the free particle (Eq. 1.17, since for short intervals the trap appears as a constant force, whose time average is

zero. The long time MSD of a trapped particle is very different from that of a free particle. It is a constant, since after time of order $1/\omega_0$ the particle turns around within the trap, and never travels much further than the amplitude of (damped) oscillation.

In the overdamped case,

$$C_x(t) = \frac{k_B T}{m_p \omega_0^2} \left[\frac{1}{2|\omega_1|\tau'_+} e^{-t/\tau'_-} - \frac{1}{2|\omega_1|\tau'_-} e^{-t/\tau'_+} \right], \tag{1.31}$$

$$C_v(t) = \frac{k_B T}{m_p} \left[-\frac{1}{2|\omega_1|\tau'_-} e^{-t/\tau'_-} + \frac{1}{2|\omega_1|\tau'_+} e^{-t/\tau'_+} \right], \tag{1.32}$$

$$\text{MSD}(t) = \frac{2k_B T}{m_p \omega_0^2} \left[1 - \frac{1}{2|\omega_1|\tau'_+} e^{-t/\tau'_-} + \frac{1}{2|\omega_1|\tau'_-} e^{-t/\tau'_+} \right]. \tag{1.33}$$

Where

$$\tau'_\pm = \frac{2\tau_p}{1 \pm 2\tau_p|\omega_1|} \tag{1.34}$$

For the Brownian motion of a free particle, the position and velocity power spectral densities are:

$$S_x = \frac{2\gamma k_B T}{m_p^2 \omega^4 + \omega^2 \gamma^2} \tag{1.35}$$

$$S_v = \frac{2\gamma k_B T}{m_p^2 \omega^2 + \gamma^2} \tag{1.36}$$

For a Brownian particle in a harmonic potential, the position and velocity PSDs are:

$$S_x = \frac{2\gamma k_B T}{m_p^2 (\omega_0^2 - \omega^2)^2 + \omega^2 \gamma^2} \tag{1.37}$$

$$S_v = \omega^2 S_x = \frac{2\omega^2 \gamma k_B T}{m_p^2 (\omega_0^2 - \omega^2)^2 + \omega^2 \gamma^2} \tag{1.38}$$

161

1.2 Derivation of hydrodynamic Brownian motion

To include the effects of hydrodynamic interaction, the term $\gamma_s v$ the Langevin equation of Eq. 3.4 is replaced with the friction force of Eq. 6.4:

$$m_p \ddot{x}(t) = -Kx - \left[\frac{m_f}{2} \ddot{x}(t) + \gamma_s \left(\dot{x}(t) + \sqrt{\frac{\tau_f}{\pi}} \int_{-\infty}^{t} \frac{\ddot{x}(t')dt'}{\sqrt{t-t'}} \right) \right] + F_{th}(t) + F_{ext}(t), \tag{1.39}$$

the result is an example of a generalized Langevin Equation (GLE), the generic form of which is:

$$m_p \ddot{x}(t) = -(\gamma * \dot{x})(t) + F_{th}(t) + F_{ext}(t) \tag{1.40}$$

where $\gamma(t)$ is the damping kernel which represents the retarded damping force. The convolution $*$ is defined as:

$$(\gamma * \dot{x})(t) = \int_{-\infty}^{\infty} \gamma(t-t')\dot{x}(t')dt' \tag{1.41}$$

$$= \int_{-\infty}^{t} \gamma(t-t')\dot{x}(t')dt'. \tag{1.42}$$

an important feature of the GLE is that causality is built into the damping kernel. In this section we summarize the results. The results in this section reduce to those of EOU theory by replacing $\gamma[\omega]$ with γ_s.

1.2.1 Thermal force autocorrelation

Making the assumption of a delta-correlated thermal force (Eq. 1.2 for Eq. 1.39 would lead to solutions that contradict equipartition. The correct expression for the thermal force autocorrelation is predicted by the fluctuation

dissipation theorem (FDT) to be:

$$S_{F_{th}} = 2m_p \langle v^2 \rangle \operatorname{Re}(\gamma[\omega]) \tag{1.43}$$

Where $\gamma[\omega]$ is the Laplace transform of $\gamma(t)$ from equation 1.40; for a sphere in liquid, $\gamma[\omega]$ is the same as given in equation 6.1. An explicit form for $\gamma(t)$ would contain differential operators.

$$S_{F_{th}}(\omega) = 2\gamma_s k_B T (1 + \sqrt{\omega \tau_f / 2}), \tag{1.44}$$

and the corresponding thermal force autocorrelation is:

$$C_{F_{th}}(t) = 2\gamma_s k_B T \left[\delta(t) + \frac{1}{2}\sqrt{\frac{\tau_f}{\pi}} t^{-3/2} \right]. \tag{1.45}$$

1.2.2 Mobility

The complex mobility $\mu(\omega)$ describes the amplitude and phase response of the particle's velocity to an oscillating driving force:

$$\mu(\omega) = \frac{i\omega/m_p}{(\omega^2 - \omega_0^2) + i\omega\gamma[\omega]/m_p} \tag{1.46}$$

1.2.3 Position and velocity power spectral densities

The position PSD is

$$S_x(\omega) = \frac{2k_B T \operatorname{Re} \gamma[\omega]}{\left(m_p(\omega^2 - \omega_0^2) - \omega \operatorname{Im} \gamma[\omega]\right)^2 + (\omega \operatorname{Re} \gamma[\omega])^2} \tag{1.47}$$

$$= \frac{2\gamma_s k_B T (1 + \sqrt{\omega\tau_f/2})}{\left(\omega^2(m^* + (9m_f/2)\sqrt{1/2\omega\tau_f}) - \omega_0^2 m_p\right)^2 + \left(\omega\gamma_s(1 + \sqrt{\omega\tau_f/2})\right)^2}. \tag{1.48}$$

The velocity PSD is $S_v = \omega^2 S_x$.

$$S_v(\omega) =$$
$$\frac{2\omega^2 \gamma_s k_B T (1 + \sqrt{\omega \tau_f / 2})}{\left(\omega^2(m^* + (9m_f/2)\sqrt{1/2\omega\tau_f}) - \omega_0^2 m_p\right)^2 + \left(\omega\gamma_s(1 + \sqrt{\omega\tau_f/2})\right)^2} \qquad (1.49)$$

1.2.4 Correlation functions

The velocity autocorrelation is the sum of four terms:

$$C_v(t) = \frac{1 + \epsilon_{ijkl}}{2} \frac{k_B T}{m^*} \frac{c_i^3 \exp(c_i^2 t) \operatorname{erfc}(c_i \sqrt{t})}{(c_i - c_j)(c_i - c_k)(c_i - c_l)} \qquad (1.50)$$

where ϵ_{ijkl} is the Levi-Civita permutation symbol[2], $\operatorname{erfc}(z)$ is the complimentary error function[3], and the four constants c_i are the complex solutions of the quartic equation:

$$m^* s^2 + \gamma_0 \sqrt{\tau_f} s^{3/2} + \gamma_0 s + K \qquad (1.51)$$

$$= m^*(\sqrt{s} + c_1)(\sqrt{s} + c_2)(\sqrt{s} + c_3)(\sqrt{s} + c_4) \qquad (1.52)$$

The mean square displacement has a similar form (c_i are the same as those above):

$$\text{MSD}(t) = \frac{2k_B T}{k} + \frac{2k_B T}{m^*} \frac{1 + \epsilon_{ijkl}}{2} \frac{\exp(c_i^2 t) \operatorname{erfc}(c_i \sqrt{t})}{c_i(c_i - c_j)(c_i - c_k)(c_i - c_l)} \qquad (1.53)$$

---

[2]$(1 + \epsilon_{ijkl})/2$ means there are four terms in the sum, the four cyclic permutations [1,2,3,4],[2,3,4,1],[3,4,1,2] and [4,1,2,3]

[3]the built-in MATLAB erfc(x) function is only defined for real x, but the c_i are complex. A third party MATLAB function for the complex generalization of erfc is available at [110]

Expansion of Eq. 1.50 about $t = 0$ in powers of $t^{1/2}$ results in a much simpler expression:

$$C_v(t) \approx \frac{k_B T}{m^*}\left(1 - \sqrt{t/\tau_v}\right) \tag{1.54}$$

with

$$\tau_v \equiv \frac{\pi r^2 (\rho_p + \rho_f/2)^2}{81 \eta \rho_f} = \frac{\pi}{4}\frac{\tau_p^{*2}}{\tau_f} \tag{1.55}$$

1.2.5 Force-velocity cross correlation

The complex force-velocity cross-power spectral density is

$$\beta S_{v,F_{th}}(\omega) = m_p \mu(\omega)\gamma^*[\omega] \tag{1.56}$$

While the force-velocity cross-correlation function is its Fourier transform:

$$\beta C_{v,F_{th}}(t) = 2m_p \int_{-\infty}^{\infty} \frac{d\omega}{2\pi} e^{-i\omega t} \mu(\omega)\gamma^*[\omega] \tag{1.57}$$

1.2.6 Cumulative velocity PSD (first order approximation)

By considering the dominant terms in S_v for large ω, it can be shown that when $CS_v(\omega) \approx \langle v^2 \rangle$, it can be estimated using first order approximation:

$$CS_v \approx \frac{k_B T}{m^*}\left[1 - \sqrt{\frac{\pi}{8\tau_v}}\omega^{-1/2}\right] \tag{1.58}$$

165

Bibliography

[1] Joseph Klafter, MF Shlesinger, and Gert Zumofen. Beyond brownian motion. *Physics today*, pages 33–39, 1996.

[2] Milton Kerker. Brownian movement and molecular reality prior to 1900. *Journal of Chemical Education*, 51(12):764, December 1974.

[3] Felix M. Exner. Notiz zu Brown's Molecularbewegung. *Annalen der Physik*, 307(8):843–847, 1900.

[4] A. Einstein. Über die von der molekularkinetischen Theorie der Wärme geforderte Bewegung von in ruhenden Flüssigkeiten suspendierten Teilchen. *Annalen der Physik*, 322(8):549–560, 1905.

[5] Don S. Lemons. Paul Langevins 1908 paper On the Theory of Brownian Motion [Sur la theorie du mouvement brownien, C. R. Acad. Sci. (Paris) 146, 530533 (1908)]. *American Journal of Physics*, 65(11):1079, 1997.

[6] A. Einstein. Theoretische Bemerkungen Über die Brownsche Bewegung. *Zeitschrift für Elektrotechnik und Elektrochemie*, 13(6):41–42, February 1907.

[7] P Langevin. Sur la theorie du mouvement brownien. *Comptes Rendus Hebdomadaires des Seances de l'Academie des Sciences*, 146:508–533, 1908.

[8] Jean Perrin. Mouvement brownien et réalité moléculaire. *Annales de Chimie et de Physique*, 18:5–104, 1909.

[9] Peter Hänggi and Fabio Marchesoni. Introduction: 100 years of Brownian motion. *Chaos (Woodbury, N.Y.)*, 15(2):26101, June 2005.

[10] Tongcang Li, Simon Kheifets, David Medellin, and Mark G Raizen. Measurement of the instantaneous velocity of a Brownian particle. *Science (New York, N.Y.)*, 328(5986):1673–5, July 2010.

[11] Simon Kheifets, Akarsh Simha, Kevin Melin, Tongcang Li, and MG Raizen. Observation of Brownian Motion in Liquids at Short Times: Instantaneous Velocity and Memory Loss. *Science*, 343(March):1493–1496, 2014.

[12] R Kubo. The fluctuation-dissipation theorem. *Reports on Progress in Physics*, 29(1):255–284, January 1966.

[13] G E Uhlenbeck and L S Ornstein. On the theory of the Brownian motion. *Physical Review*, 36(5):823–841, 1930.

[14] A. Rahman. Correlations in the Motion of Atoms in Liquid Argon. *Physical Review*, 136(2A):A405–A411, October 1964.

[15] B. Alder and T. Wainwright. Velocity Autocorrelations for Hard Spheres. *Physical Review Letters*, 18(23):988–990, June 1967.

[16] B. J. Alder and T. E. Wainwright. Decay of the Velocity Autocorrelation Function. *Physical Review A*, 1(1):18–21, January 1970.

[17] V Lisy and J Tothova. On the (hydrodynamic) memory in the theory of Brownian motion. *arXiv preprint cond-mat/0410222*, pages 1–12, 2004.

[18] Kirstine Berg-Sø rensen and Henrik Flyvbjerg. The colour of thermal noise in classical Brownian motion: a feasibility study of direct experimental observation. *New Journal of Physics*, 7:38–38, February 2005.

[19] V Vladimirsky and Ya Terletzky. Hydrodynamical theory of translational Brownian motion. *Zhurnal Eksperimentalnoi i Teoreticheskoi Fiziki*, 15:258–263, 1945.

[20] R Zwanzig and M Bixon. Hydrodynamic theory of the velocity correlation function. *Physical Review A*, 1970.

[21] Allan Widom. Velocity Fluctuations of a Hard-Core Brownian Particle. *Physical Review A*, 3(4):1394–1396, April 1971.

[22] D. Bedeaux and P. Mazur. Brownian motion and fluctuating hydrodynamics. *Physica*, 76(2):247–258, September 1974.

[23] E. J. Hinch. Application of the Langevin equation to fluid suspensions. *Journal of Fluid Mechanics*, 72(03):499, March 1975.

[24] Y Pomeau and P Résibois. Time dependent correlation functions and mode-mode coupling theories. *Physics Reports*, 19(2):63–139, June 1975.

[25] James Clerk Maxwell. *A Treatise on Electricity and Magnetism.* Clarendon Press, Oxford, first edition, 1873.

[26] E. F. Nichols and G. F. Hull. The Pressure due to Radiation. *The Astrophysical Journal*, 17:315, June 1903.

[27] P. N. Lebedev. Untersuchungen über die druckkräfte des lichtes. *Ann. d. Phys.*, 6:433, 1901.

[28] E. F. Nichols and G. F. Hull. A preliminary communication on the pressure of light and heat radiation. *Science*, 14:588, 1901.

[29] A Ashkin. Acceleration and Trapping of Particles by Radiation Pressure. *Physical Review Letters*, 24(4):156–159, January 1970.

[30] A Ashkin and JM Dziedzic. Optical levitation of liquid drops by radiation pressure. *Science*, 187(4181):1073–1075, 1975.

[31] A Ashkin and J. M. Dziedzic. Optical levitation in high vacuum. *Applied Physics Letters*, 28(6):333, 1976.

[32] A. Ashkin. Atomic-beam deflection by resonance-radiation pressure. *Physical Review Letters*, 25:1321–1324, 1970.

[33] T.W. Hänsch and A.L. Schawlow. Cooling of gases by laser radiation, 1975.

[34] A. Ashkin. Trapping of atoms by resonance radiation pressure. *Physical Review Letters*, 40:729–732, 1978.

169

[35] D. J. Wineland, R. E. Drullinger, and F. L. Walls. Radiation-pressure cooling of bound resonant absorbers. *Physical Review Letters*, 40:1639–1642, 1978.

[36] A. Ashkin, J. M. Dziedzic, J. E. Bjorkholm, and Steven Chu. Observation of a single-beam gradient force optical trap for dielectric particles. *Optics Letters*, 11(5):288, May 1986.

[37] A Ashkin and J M Dziedzic. Optical trapping and manipulation of viruses and bacteria. *Science (New York, N.Y.)*, 235:1517–1520, 1987.

[38] A. Ashkin, J. M. Dziedzic, and T. Yamane. Optical trapping and manipulation of single cells using infrared laser beams. *Nature*, 330(6150):769–71, 1987.

[39] A. Ashkin. History of optical trapping and manipulation of small-neutral particle, atoms, and molecules. *IEEE Journal on Selected Topics in Quantum Electronics*, 6:841–856, 2000.

[40] a Ashkin. Forces of a single-beam gradient laser trap on a dielectric sphere in the ray optics regime. *Biophysical Journal*, 61(2):569–582, February 1992.

[41] Y Harada. Radiation forces on a dielectric sphere in the Rayleigh scattering regime. *Optics Communications*, 124(5-6):529–541, March 1996.

[42] W H Wright, G J Sonek, and M W Berns. Parametric study of the forces on microspheres held by optical tweezers. *Applied optics*, 33(9):1735–48, March 1994.

[43] R Omori, T Kobayashi, and a Suzuki. Observation of a single-beam gradient-force optical trap for dielectric particles in air. *Optics letters*, 22(11):816–8, June 1997.

[44] Yong Kim and Joseph Matta. Long-Time Behavior of the Velocity Autocorrelation: A Measurement. *Physical Review Letters*, 31(4):208–211, July 1973.

[45] Paul Fedele and Young Kim. Direct Measurement of the Velocity Autocorrelation Function for a Brownian Test Particle. *Physical Review Letters*, 44(11):691–694, March 1980.

[46] W Denk and W W Webb. Optical measurement of picometer displacements of transparent microscopic objects. *Applied optics*, 29(16):2382–91, June 1990.

[47] K. Svoboda, C.F. Schmidt, B.J. Schnapp, and S.M. Block. Direct observation of kinesin stepping by optical trapping interferometry. *Nature*, 365(6448):721–727, 1993.

[48] Lucien P. Ghislain, Neil A. Switz, and Watt W. Webb. Measurement of small forces using an optical trap. *Review of Scientific Instruments*, 65:2762–2768, 1994.

[49] S B Smith, Y Cui, and C Bustamante. Overstretching B-DNA: the elastic response of individual double-stranded and single-stranded DNA molecules. *Science (New York, N.Y.)*, 271(5250):795–9, February 1996.

[50] Koen Visscher, SP Gross, and SM Block. Construction of multiple-beam optical traps with nanometer-resolution position sensing. *IEEE Journal of Selected Topics in Quantum Electronics*, 2(4):1066–1076, 1996.

[51] F Gittes and C F Schmidt. Interference model for back-focal-plane displacement detection in optical tweezers. *Optics letters*, 23(1):7–9, January 1998.

[52] M W Allersma, F Gittes, M J DeCastro, R J Stewart, and C F Schmidt. Two-dimensional tracking of ncd motility by back focal plane interferometry. *Biophysical journal*, 74(2 Pt 1):1074–85, March 1998.

[53] a Pralle, M Prummer, E L Florin, E H Stelzer, and J K Hörber. Three-dimensional high-resolution particle tracking for optical tweezers by forward scattered light. *Microscopy research and technique*, 44(5):378–86, March 1999.

[54] Isaac Chavez, Rongxin Huang, Kevin Henderson, Ernst-Ludwig Florin, and Mark G Raizen. Development of a fast position-sensitive laser beam detector. *The Review of scientific instruments*, 79(10):105104, October 2008.

[55] Tongcang Li, Simon Kheifets, and Mark G. Raizen. Millikelvin cooling of an optically trapped microsphere in vacuum. *Nature Physics*, 7(7):527–530, March 2011.

[56] Edmund Optics. Understanding ball lenses. `http://www.edmundoptics.com/technical-resources-center/optics/understanding-ball-lenses/`, 2014. [Online; accessed 22-June-2014].

[57] R.S. RS Bradley. The cohesive force between solid surfaces and the surface energy of solids. *The London, Edinburgh, and Dublin Philosophical Magazine and Journal of Science*, 13(86):853–862, 1932.

[58] B.V Derjaguin, V.M Muller, and Yu.P Toporov. Effect of contact deformations on the adhesion of particles. *Journal of Colloid and Interface Science*, 53(2):314–326, November 1975.

[59] LO Heim, Jürgen Blum, Markus Preuss, and HJ Butt. Adhesion and friction forces between spherical micrometer-sized particles. *Physical Review Letters*, pages 16–19, 1999.

[60] Tongcang Li. *Fundamental Tests of Physics with Optically Trapped Microspheres*. PhD thesis, University of Texas at Austin, May 2011.

[61] Astrid van der Horst. *High-refractive index particles in counter-propagating optical tweezers - manipulation and forces*. PhD thesis, Utrecht University, September 2006.

[62] Yohai Roichman, Bo Sun, Allan Stolarski, and David Grier. Influence of Nonconservative Optical Forces on the Dynamics of Optically Trapped Colloidal Spheres: The Fountain of Probability. *Physical Review Letters*, 101(12):1–4, September 2008.

[63] B. Lukić, S. Jeney, C. Tischer, a. Kulik, L. Forró, and E.-L. Florin. Direct Observation of Nondiffusive Motion of a Brownian Particle. *Physical Review Letters*, 95(16):160601, October 2005.

[64] Patrick Kwee and Benno Willke. Automatic laser beam characterization of monolithic Nd:YAG nonplanar ring lasers. *Applied optics*, 47(32):6022–32, November 2008.

[65] Abouzar Moshfegh, Mehrzad Shams, Goodarz Ahmadi, and Reza Ebrahimi. A novel surface-slip correction for microparticles motion. *Colloids and Surfaces A: Physicochemical and Engineering Aspects*, 345(1-3):112–120, August 2009.

[66] R Kubo. Brownian motion and nonequilibrium statistical mechanics. *Science (New York, N.Y.)*, 233(4761):330–4, July 1986.

[67] G. Wang, E. Sevick, Emil Mittag, Debra Searles, and Denis Evans. Experimental Demonstration of Violations of the Second Law of Thermodynamics for Small Systems and Short Time Scales. *Physical Review Letters*, 89(5):1–4, July 2002.

[68] Asa Hopkins, Kurt Jacobs, Salman Habib, and Keith Schwab. Feedback cooling of a nanomechanical resonator. *Physical Review B*, 68(23):235328, December 2003.

[69] Dustin Kleckner and Dirk Bouwmeester. Sub-kelvin optical cooling of a micromechanical resonator. *Nature*, 444(7115):75–8, November 2006.

[70] Kenneth G Libbrecht and Eric D Black. Toward quantum-limited position measurements using optically levitated microspheres. *Physics Letters A*, 321(2):99–102, January 2004.

[71] A Ashkin and J. M. Dziedzic. Optical levitation in high vacuum. *Applied Physics Letters*, 28(6):333, 1976.

[72] D E Chang, C a Regal, S B Papp, D J Wilson, J Ye, O Painter, H J Kimble, and P Zoller. Cavity opto-mechanics using an optically levitated nanosphere. *Proceedings of the National Academy of Sciences of the United States of America*, 107(3):1005–10, January 2010.

[73] Oriol Romero-Isart, Mathieu L Juan, Romain Quidant, and J Ignacio Cirac. Toward quantum superposition of living organisms. *New Journal of Physics*, 12(3):033015, March 2010.

[74] G. G. Stokes. On the effect of the internal friction of fluids on the motion of pendulums. *Cambridge Philos. Trans.*, 9:8–106, 1851. Reprinted in Mathematical and Physical Papers, 2nd ed., Vol. 3. New York: Johnson Reprint Corp., p. 1, 1966.

[75] L. D. Landau. *Fluid mechanics.* Elsevier/Butterworth-Heinemann, Amsterdam, 2004.

[76] Joseph Boussinesq. Sur la résistance quoppose un fluide indéfini au repos, sans pesanteur, au mouvement varié dune sphère solide quil mouille sur toute sa surface, quand les vitesses restent bien continues et assez faibles pour que leurs carrés et produits soient néglige. *Comptes rendus hebdomadaires des séances de l'Académie des sciences*, 100:935, 1885.

[77] A. B. Basset. On the Motion of a Sphere in a Viscous Liquid. *Philosophical Transactions of the Royal Society A: Mathematical, Physical and Engineering Sciences*, 179(January):43–63, January 1888.

[78] Robert Zwanzig and Mordechai Bixon. Compressibility effects in the hydrodynamic theory of Brownian motion. *Journal of Fluid Mechanics*, 69(01):21–25, March 1975.

[79] L D Landau and E M Lifshitz. *Fluid Mechanics, volume 6 of Course of Theoretical Physics.* Prentice-Hall, Oxford Pergamon Press, 2nd edition, 1987.

[80] Oleksiy Svitelskiy, Yangcheng Li, Arash Darafsheh, Misha Sumetsky, David Carnegie, Edik Rafailov, and Vasily N Astratov. Fiber coupling to BaTiO¡sub¿3¡/sub¿ glass microspheres in an aqueous environment. *Optics letters*, 36(15):2862–4, August 2011.

[81] Arash Darafsheh, Gary F. Walsh, Luca Dal Negro, and Vasily N. Astratov. Optical super-resolution by high-index liquid-immersed microspheres. *Applied Physics Letters*, 101(14):141128, 2012.

[82] Steve Smith. Make a microchamber. `http://tweezerslab.unipr.it.` `/cgi-bin/mt/documents.pl/Show?_id=a77c&sort=DEFAULT&search=` `&hits=22`, 2008. [Online; accessed 16-June-2014].

[83] Kirstine Berg-Sø rensen and Henrik Flyvbjerg. Power spectrum analysis for optical tweezers. *Review of Scientific Instruments*, 75(3):594, 2004.

[84] Ren van Wezel. Advanced notes on water immersion lenses. `http://` `www.microscopy-uk.org.uk/mag/artapr05/rvwimm.html`, 2005. [Online; accessed 16-June-2014].

[85] Megan T Valentine, Nicholas R Guydosh, Braulio Gutiérrez-Medina, Adrian N Fehr, Johan O Andreasson, and Steven M Block. Precision steering of an optical trap by electro-optic deflection. *Optics letters*, 33(6):599–601, March 2008.

[86] O Jennrich. A high power photodetection system for use with laser interferometric gravitational wave detectors. *Optics Communications*, 205(4-6):405–413, May 2002.

[87] Patrick Kwee, Benno Willke, and Karsten Danzmann. Shot-noise-limited laser power stabilization with a high-power photodiode array. *Optics letters*, 34(19):2912–4, October 2009.

[88] Patrick Kwee, Benno Willke, and Karsten Danzmann. Laser power noise detection at the quantum-noise limit of 32 A photocurrent. *Optics letters*, 36(18):3563–5, September 2011.

[89] Paul Horowitz. *The art of electronics.* Cambridge University Press, Cambridge England New York, 1989.

[90] Mohammed Mahamdeh, C Pérez Campos, and E Schäffer. Under-filling trapping objectives optimizes the use of the available laser power in optical tweezers. *Optics express*, 19(12):1260–1262, 2011.

[91] H. Clercx and P. Schram. Brownian particles in shear flow and harmonic potentials: A study of long-time tails. *Physical Review A*, 46(4):1942–1950, August 1992.

[92] G L Paul and P N Pusey. Observation of a long-time tail in Brownian motion. *Journal of Physics A: Mathematical and General*, 14(12):3301–3327, December 1981.

[93] Robert E. London. Forcevelocity cross correlations and the Langevin equation. *The Journal of Chemical Physics*, 66(2):471, January 1977.

[94] V Balakrishnan. Fluctuation-dissipation theorems from the generalised Langevin equation. *Pramana*, 12(4):301–315, 1979.

[95] Rongxin Huang, Isaac Chavez, Katja M. Taute, Branimir Lukić, Sylvia Jeney, Mark G. Raizen, and Ernst-Ludwig Florin. Direct observation of

the full transition from ballistic to diffusive Brownian motion in a liquid. *Nature Physics*, 7(7):576–580, March 2011.

[96] Matthias Grimm, Sylvia Jeney, and Thomas Franosch. Brownian motion in a Maxwell fluid. *Soft Matter*, 7(5):2076, 2011.

[97] Daniel Rings, Romy Schachoff, Markus Selmke, Frank Cichos, and Klaus Kroy. Hot Brownian Motion. *Physical Review Letters*, 105(9):8–11, August 2010.

[98] Jérôme Duplat, Simon Kheifets, Tongcang Li, Mark G Raizen, and Emmanuel Villermaux. Superdiffusive trajectories in Brownian motion. *Physical Review E*, 87(2):020105, February 2013.

[99] U. Seifert. Stochastic thermodynamics: principles and perspectives. *The European Physical Journal B*, 64(3-4):423–431, January 2008.

[100] D. Carberry, J. Reid, G. Wang, E. Sevick, Debra Searles, and Denis Evans. Fluctuations and Irreversibility: An Experimental Demonstration of a Second-Law-Like Theorem Using a Colloidal Particle Held in an Optical Trap. *Physical Review Letters*, 92(14):1–4, April 2004.

[101] E H Trepagnier, C Jarzynski, F Ritort, G E Crooks, C J Bustamante, and J Liphardt. Experimental test of Hatano and Sasa's nonequilibrium steady-state equality. *Proceedings of the National Academy of Sciences of the United States of America*, 101(42):15038–41, October 2004.

[102] a. Imparato, L. Peliti, G. Pesce, G. Rusciano, and a. Sasso. Work and heat probability distribution of an optically driven Brownian particle: Theory and experiments. *Physical Review E*, 76(5):1–4, November 2007.

[103] T Speck, V Blickle, C Bechinger, and U Seifert. Distribution of entropy production for a colloidal particle in a nonequilibrium steady state. *Europhysics Letters (EPL)*, 79(3):30002, August 2007.

[104] V. Blickle, T. Speck, C. Lutz, U. Seifert, and C. Bechinger. Einstein Relation Generalized to Nonequilibrium. *Physical Review Letters*, 98(21):210601, May 2007.

[105] K Svoboda and S M Block. Optical trapping of metallic Rayleigh particles. *Optics letters*, 19(13):930–2, July 1994.

[106] Faeghe Hajizadeh and S Nader S Reihani. Optimized optical trapping of gold nanoparticles. *Optics express*, 18(2):551–9, January 2010.

[107] Daniel Rings, Romy Schachoff, Markus Selmke, Frank Cichos, and Klaus Kroy. Hot Brownian Motion. *Physical Review Letters*, 105(9):090604, August 2010.

[108] L. Joly, S. Merabia, and J.-L. Barrat. Effective temperatures of a heated Brownian particle. *EPL (Europhysics Letters)*, 94(5):50007, June 2011.

[109] D Chakraborty, M. V. Gnann, D. Rings, J. Glaser, F. Otto, F. Cichos, and K. Kroy. Generalised Einstein relation for hot Brownian motion. *EPL (Europhysics Letters)*, 96(6):60009, December 2011.

[110] Paul Godfrey. Matlab file exchange: erfz. `http://www.mathworks.` `com/matlabcentral/fileexchange/3574-erfz`, 2003. [Online; accessed 14-July-2014].

Vita

Simon Kheifets was born in St. Petersberg, Russia in 1986. He moved to Adelaide, Australia in 1991 and then to Canberra, Australia in 1997. He completed his high school education at Narrabundah College in 2004. He received a AB in physics from Princeton University in 2009. He entered graduate school at the University of Texas at Austin in 2009 and joined the Raizen group in January of 2010.

Permanent address: 3 Liffey Circuit
                    Kaleen, ACT 2617
                    Australia

This dissertation was typeset with LaTeX[†] by the author.

[†]LaTeX is a document preparation system developed by Leslie Lamport as a special version of Donald Knuth's TeX Program.